STUDY OF THERMAL RESPONSE IN HIGHLY POROUS HEAT SHIELD MATERIALS SUBJECTED TO HIGH TEMPERATURE FLOWS

BY

BERNARD OTIENO OWITI

(D16T1102C)

DEPARTMENT OF MECHANICAL AND AEROSPACE ENGINEERING

TOTTORI UNIVERSITY

JANUARY, 2020

STUDY OF THERMAL RESPONSE IN HIGHLY POROUS HEAT SHIELD MATERIALS SUBJECTED TO HIGH TEMPERATURE FLOWS

BY

BERNARD OTIENO OWITI

(D16T1102C)

A DISSERTATION SUBMITTED IN PARTIAL FULFILMENT OF THE
REQUIREMENTS FOR THE DEGREE OF DOCTOR OF PHYLOSOPHY
(Ph.D.) IN MECHANICAL AND AEROSPACE ENGINEERING IN
TOTTORI UNIVERSITY

JANUARY, 2020

Table of Contents

Chapter 1

Chapter 2

Chapter 3

Chapter 4

Chapter 5

List of Tables

List of Figures

Nomenclature

A_i = Equilibrium reaction constants (i=1,2,3,4,5)

$A_{\lambda i}$ = Absorption coefficient curve fit parameters

A_s, B_s, C_s = Evaluation constants for Blottner’s viscosity model

A, B = Landau-Teller relaxation time constants

B_λ = Planck’s function at wavelength, λ

c_1 = Potts formula constant, K

c_2 = Potts formula constant, J/(kg-K)

c_s = Average molecular speed, m/s

$c_{v,s}$ = Species s translational-rotational specific heat at constant volume, J/(kg-K)

$c_{v,tr,s}$ = Species s translational specific heat at constant volume, J/(kg-K)

$c_{v,rot,s}$ = Species s rotational specific heat at constant volume, J/(kg-K)

$c_{v,vib,s}$ = Species s vibrational specific heat at constant volume, J/(kg-K)

C_f = Reaction rates coefficient constants, m^3/(mol-s)

C_p = Specific heat at constant pressure, J/(kg-K)

d_{coef} = Diffusion coefficient, m^2/s

e = Internal energy, J/kg

$e_{el,s}$ = Species s electronic energy per unit mass, J/kg

e_{gas}, e_{sol} = Gas and solid material energy per unit volume respectively, J/m^3

$e_{v,s}$ = Species s vibrational energy per unit mass, J/kg

$e_{v,s}(T)$ = Species s vibrational energy per unit mass at local temperature, J/kg

f_x, f_r = Friction force per unit volume in x and r directions respectively, J/m^3

E = Total convective flux vector in x direction

E_e = Electronic energy per unit volume, J/m^3

E_{inv} = Inviscid convective flux vector in x direction

E_t = Total energy per unit volume, J/m^3

E_v = Vibrational energy per unit volume, J/m^3

E_{vis} = Viscous convective flux vector in x direction

F = Total convective flux vector in r or y direction

F_{inv} = Inviscid convective flux vector in r or y direction

F_{rad} = Radiative source term

F_{vis} = Viscous convective flux vector in r or y direction

$g_{i,s}$ = i^{th} state electronic degeneracy for species s

H = Total flux vector for axisymmetric flow

H_{inv} = Inviscid flux vector for axisymmetric flow

H_{vis} = Viscous flux vector for axisymmetric flow

h_s = Species s enthalpy per unit mass, J/kg

h_s^0 = Species s enthalpy of formation per unit mass, J/kg

I_λ = Intensity of radiation at wavelength λ, W/sr

$I(s_r)$ = Intensity of light at path length s_r, cd

I_o = Initial intensity of light emitted from the source, cd

J = Mass flux, kg/(m^2-s)

k = Mixture’s translational-rotational temperature conductivity, W/(m-K)

k_b, k_f = Backward and forward reaction rate coefficients, m^3/(mol-s)

k_{eff} = Effective conductivity, W/(m-K)

k_{gas} = Gas thermal conductivity, W/(m-K)

k_{rad} = Radiative conductivity, W/(m-K)

k_{sol} = Solid material thermal conductivity, W/(m-K)

k_v = Mixture's vibrational-electronic temperature conductivity, W/(m-K)

$k_{v,s}$ = Species s vibrational-electronic temperature conductivity, W/(m-K)

K_{eq} = Equilibrium constant, 1 or mol/m^3

m = Mass, kg

$\dot{m}$ = Mass flow rate per unit area, kg/(m^2-s)

$\dot{M}$ = Mass flow rate, kg/s

M_s = Species s atomic weight, kg/mol

nit = Nitridation

n_s = Species s number density, mol/m^3

p = Total pressure, Pa

P_e = Electron partial pressure/Equilibrium vapor pressure, Pa

q = Wall surface heat flux, W/m^2

q_{CFD} = Heat flux from CFD calculation, MW/m^2

q_{net} = Net surface heat flux, MW/m^2

q_x, q_y = Translational-rotational heat flux in x and y directions respectively, W/m^2

q_{v_x}, q_{v_y} = Vibrational-electronic heat flux in x and y directions respectively, W/m^2

Q = Conservative variables vector

Q_{d-v} = Vibrational energy transfer rate through dissociation, J/(m^3-s)

Q_{e-e} = Electron-electronic energy transfer rate, J/(m^3-s)

Q_{e-ex} = Energy transfer rate in electronic excitation, J/(m^3-s)

Q_{t-e} = Translational-electron energy transfer rate, J/(m^3-s)

Q_{t-v} = Translational-vibrational energy transfer rate, J/(m^3-s)

r = radial distance (Fig. 3.3)

r_{ml} = Mass loss rate, m/s

R = Cylinder radius (Fig. 3.3)

$\hat{R}$ = Universal gas constant, J/(mol-K)

R_i = i^{th} reaction

s_p = Ray path length

sr = Surface recession, m

sub = Sublimation

t = Time, s

T , T_{tr} = Translational-rotational temperature, K

T_a = Average temperature for calculating reaction rate coefficient, K

T_{gas} = Gas temperature, K

T_{sol} = Solid material temperature, K

T_{ve} = Vibrational-electronic temperature, K

T_w = Wall temperature, K

u, v = Velocity components in x and r directions respectively, m/s

u_s, v_s = Species velocity components in x and r directions respectively, m/s

W = Source vector

W_s = Species s reaction mass source term, kg/(m^3-s)

W_v = Vibrational-electronic energy source term, J/(m^3-s)

x, r = Axisymmetric coordinates, m

X_s = Species s molar concentration

Greek Symbols

α, γ, γ' = Angles (Fig. 3.3), *radians*

α = Reaction probability, coefficient of heat transfer, W/(m^3-K)

β = Extinction coefficient, m^{-1}

ε = Porosity

γ = Permeability, m^2

$\theta_{d,s}$ = Reaction characteristic temperature

$\theta_{el1,s}$ = Species s first excitation state characteristic temperature, K

$\theta_{v,s}$ = Vibrational characteristic temperature for species s, K

κ_{λ} = Absorption coefficient at a given wavelength, cm^{-1}

μ = Mixture's viscosity, (N-s)/m^2

μ_x, μ_y = Reaction orders in x and y directions respectively

μ_s = Species s viscosity, (N-s)/m^2

η = Reaction rate constant

ρ, ρ_s = Total and species s densities respectively, kg/m^3

$\tilde{\rho}_s$ = Element s elemental density, kg/m^3

α_{rlx} = Heat transfer coefficient, W/(m^3-K)

σ_s = Energy transfer cross-section between electrons and species s heavy particles

σ_{SB} = Stefan-Boltzmann constant, $5.67e^{-8}$ W/(m^2-K^4)

σ_{sr} = Species s and r collision cross-section

σ_{λ} = Absorption cross-section at a given wavelength, m^2

$\tau_{c,s}$ = Species s collision limited vibrational relaxation rate

$\tau_{xx}, \tau_{xy}, \tau_{yy}, \tau_{y\theta}$ = Shear stress tensors, N/m^2

τ_s = Species s characteristic reaction time

τ_v = Characteristic translational-rotational relaxation rate

ϕ_s = Wilke's mixing model parameter

Subscripts

BL = Baldwin-Lomax model
CFD = Computational Fluid Dynamics
cw = Cold wall
eff = Effective
gas = Gas
inj = Injection-induced turbulence model
inv = Inviscid flow
vis = Viscous flow
$conv$ = Convective
l = Laminar
LT = Landau-Teller
$\max$ = Maximum
net = Net
rad = Radiative
rlx = Relaxation
SB = Stefan-Boltzmann
sol = Solid
t = Turbulent flow
w = Wall surface
∞ = Freestream
λ = Wavelength, m

Chapter 1

Introduction

1.1 Background

In a bid to expound the knowledge about the origin of the solar system, both manned and robotic planetary exploration missions have been scaling up and will continue to grow steadily with more and more missions in line. For instance, the launch of Exploration Mission-1 (EM-1) by the National Aeronautics and Space Administration (NASA) is planned for the year 2020. The first among a series of increasingly complex missions, EM-1 will be an unmanned mission to the moon and beyond [1]. Right from the Pioneer mission, all these space explorations are geared toward conducting scientific researches and finding more information about the solar system as well as investigating the possibility of extending human existence to the moon and even the space beyond. The Apollo program made history back in the day as one of the greatest achievements of mankind when it landed on the lunar surface in July 1969 [2]. In Japan, H-II Transfer Vehicle (HTV) Small Re-entry Capsule (HSRC) was launched by Japan Aerospace Exploration Agency (JAXA) and successfully berthed to the International Space Station (ISS) in September, 2018.

Space vehicles return to earth's atmosphere from exploration missions at hypersonic re-entry velocities of about 8000 m/s or even higher. At these velocities, the re-entry vehicle is exposed to strong shocks, both equilibrium and non-equilibrium gas chemistry, huge amounts of heat fluxes and consequently, extremely high temperatures [3-6]. For instance, NASA's Pioneer-Venus experienced a high stagnation heating rate of about 55 MW/m^2 while JAXA's Hayabusa had a peak heating rate of 15 MW/m^2 during its re-entry to earth's atmosphere [7]. Most of the kinetic energy of the incoming flow is dissipated in the form of heat at extremely high temperatures through dissociation or ionization of the flow species in the radiative shock layer that forms around the vehicle. The vehicles, therefore, require thermal protection system (TPS) to survive the intense heating rates [8].

Success of space exploration missions heavily depends on the choice of the TPS as well as the reliability of its performance prediction [9, 10]. Therefore, TPS is one of the most significant components of the vehicle [11-13]. TPS materials are generally grouped into two broad categories, i.e. ablative TPS like the ones used for the Gemini, Mercury, Apollo missions [14], and non-ablative TPS, e.g. the ceramic tiles used on the space shuttle [15]. Both beryllium and phenolic asbestos TPS were used for the Apollo re-entry in 1965. Pioneer-Venus, Galileo and Hayabusa missions used carbon-phenolic TPS. Phenolic Impregnated Carbon Ablator (PICA), an example of low density ablative TPS which was developed by NASA [16, 17], has been successfully applied in NASA's past missions [18]. In Japan, a low-density ablative material [19] was successfully used as the TPS for the launch of HSRC. Ablative TPS, in particular, mitigates the incoming heat to the vehicle surface through chemical reactions, phase changes, and material removal through ablation process [20].

The mass decrease of ablative TPS has been the greatest challenge to the design of TPS for a long time. Owing to the high-density materials used in the past, TPS have always taken quite a large fraction of the total mass of the vehicle. For instance, in Ref. [7], the mass fraction of the TPS used in Hayabusa was about 40% of the total mass of the vehicle. High density carbon/carbon and carbon/resin composites have been widely applied as ablative TPS in the past [21]. Typical densities of such ablative TPS were way over 1 g/cm^3. For example, densities of the ablative TPS used in Hayabusa and Pioneer-Venus missions were 1.4 and 1.49 g/cm^3, respectively [5, 22].

An accurate and reliable prediction of ablative TPS performance is desirable in order to closely estimate the design of its weight and thickness [23]. This is particularly important owing to the sacrificial nature of the charring ablative TPS [24]. Photograph of a porous carbon-based material is shown in Fig. 1.1. When this material is impregnated with resin, an ablative material with a higher density results. Heating the resulting ablative material to elevated temperatures of 1200 K and beyond thermally decomposes resin and the material is thereby converted into a highly porous char layer, also shown in Fig. 1.1. Transformation processes in ablative TPS during ablation can be demonstrated as shown in Fig. 1.2. At the ablating surface, and depending on the temperature of the surface, the reaction processes mentioned in Ref. [20] may occur. They include oxidation of the surface carbon atoms [25], nitridation, sublimation and surface recombination of the freestream atomic species. At temperatures higher than 3000 K, atomic carbon actively undergoes sublimation [26]. During these transformation processes, the ablative material undergoes both pyrolysis and ablation phenomena. The developed char layer may undergo ablation processes as a result of the heterogeneous chemical reactions, e.g. oxidation and nitridation, phase change through sublimation as well as mechanical erosion through spallation. All these processes lead to the recession at the surface of the TPS [27].

Low density carbon-based material with porosity values typically in the order of 90% is a promising candidate for light ablative TPS [28]. Such a light and highly porous material has an apparent density in the order of 0.1 and is readily available commercially. Both the virgin and char materials in the transformation process explained above have lower densities compared to the materials used in the past space exploration missions described in Ref. [7]. Both heat and mass transfer processes, and thermochemical degradation of a low-density ablative material should be understood before its application as a heat shield material [29-31]. Among these processes, modeling of radiative transfer within a highly porous ablative material like the ablative char layer offers a unique opportunity for the thermal response analysis that is different from the existing radiative transfer solution methods. This is because the char layer has an inner morphology that is quite different from the initial porous state due to the resulting char residue from the thermal decomposition of the resin filler during heating of the material.

To ascertain the integrity of ablative TPS performance analysis methods, they must be able to reproduce the corresponding experimental data to within acceptable levels of accuracy. This accuracy can be enhanced further by capturing the computational fluid dynamics (CFD) flow and material response interactions through a coupling method that is able to account for the radial non-uniformity of the arcjet freestream distribution. It is desirable to develop a coupling approach that will be able to take care of the radial non-uniformity of the flow variables at the interface of the CFD flow and material response analysis fields.

Experimental data used for validating numerical simulation models for ablative material's thermal response analysis are normally generated by a range of ground test facilities. These facilities are capable of generating flow and enthalpies that are sufficiently high for application in a specific aerodynamic re-entry environment. Examples of such facilities include: the arc heated wind tunnels, plasma wind tunnels, hypersonic shock tubes and tunnels, inductive torches, among others. Constrictor-type arc heated wind tunnel is commonly used for the simulation of severe aerodynamic heating environments encountered by the space vehicles during atmospheric re-entry [32-37]. This type of arcjet wind tunnel has been in operation since its first development in the late 1950's [38].

There is need to conduct continuous analysis for the entire flow field within the arc heated wind tunnel from the heater section up to the test chamber section. Such analysis is particularly important for the satisfactory performance assessment of the ablative TPS within the test chamber section of a wind tunnel, in which the flow field data from the arc heater section are required for calculation of the Pitot pressure and heat flux distributions therein. Such an elaborate and detailed numerical analysis of the integral parts of the entire arcjet wind tunnel is relatively unclear currently. Numerical analysis of the arc heater and the test chamber flow fields are often done independently. For instance, a high enthalpy arc heater operational conditions have been analyzed numerically only up to the physical nozzle throat [39].

The current research, therefore, seeks to address the above existing issues through the study of the following: (1) flow field analysis of the entire arc heated wind tunnel and validation of the numerical methodology, and (2) development of a radiative transfer model for analyzing the thermal response of ablative TPS using a coupling approach which has the capability of accounting for the radial non-uniformity of the flow field within the test chamber.

1.2 Previous Researches and Problem Description

1.2.1 Ablative TPS and Radiative Transfer Models

Ablation phenomenon has been actively studied since the advent of the ablative TPS [40-45]. Ablation is a transformation phenomenon that may occur due to the heterogeneous chemical reactions (oxidation and nitridation), phase change (sublimation), and/or mechanical erosion (spallation) of the char layer of an ablative porous material. These processes result in the mass loss of the char layer as well as the recession at the surface of the ablative porous material that are estimated using the ablative material response models [46].

Ablative material response models have been developed in the past mainly to analyze the multi-dimensional gas flow within the porous ablative materials. Most of these models were designed to blow away the pyrolysis gases generated by the decomposing resin fillers into the boundary layer around the surface of the material, Ref. [21]. Pyrolysis gases are usually transported from the ablative TPS by complex diffusion and convection processes through the substrate of the porous carbon fiber [47]. The Q* model is among the several models developed in the past to predict the rates of ablation in the ablative materials [48]. This model determines the heat of ablation using some experimental correlation. Even though this model can be used to offer a quick estimate of the amount of the ablated surface, it excludes the detailed analysis which raises the questions of its reliability, Ref. [44]. In the current study, an attempt is made to closely estimate thermal response of the charred piece of an ablative TPS by using an ablation model that is more detailed but excludes the pyrolysis processes.

Radiative transfer is an important mode of heat transfer for the thermal response analysis in porous ablative TPS, especially under extreme heating conditions. Therefore, modeling of radiative transfer is highly essential for the success of such analysis. Radiative transfer models for the porous carbon materials have been developed in the past to study other variables such as the effective thermal conductivity [49-51]. For instance, De Micco and Aldao [52] did a review of some of the models for evaluating radiative conductance expressions and the overall thermal conductivity. Nouri and his co-researchers [53] used a 3D direct simulation model obtained from an X-ray microtomography to capture the macroscopic geometric properties of an ablative fibrous material. Their results were found to compare acceptably with the corresponding experimental data. Again, both arcjet tests and computational fluid dynamics (CFD) calculations have been done previously to investigate the thermal response of ablative materials [54-56]. Nevertheless, from the above reviews, effect of radiative transfer in porous ablative material on its overall heat transfer mechanisms in extreme heating conditions is relatively unknown. Since exact analytical methods for the radiative transfer calculations are usually very time-consuming in terms of computation, an alternative method which is acceptably accurate and efficient is desirable. This is the reason why this study seeks to introduce an approximate but appropriate and efficient methodology for analyzing radiative transfer in porous carbon-based materials under reasonable assumptions.

In order to increase the accuracy of thermal response analysis in ablative TPS, proper modeling of the heating rate at the material surface is critical. One way of doing this is to couple the interactions in the CFD flow solver to the material response analysis model as explained in Ref. [8]. Over the years, numerical simulation of coupled radiation and ablation processes have progressed from the viscous shock layer methods which involve coupling of the boundary layer solutions with inviscid shock layer solutions to the upwind based finite volume methods [57]. Even though ablative materials have been the subjects of many experimental and numerical studies, particularly in the 1960's and 1970's, most coupling models have somehow stagnated at the level of empirical approximations introduced at the time [58], majority of which assume radial uniform distributions of flow variables along the heating surface of the test material.

The foregoing review indicates that a high-integrity computer code that is capable of closely reproducing the experimental data is desirable. Radiative transfer model and the coupling method are the major focus in this study.

1.2.2 Arc Heated Wind Tunnel Flow Analysis

As already mentioned, constrictor-type arc heated wind tunnel is currently the only viable and affordable possibility for both material qualification and validation of material response codes [59]. Schematic diagram of a typical constrictor-type arc heated wind tunnel is shown in Fig. 1.3.

It consists of five main components: the upstream electrode (anode) chamber, the constrictor tube section, the downstream electrode (cathode) chamber, the convergent-divergent nozzle section, and the test chamber section. Computer codes are usually desired for the numerical analysis of the entire arc heated wind tunnel. In this section, a review of the numerical methods for flow analysis within the arc heated wind tunnels is given.

A computer code named ARCFLO was first developed in NASA in the 1970's to analyze flow field within the constrictor section of the arc heater [60, 61]. The code incorporates a two-band gray-gas radiation model together with an eddy-viscosity turbulence model. However, this particular code was only capable of calculating flow within the constrictor. Later, a new CFD code named ARCFLO2 was developed [62] with the primary objective of converting the spatial marching in the previous ARCFLO into time-marching, see Ref. [39]. This code, however, failed to manage the numerical instability that occurred during simulation at high heating conditions. ARCFLO2 was upgraded further by Sakai and his co-researchers [63] to a new version named ARCFLO3. As stated in Ref. [39], this version was able to eliminate, fairly well, the earlier problems of numerical instability. Unlike the original ARCFLO code, modeling of radiation in this code was done using a three-band gray-gas approach by Sakai in Ref. [63]. Furthermore, this code was able to extend the flow field analysis but only up to the physical nozzle throat.

Availability of the experimental data for the entire flow field offers a rare opportunity for the development of an equivalent numerical approach to subsequently solve the arc heater, physical nozzle, and the test chamber flow fields. Simultaneous measurements of all the properties of the arcjet freestream from the arc heater section to the test chamber section is a rare practice. However, a simultaneous test for the entire flow field was recently conducted in JAXA's Institute of Space and Astronautical Science (ISAS) using their 1 MW constrictor-type arc heated wind tunnel. The experimental data from this test are used to validate the numerical model named ARCFLO3+ in this study. ARCFLO3+ combines the three code sets used to analyze flow in the arc heater, the nozzle, and the test chamber sections of the wind tunnel. Thereafter, the Pitot pressure and heat flux distributions within the test chamber flow field are evaluated and compared with experimental data. The validated CFD model is used for the coupling calculations of material thermal response.

1.3 Study Objectives and Outline

The overall objective of this study is to develop a high-fidelity computer code for analyzing the thermal response of a highly porous heat shield material subjected to atmospheric re-entry heating conditions. Prior to that, the existing numerical method for predicting the arcjet freestream flow properties for the constrictor-type arc heated wind tunnel is validated. The next objective is to investigate the effect of convective transport to the overall heat transfer mechanism within the heat shield material. The study is divided into five chapters as described below.

Chapter 1, which is the current chapter, constitutes the introductory part of this study. It highlights a brief history of the space exploration missions, the previous researches on ablative TPS materials, radiative transfer models, and the constrictor-type arc heated wind tunnels. It also includes the problem description, study objectives, and the research outline.

In chapter 2, the heating experiments conducted using JAXA’s 1 MW constrictor-type arc heated wind tunnel located at the ISAS are described. In this chapter, a brief description of the wind tunnel is made alongside the experimental set up and conditions. The final section of this chapter spells out the preparation procedures for the test specimens used in the study.

In chapter 3, all the numerical methods applied in this study are explained. First, the ARCFLO3+ code set is validated against the experimental data by regulating the amount of input power to the arc heater in order to closely reproduce the measured mass averaged enthalpy. Radiative heating is estimated using a three-band gray-gas radiation model. Thermochemical nonequilibrium CFD flow code that accounts for 21 species while solving the flow field within the test chamber is explained, giving elaborate details of all the governing equations used. Thereafter, the material thermal response is evaluated by following two distinct approaches. The first approach purely solves the solid material's energy conservation equation in a coupling process between the CFD flow and material response models. Details of the coupling approach are also explained. In the second approach, the mass, momentum, and convective gas energy conservation equations are incorporated in the formulation for Navier-Stokes governing equations and then solved alongside the solid material's energy conservation equation. However, in the latter approach, calculations are done entirely in an uncoupled manner. The sole aim in this case is to demonstrate the role of convective transfer in the overall thermal response analysis within the highly porous carbon-based materials. The last part of this chapter explains the grid convergence study.

Chapter 4 presents the results and discussion for all the considered study cases. Both the experimental and numerical results are compared, explained, and discussed. These results include: (1) arc heater operating conditions, (2) distribution of the arcjet flow properties, (3) heat flux and flow distribution analysis, (4) surface temperature time histories, and (5) in-depth temperature time histories.

Finally, in chapter 5, a summary of all the contents in the previous chapters is given. Consequently, the study conclusions are concisely drawn. Possible improvement areas are also suggested in the form of recommendations.

References

[1] https://www.nasa.gov/feature/nasa-s-deep-space-exploration-system-is-coming-together

[2] Dickey, J. O., Bender, P. L., Faller, J. E., Newhall, X. X., Ricklefs, R. L., Ries, J. G., Shelus, P. J., Veillet, C., Whipple, A. L., Wiant, J. R., Williams, J. G., and Yoder C. F., "Lunar Laser Ranging: A Continuing Legacy of the Apollo Program", *Science*, Vol. 265, Issue 5171, July 1994, pp. 482–490.

[3] Riccio, A., Raimondo, F., Sellitto, A., Carandente, V., Scigliano, R., and Tescione, D. "Optimum design of ablative thermal protection systems for atmospheric entry vehicles," *Journal of Applied Thermal Engineering*, Vol. 119, 2017, pp. 541–552.

[4] Amar, A. J., Calvert, D. N., and Benjamin, S. K., "Computation of Multi-Dimensional Material Response Coupled to Hypersonic Flow," AIAA Thermophysics Conference Paper, 2012.

[5] Anderson, J. D., "Hypersonic and High Temperature Gas Dynamics," Mac Graw-Hill, New York, 1989.

[6] Cozmuta, I., Wright, J. M., Laub, B., and Willcokson, H. W., "Defining Ablative Thermal Protection System Margins for Planetary Entry Vehicles," AIAA Paper 2011-3757, 2011.

[7] Davies, C., and Arcadi, M., "Planetary Mission Entry Vehicles Quick Reference Guide. Version 3," NASA/SP-2006-3401, January, 2006.

[8] Martin, A., and Boyd, D. I., "Strongly Coupled Computation of Material Response and Nonequilibrium Flow for Hypersonic Ablation," *Journal of Spacecraft and Rockets*, Vol. 52, No. 1, 2015, pp. 89–105.

[9] Amar, A. J., Calvert, D. N., and Benjamin, S. K., "Development and Verification of the Charring ablating Thermal Protection Implicit System Solver," AIAA Thermophysics

Conference Paper, 2011.

[10] Lachaud, J., and Mansour, N. N., “Microscopic scale simulation of the ablation of fibrous materials,” AIAA Paper, 2010-984, 2010.

[11] Martin, A., and Boyd, D. I., “Non-Darcian Behavior of Pyrolysis Gas in a Thermal Protection system,” *Journal of Thermophysics and Heat Transfer*, Vol. 24, No. 1, 2010, pp. 60–68.

[12] Martin, A., and Boyd, D. I., “Modeling of Heat Transfer Attenuation by Ablative Gases During the Stardust Reentry,” *Journal of Thermophysics and Heat Transfer*, Vol. 29, No. 3, 2015, pp. 450–467.

[13] Martin, A., and Boyd, D. I., “Simulation of pyrolysis gas within a thermal protection system,” AIAA Paper, 2008-3805, 2008.

[14] Bouilly, J.-M., Dariol, L., and Leleu, F., “Ablative Thermal Protections for Atmospheric Entry. An Overview of Past Missions and Needs for Future Programmes,” 5th European Workshop on Thermal Protection systems and Hot Structures, Noordwijk, The Netherlands, (ESA SP-631, august 2006).

[15] Martin, A., and Boyd, D. I., “Strongly Coupled Computation of Material Response and Nonequilibrium Flow for Hypersonic Ablation,” AIAA Thermophysics Conference Paper, 2009.

[16] Tran, H., Johnson, C., Rasky, D., Hui, F., Chen, Y. K., and Hsu, M., “Phenolic Impregnated Carbon Ablators (PICA) for Discovery Missions,” NASA TM 110440, April, 1997.

[17] Covington, M. A., Heinemann, M. J., Goldstein, H. E, Chen, Y., -K, Terrazas-Salinas, I., Balboni, J. A., Olejniczak, J., and Martinez, E. R., “Performance of a Low Density Ablative Heat Shield Material,” *Journal of Spacecraft and Rockets*, Vol. 45, No. 2, March–April 2008, pp. 237–247.

[18] Wright, M. J., Beck, R. A. S., Edquist, K. T., Driver, D., Sepka, S. A., Slimko, E. M., Willcockson, W. H., DeCaro, A., and Hwang, H. H., “Sizing and Margins Assessment of the Mars Science Laboratory Aeroshell Thermal Protection System,” AIAA Paper 2009-4231, June 2009.

[19] Fujita, K., Suzuki, T., Ozawa, T., Sakai, T., Dantsuka, T., Ishida, Y., and Watanabe, Y., “Ablation Sensor Unit for Flight Demonstration on HTV Small Recovery Capsule,” AIAA Paper 2017-0899, 2017.

[20] Duffa, G., “Ablative Thermal Protection Systems Modeling,” AIAA Education Series, 2013.

[21] Lachaud, J., Eekelen, T., Scoggins, J. B., Magin, T. E., and Mansour, N. N., “Detailed Chemical Equilibrium Model for Porous Ablative Materials,” *International Journal of Heat and Mass Transfer*, Vol. 90, 2015, pp. 1034–1045.

[22] Kato, S., Okuyama, K., Gibo, K., Miyagi, T., Suzuki, T., Fujita, K., Sakai, T., Nishio, S., and Watanabe, A. “Thermal Response Simulation of Ultra Light Weight Phenolic Carbon Ablator by the Use of the Ablation Analysis Code,” Trans. JSASS Aerospace Tech. Japan, Vol. 10, No. ists28, 2012, pp. 31–39.

[23] Paglia, L., Tirillo, J., Marra, F., Bartuli, C., Simone, A., Valente, T., Pulci, G.,”Carbon-phenolic ablative materials for re-entry vehicles: plasma wind tunnel test and finite element modeling,” *Journal of Materials and Design*, Vol. 90, 2016, pp. 1170–1180.

[24] Harpale, A., Sawant, S., Kumar, R., Levin, D., and Chew, B. H., “Ablative thermal protection systems: Pyrolysis modeling by scale-bridging molecular dynamics,” *Carbon*, Vol. 130, 2018, pp. 315–324.

[25] Park, C., “*Nonequilibrium Hypersonic Aerothermodynamics*,” Wiley, New York, 1990, pp. 349.

[26] Baker, R. L., McDonaugh, J. M., Herr, K. C., Kingberg, R. A., Coffer, J. C., and Covington, M. A., "Carbon Vaporization Condensation Effects," NASA TM 874300, July 1984.

[27] Lachaud, J., Magin, T. E., Cozmuta, I., and Mansour, N. N., "A short review of ablative-material response models and simulation tools," 7th Aerothermodynamics Symposium (European Space Agency), May 2011.

[28] Horiuchi, T., Sakai, T., Fukui, H., Shimamoto, D., Hotta, Y., Ishida, Y., Suzuki, T., and Fujita, K. "Thermal Response Analysis of Porous Carbon-based Non-Ablative Heatshield in An Arcjet Flow Condition," Transactions of Japan Society for Aeronautical and Space Sciences, Vol. 61, No. 5, 2018, pp. 211–218.

[29] Panerai, F., Ferguson, J. C., Lachaud, J., Martin, A., Gasch, M. J., and Mansour, N. N., "Micro-tomography based analysis of thermal conductivity, diffusivity and oxidation behavior of rigid and flexible fibrous insulators," *International Journal of Heat and Mass Transfer*, Vol. 108, 2017, pp. 801–811.

[30] Ferguson, J. C., Panerai, F., Lachaud, J., Martin, A., Bailey, S. C., C., and Mansour, N. N., "Modeling the oxidation of low-density carbon fiber material based on micro-tomography," *Carbon*, Vol. 96, 2016, pp. 57–65.

[31] Borner, A., Panerai, F., and Mansour, N. N., "High temperature permeability of fibrous materials using direct simulation Monte Carlo," *International Journal of Heat and Mass Transfer*, Vol. 106, 2017, pp. 1318–1326.

[32] Hirakawa, M., Abe, K., Nishida, M., Takeishi, K., and Matsuura, M., "Application of a 20 kW Arc-Heated Wind Tunnel to Evaluation Tests of Wall Catalysis," *Trans. Japan Soc. Aeronaut. Space Sci.*, Vol. 45, 2003, pp. 217–223.

[33] Takayanagi, H., Mizuno, M., Fijii, K., Sakai, T., and Fujita, K., "Application of Two-Photon

Absorption Laser-Induced Fluorescence to Atomic Species in the JAXA 750 kW Arc-Heated Wind Tunnel," *Trans. Japan Soc. Aeronaut. Space Sci.*, Vol. 57, 2014, pp. 101–108.

[34] Scott, C. D., "Survey of measurements of flow properties in arcjets," *Journal of Thermophysics and Heat Transfer*, Vol. 7, 1993, pp. 9–24.

[35] Grinstead, J., Stewart, D., and Smith, C., "High enthalpy test methodologies for thermal protection systems development at NASA Ames research center," AIAA 2005–3326, 2005.

[36] De Filippis, F., "SCIROCCO arc-jet facility for large scale spacecraft TPS verification," 55th International Astronnautical Congress, 2004, pp. 1 – 8.

[37] Hinada, M., Inatani, Y., Yamada, T., and Hiraki, K., "An Arc-Heated High Enthalpy Test Facility for Thermal Protection Studies," The Institute of Space and Astronautical Science Report No. 664, March 1996, pp. 1–29.

[38] Fletcher, G. D., "Measurement Requirements for Improved Modeling of Arcjet Facility Flows," Lecture Notes, RTO AVT Course on Measurement Techniques for High Enthalpy and Plasma Flows, 1999.

[39] Sakai, T., "Computational Simulation of High-Enthalpy Arc Heater Flows," *Journal of Thermophysics and Heat Transfer*, Vol. 21, No. 1, 2007, pp. 77–85.

[40] Metzger, J. W., Engel, M. J., and Diaconis, N. S., "Oxidation and Sublimation of Graphite in Simulated Re-entry Environments," *AIAA Journal*, Vol. 5, No. 3, 1967, pp. 451–460.

[41] Schneider, P. J., Dolton, T. A., and Reed, G. W., "Mechanical Erosion of Charring Ablators in Ground-Test and Re-Entry Environments," *AIAA Journal*, Vol. 6, No. 1, 1968, pp. 64–72.

[42] Moyer, C. B., and Rindal, R. A., "An Analysis of the Coupled Chemically Reacting Boundary Layer and Charring Ablator, Part II, Finite Difference Solution for the In-Depth Response of Charring Materials Considering Surface Chemical and Energy Balances," NASA CR-1061,

1968.

[43] Putz, K. E., and Bartlett, E. P., "Heat-Transfer and Ablation-Rate Correlations for Re-Entry Heat-Shield and Nosetip Applications," *Journal of Spacecraft and Rockets*, Vol. 10, No. 1, 1973, pp. 15–22.

[44] Sutton, G. W., "The Initial Development of Ablation Heat Protection, An Historical Perspective," *Journal of Spacecraft and Rockets*, Vol. 19, No. 1, 1982, pp. 3–11.

[45] Reynolds, R. A., Russell, G. W., and Nourse, R. W., "Ablation Performance Characterization of Thermal Protection Materials Using a Mach 4.4 Sled Test," AIAA Paper 92-3055, 1992.

[46] Lachaud, J., Cozmuta, I., and Mansour, N. N., "Multiscale Approach to Ablation Modeling of Phenolic Impregnated Carbon Ablators," *Journal of Spacecraft and Rockets*, Vol. 47, No. 6, 2010, pp. 910–921.

[47] Scoggins, J. B., Rabinovitch, J., Fernandez, B. B., Martin, A., Lachaud, J., Jaffe, R. L., Mansour, N. N., Blanquart, G., and Magin, T., "Thermodynamic properties of carbon-phenolic gas mixtures," *Aerospace Science and Technology*, Vol. 66, 2017, pp. 177–192.

[48] Dec, J. A., Braun, R. D., "An Approximate Ablative Thermal Protection System Sizing Tool for Entry System Design," AIAA Paper 2006-780, 2006.

[49] Vignoles, G. L., and Ortona, A., "Numerical study of effective heat conductivities of foams by coupled conduction and radiation," *International Journal of Thermal Sciences*, Vol. 109, 2016, pp. 270–278.

[50] Almanza, O. A., Rodriguez-Perez, M. A., and De Saja, J. A., "Prediction of the Radiation Term in the Thermal Conductivity of Crosslinked Closed Cell Polylolefin Foams," *Journal of Polymer Science*, Vol. 38, 2000, pp. 993–1004.

[51] Mendes, M. A. A., Ray, S., and Trimis, D., "An improved model for the effective thermal

conductivity of open-cell porous foams," *International Journal of Heat and Mass Transfer*, Vol. 75, 2014, pp. 224–230.

[52] Micco, C. D., and Aldao, C. M., "Radiation Contribution to the Thermal Conductivity of Plastic Foams," *Journal of Polymer Science*, Vol. 43, 2005, pp. 190–192.

[53] Nouri, N., Panerai, F., Tagavi, K. A., Mansour, N. N., and Martin, A., "Evaluation of the anisotropic radiative conductivity of a low-density carbon fiber material from realistic microscale imaging," *International Journal of Heat and Mass Transfer*, Vol. 95, 2016, pp. 535–539.

[54] Chen, Y.-K., Gökçen, T., and Edquist, K. T., "Two-Dimensional Ablation and Thermal Response Analyses for Mars Science Laboratory Heat Shield," *Journal of Spacecraft and Rockets*, Vol. 52, No. 1, January–February 2015, pp. 134–143.

[55] Weng, H., Bailey, S. C., and Martin, A., "Numerical study of iso-Q sample geometric effects on charring ablative materials," *International Journal of Heat and Mass Transfer*, Vol. 80, 2015, pp. 570–596.

[56] Nouri, N., and Martin, A., "Three dimensional radiative heat transfer model for the evaluation of the anisotropic effective conductivity of fibrous materials," *International Journal of Heat and Mass Transfer*, Vol. 83, 2015, pp. 629–635.

[57] Gnoffo, P. A., Johnston, C. O., and Thompson, R. A., "Implementation of Radiation, Ablation, and Free Energy Minimization Modules for Coupled Simulations of Hypersonic Flow," AIAA Paper 2009-1399, 2009.

[58] Cheng, G. C., Venkatachari, B. S., and Cozmuta, I. "Multi-scale simulations of in-depth pyrolysis of charring ablative thermal protection material," *Journal of Computers & Fluids*, Vol. 45, 2011, pp. 191–196.

[59] Helber, B., Chazot, O., Hubin, A., and Magin, T. E., "Emission Spectroscopic Boundary Layer Investigation during Ablative Material Testing in Plasmatron," *J. Vis. Exp*, Issue 112, 2016, pp. 1–11.

[60] Watson, R. V., and Pegot, B. E., "Numerical Calculations for the Characteristics of a Gas Flowing Axially Through a Constricted Arc," NASA TN D-4042, 1967.

[61] Nicolet, W. E., Shepard, C. E., Clark, K. C., Balakrishnan, A., Kesselring, J. P., Suchsland, K. E., and Reese, J. J., "Analytical and Design Study for a High-Pressure, High-Enthalpy Constricted Arc Heater," AEDC-TR-75-47, July, 1975.

[62] Kim, K. H., Rho, O. H., and Park, C., "Computation of Arc-Heated Flows Using a Navier-Stokes Code, *Journal of Thermophysics and Heat Transfer*, Vol. 14, No. 2, 2000, pp. 250–258.

[63] Sakai, T., Ichikawa, S., and Saruhashi, Y., "Computational Simulation of Arc Heater Flows For Martian Atmosphere," *Trans. Japan Soc. Aeronaut. Space Sci.*, Vol. 7, No. ists26, 2009, pp. 43–47.

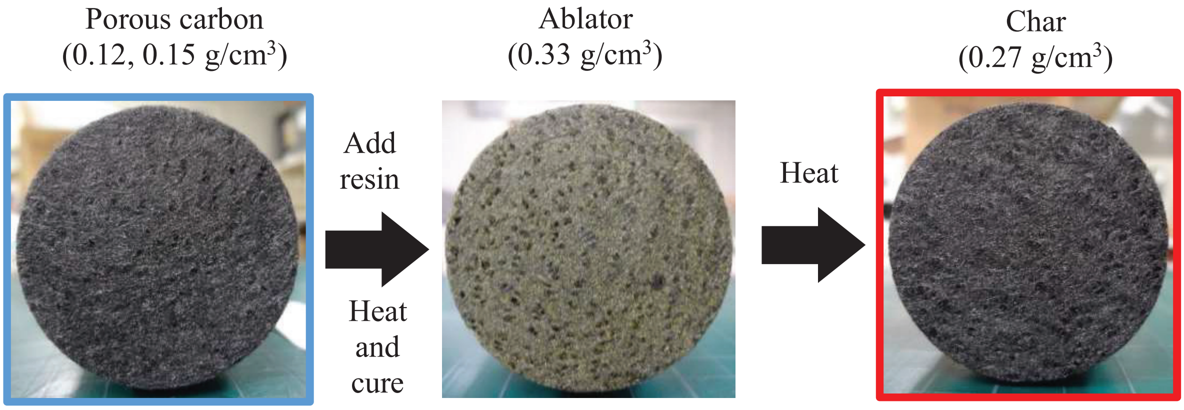

Fig. 1.1 Photographs of the actual test materials

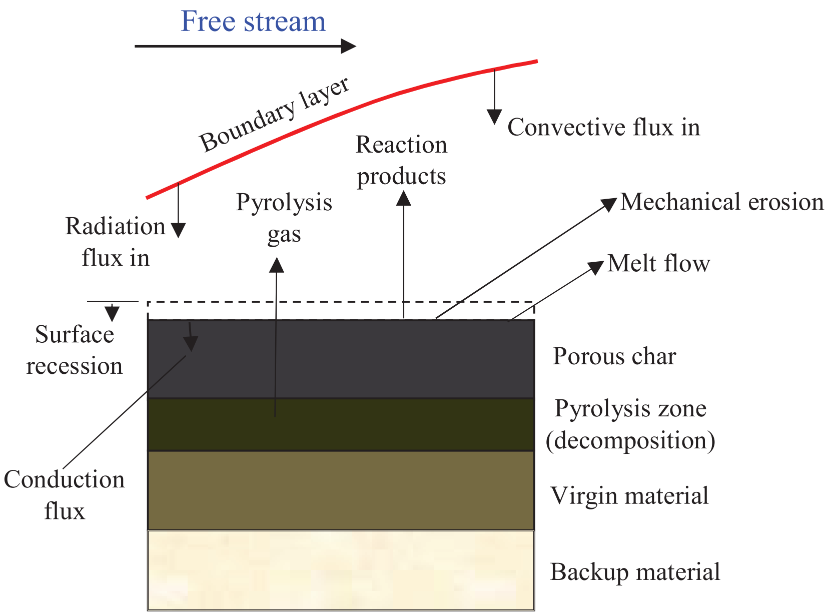

Fig. 1.2 Transformation phases of an ablative material

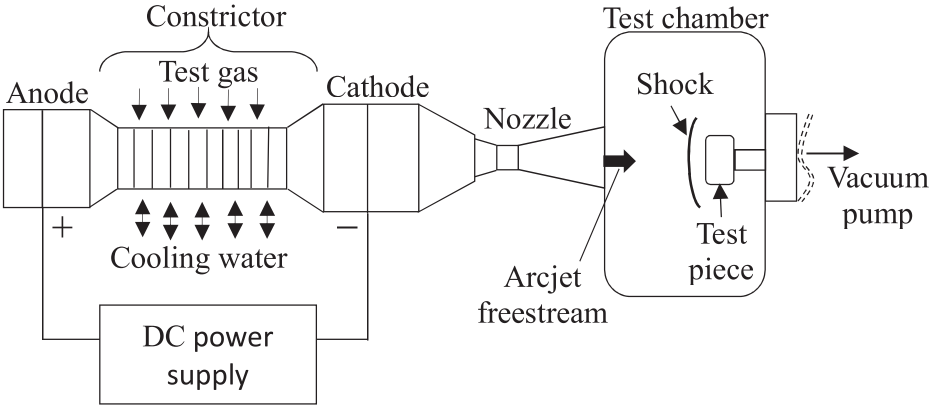

Fig. 1.3 Schematic diagram of a typical constrictor-type arc heated wind tunnel

Chapter 2

Constrictor-type Arc Heated Wind Tunnel Experiments

2.1 Introduction

In this chapter, the operational principle of the arcjet test facility that was used to conduct the experiments is briefly described. Thereafter, the methodology used in preparing the test specimens is explained. Finally, the high enthalpy arc heater experimental conditions and the conditions for the thermal response analysis of porous carbon-based materials are described. Three test specimens of 0.12, 0.15, and 0.27 g/cm^3 densities are used in this study.

2.2 Experimental Setup

2.2.1 Arcjet Test Facility

Heating experiments were conducted using the 1 MW constrictor-type arc heated wind tunnel which is located in ISAS, and managed and operated by JAXA. High enthalpy arc-heated wind tunnels together with the experiments conducted in them have been extensively discussed in the past [1 - 8]. The schematic diagram of a typical constrictor-type arc heated wind tunnel facility has been illustrated earlier in Fig. 1.3. The test gas (nitrogen) is mainly injected from the constrictor section and partly from the two electrode chambers. This gas is then heated through the constrictor section (between the anode and cathode chambers) by an electric discharge. From there, the heated gas is expanded through the convergent-divergent physical nozzle into the material test chamber. Within the test chamber, the test specimen is mounted in position for heating by the heated arcjet freestream. After heating for a prescribed test time, the specimen is retracted and allowed to undergo cooling process. Figure 2.1 shows the photograph of the arc-heated wind tunnel facility in ISAS. Most of the details of this facility, together with its test flow characterization, have been discussed before [9 - 11] and are therefore excluded here. However, we will give the following overview description in this section.

Specifications for the ISAS constrictor-type arc heated wind tunnel facility are given in Table [2.1]. The discharge current and the plenum pressure constitute the independent operational parameters for the facility. The total input power and the mass flow rate, on the other hand, are determined automatically using the fixed hardware configurations like the nozzle throat diameter, and the number of disk packs used [12]. The choice of the nozzle to be used is determined by the amount of heat flux to be achieved during the test. For instance, the smallest nozzle with an exit diameter of 25 mm should be used in order to obtain higher heat flux values. Our experimental test conditions using this wind tunnel are described in section 2.2.3 of the current Chapter.

2.2.2 Preparation of the Test Specimens

In this study, three blunt bodies of highly porous carbon-based materials were used as the test specimens. The test specimen for the 0.12 g/cm^3 material had a configuration of 50 mm diameter and 40 mm length. On the other hand, the 0.15, and 0.27 g/cm^3 test specimens had a configuration of 50 mm diameter and 25 mm length. The corresponding porosity values for these test specimens were 0.93, 0.90 and 0.85, respectively. Both the 0.12 and 0.15 g/cm^3 porous carbon-based specimens were prepared from the rigid carbon insulating materials, manufactured by the Osaka Gas Chemicals Co. Ltd [13]. On the other hand, the 0.27 g/cm^3 porous carbon specimen (Char) was produced through a furnace heat treatment processing of an ablative test specimen. The ablative specimen in this study was developed in-house by impregnating the original porous carbon-based material with polyimide resin. The resulting ablative piece was then subjected to heating in a muffle furnace under a regulated temperature of about 1273 K for about 30 minutes in an inert gas (argon) environment. This heat treatment process resulted into a highly porous char specimen with a density value of 0.27 g/cm^3.

The schematic diagram for the physical configuration of the 0.12 g/cm^3 test specimen is shown in Fig. 2.2 while that for the 0.15, and 0.27 g/cm^3 test specimens is shown in Fig. 2.3. All the test specimens had the same measurement positions. The actual test specimen for the 0.15, and 0.27 g/cm^3 materials is shown in Fig. 2.4 (a). A demonstration of the same test specimen firmly held in position for the heating experiments is shown in Fig. 2.4 (b).

Measurements of the temperature-time history at the stagnation points of the test specimens were conducted using one color pyrometer whereas the in-depth temperature-time histories were measured along the centerline with the aid of Nickel-Chromium K-type thermocouples, attached normal to the axial direction. The test specimens were firmly held in the experimental positions using Bakelite tubes as shown by the 3D illustration in Fig. 2.5. The Bakelite tubes acted as the connecting links between the test specimens and the attachment arm of the arcjet wind tunnel, as can be viewed in Fig. 2.4 (a). The first two thermocouples were attached at the 18 mm, and 23 mm depth positions indicated in both Fig. 2.2 and 2.3. A third thermocouple was placed at the center line of the rear surface in order to monitor the temperature time history at this position. All the three thermocouples are highlighted by the illustration in Fig. 2.5.

2.2.3 Experimental Test Conditions

Experiments were conducted to measure the operational characteristics of the arc heater section of the wind tunnel in ISAS. The measured conditions included: mass flow rate of the test gas, the arc heater power, the arc voltage, the electric current, the pressure at the wall of the arc heater chamber, the mass averaged enthalpy and the thermal efficiency of the arc heater. Stagnation point Pitot pressure and the heat flux values were also measured on a flat-faced cylindrical shaped test specimen within the test chamber. Measurements were made on the test specimen by placing it at various axial positions from the physical nozzle exit. For this case, four sets of measurement were conducted, i.e. at 50, 60, 70, and 80 mm positions. The diameter of the test specimen in this set of experiments was 25 mm.

Another set of experiments were conducted to take similar measurements to the first set of experiments. These experiments were conducted using three different test specimens of 50 mm diameter each and placed at a fixed axial distance of 100 mm from the physical nozzle exit. Measurements were independently taken for each of the test specimens as was explained earlier in section 2.2.2. Thermal response measurements on the test specimens were also taken. On top of the measured conditions in the first set of experiments, other measurements were also taken. These included the nominal Pitot pressure value, the cold wall heat flux, and the stagnation point temperature time history distributions. These measurements were taken at the heating surfaces, at the specific in-depth positions, as well as at the rear surfaces of the test specimens. The arc heater operating conditions were largely similar in the two sets of experiments, with very minimal differences which led to the slight variation in the value of the measured mass averaged enthalpy between the two sets of experiments. A high temperature nitrogen freestream was used in the experiments as the test gas in order to minimize the rate of material recession at the heating surfaces. However, the surfaces actually receded by about 0.3 ± 0.16 mm at the stagnation points of the test specimens. This was mainly caused by the surface reaction processes, largely dominated by nitridation reaction [14, 15]. Table [2.2] and [2.4] present the summaries of the test conditions and measurements for the first and second sets of experiments, respectively

During the experiments, the cold wall heat flux was measured using a 50 mm diameter Gardon gauge, manufactured by the Medtherm Corporation. The heat flux values at the heating surfaces of the test specimens were in the range of 3.2 ± 0.5 MW/m^2. The surface temperature measurements were made using a one-color pyrometer (Micron M90Vx) with a measurement range of 1473 – 4273 K and a wavelength value of 0.65 μm. The test specimens were exposed to heating by the arc heated nitrogen freestream for 10, 15, and 25 s for the 0.12, 0.15, and 0.27 g/cm^3 materials, respectively. Whereas the arcjet mass flow rate was in the range of 18.2 ± 0.3 g/s, the electric current into the arc heater was maintained at about 450 A across all the test cases. The arc heater power was set in the range of 644 ± 7 kW during the first set of experiments, and 740 ± 5 kW in the second set of experiments. The nominal Pitot pressure value within the heating chamber was maintained at 12.6 kPa. The measured mass averaged enthalpy was about 14.7 MJ/kg in the first set of experiments and 15.9 ± 0.4 MJ/kg in the second set of experiments.

Even though the first set of experiments was carried out by specifying both the mass flow rate and the electrical current while measuring the voltage drop in the process, the arc heater input power is included in Table [2.2] because the corresponding calculations for this set of experiments were done by specifying the input power as will be elaborated later in the following Chapters. During the tests, the axial position of the test specimen was changed within the test chamber in order to achieve a variety of heating levels. Both the Pitot pressure and heat flux measurements were done, for each of these operational conditions, using a flat-faced cylindrical probe with a diameter of 25 mm as has been mentioned already in sub-section 2.2.1 of this Chapter. For the pressure measurements, pressure gauges were mounted at three different locations, i.e. r = 0, 4.5, and 9 mm, along the radial direction from the centerline of the test specimen. In the first set of experiments, only the stagnation point heat flux values were measured using a 25 mm diameter Gardon gauge. Therefore, unlike the pressure, the heat flux radial profile data is unavailable. The measured data at various axial and radial test positions are summarized in Table [2.3].

References

[1] Scott, C. D., “Survey of measurements of flow properties in arcjets,” *Journal of Thermophysics and Heat Transfer*, Vol. 7, 1993, pp. 9–24.

[2] Grinstead, J., Stewart, D., and Smith, C., “High enthalpy test methodologies for thermal protection systems development at NASA Ames research center,” AIAA 2005–3326, 2005.

[3] De Filippis, F., “SCIROCCO arc-jet facility for large scale spacecraft TPS verification,” 55th International Astronnautical Congress, 2004, pp. 1 – 8.

[4] Hirakawa, M., Abe, K., Nishida, M., Takeishi, K., and Matsuura, M., “Application of a 20 kW Arc-Heated Wind Tunnel to Evaluation Tests of Wall Catalysis,” *Trans. Japan Soc. Aeronaut. Space Sci.*, Vol. 45, 2003, pp. 217–223.

[5] Takayanagi, H., Mizuno, M., Fijii, K., Sakai, T., and Fujita, K., “Application of Two-Photon Absorption Laser-Induced Fluorescence to Atomic Species in the JAXA 750 kW Arc-Heated Wind Tunnel,” *Trans. Japan Soc. Aeronaut. Space Sci.*, Vol. 57, 2014, pp. 101–108.

[6] Sakai, T., “Computational Simulation of High-Enthalpy Arc Heater Flows,” *Journal of Thermophysics and Heat Transfer*, Vol. 21, No. 1, 2007, pp. 77–85.

[7] Takahashi, Y., Abe, T., Takayanagi, H., Mizuno, M., Kihara, H., and Abe, K., “Advanced Validation of Nonequilibrium Plasma Flow Simulation for Arc-Heated Wind Tunnels,” *Journal of Thermophysics and Heat Transfer*, Vol. 28, No. 1, 2014, pp. 9–17.

[8] Bendoukha, S. A., Okuyama, K., Szasz, B., and Shimoda, T., “Experimental Method using Arc Wind Tunnel to simulate a New Technique for Communicating with a Reentry Probe Having a Thermal Shield made of LATS Materials,” *International Journal of Research - Granthaalayah*, Vol. 5, Issue 2, 2017, pp. 1–12.

[9] Hinada, M., Inatani, Y., Yamada, T., and Hiraki, K., “An Arc-Heated High Enthalpy Test

Facility for Thermal Protection Studies," The Institute of Space and Astronautical Science Report No. 664, March 1996, pp. 1–29.

[10] Ahn, H.-K., Park, C., and Sawada, K., "Response of Heatshield Material at Stagnation Point of Pioneer-Venus Probe," *Journal of Thermophysics and Heat Transfer*, Vol. 16, 2002, pp. 432–439.

[11] Yamada, T., and Inatani, Y., "ISAS High Enthalpy Flow Facility for Thermal Protection Materials Tests," IEPC-99-233, 26th International Electric Propulsion Conference, Kitakyushu, Japan, Oct. 17 – 21 1999.

[12] Yamada, T., and Inatani, Y., "Arc Heating Facility and Test Technique for Planetary Entry Missions," The Institute of Space and Astronautical Science Report SP No. 17, March, 2003, pp. 147–163.

[13] Anon., Osaka Gas Chemicals Co., Ltd., "S-242," http://www.ogc.co.jp/e/products/carbon-f/ [Retrieved 25 May 2016].

[14] Suzuki, T., Fujita, K., Ando, K., and Sakai, T., "Experimental Study of Graphite Ablation in Nitrogen Flow," *Journal of Thermophysics and Heat Transfer*, Vol. 22, 2008, pp. 382–389.

[15] Suzuki, T., Fujita, K., and Sakai, T., "Experimental Study of Graphite Ablation in Nitrogen Flow, Part II: Further Numerical Analysis," *Journal of Thermophysics and Heat Transfer*, Vol. 24, 2010, pp. 589–597.

Table [2. 1] Specifications for the 1 MW constrictor-type arc heating facility in ISAS

Description	Specification
Constrictor inner diameter, mm	25
Throat diameter, mm	10
Nozzle exit diameter, mm	25, 40, 110
Ratio of nozzle exit areas to throat area, A_e/A_t	6.25, 16, 121
Mass flow rate, g/s	10 ~ 30
Maximum input power, kW	1000
Arc voltage, V	~2000
Electric current, A	300 ~ 700
Impact pressure, kPa	5 ~ 70
Flow enthalpy, MJ/kg	3 ~ 20

Table [2. 2] Arc heater measured data in the first experiments

Test condition/ measurement	Measured values
Mass flow rate, g/s	18.6
Input power, kW	644 ± 7
Arc voltage, V	1436 ± 5
Electric current, A	449 ± 4
Chamber wall pressure, kPa	510 ± 1
Mass average enthalpy, MJ/kg	14.7
Thermal efficiency, %	42

Table [2. 3] Test chamber measured data in the first experiments

Axial distance from nozzle exit, mm	Pitot pressure, kPa			Heat flux, MW/m^2
	$r = 0$ mm	4.5 mm	9 mm	
50	50.9 ± 0.3	48.0 ± 0.8	38.9 ± 0.1	14.0 ± 0.1
60	39.7 ± 0.3	40.0 ± 0.8	30.3 ± 0.2	13.6 ± 0.3
70	29.8 ± 0.8	27.2 ± 0.2	22.6 ± 0.4	9.7 ± 0.2
80	20.3 ± 0.1	19.2 ± 0.1	16.7 ± 0.1	6.5 ± 0.2

Table [2. 4] Measured data in the second experiments (* denotes the nominal value)

Material density, g/cm^3	Test gas, -	Electric current, A	Input power, kW	Mass flow rate, g/s	Heating time, s	Mass average enthalpy, MJ/kg	Pitot pressure, kPa	Cold wall heat flux, MW/m^2
0.12	N_2	449 ± 4	740 ± 5	18.2 ± 0.3	10	15.9 ± 0.4	12.6*	3.2 ± 0.5
0.15					15			
0.27					25			

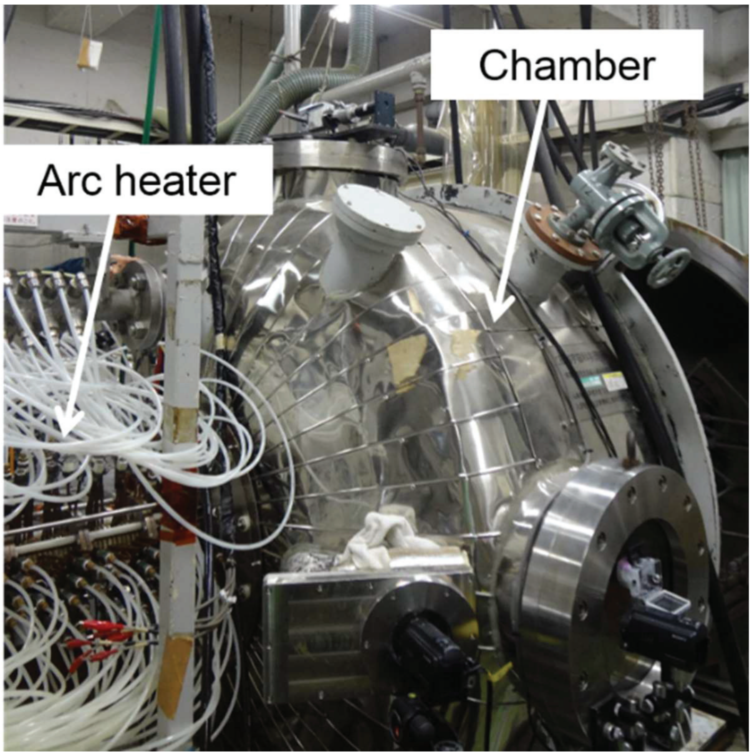

Fig. 2.1 The 1 MW constrictor-type arc heated wind tunnel at ISAS

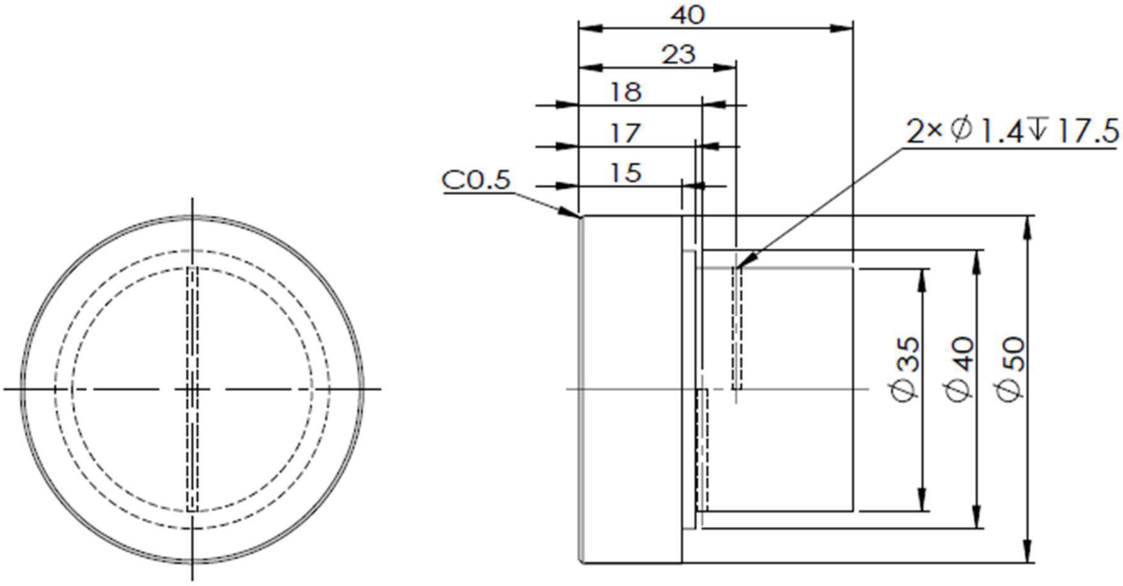

Fig. 2.2 Configuration for the 0.12 g/cm^3 test specimen

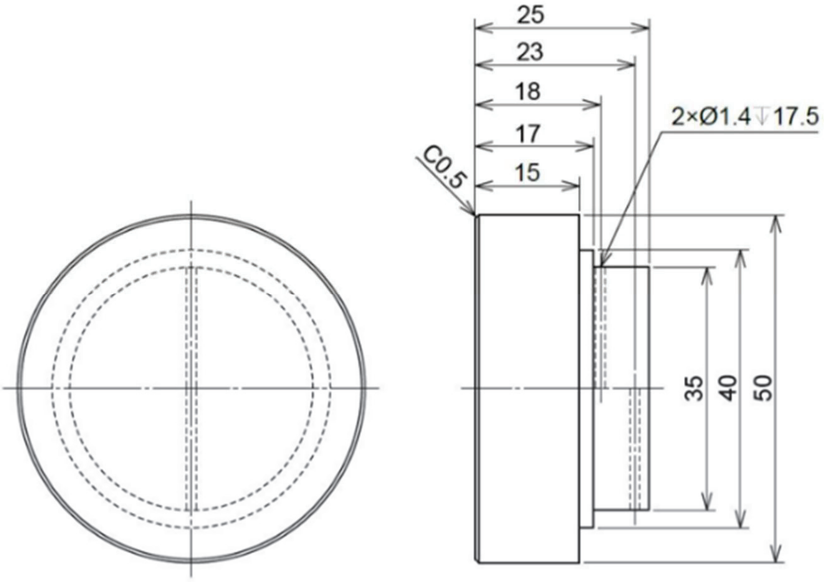

Fig. 2.3 Configuration for the 0.15 and 0.27 g/cm^3 test specimens

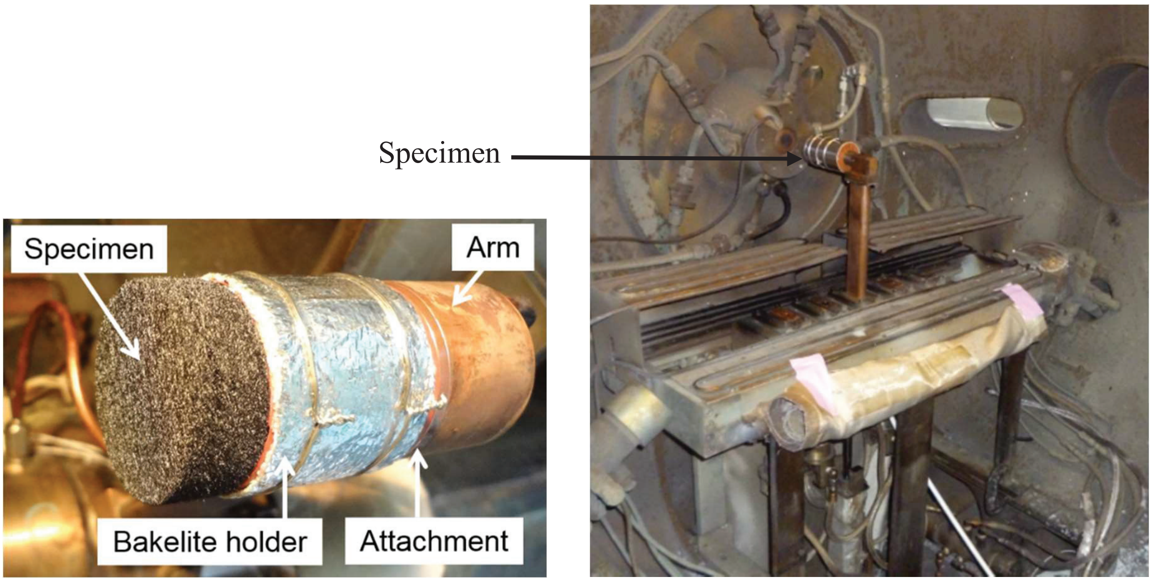

(a) Test specimen attachment (b) Specimen experimental position

Fig. 2.4 Experimental attachment methodology for the test specimens

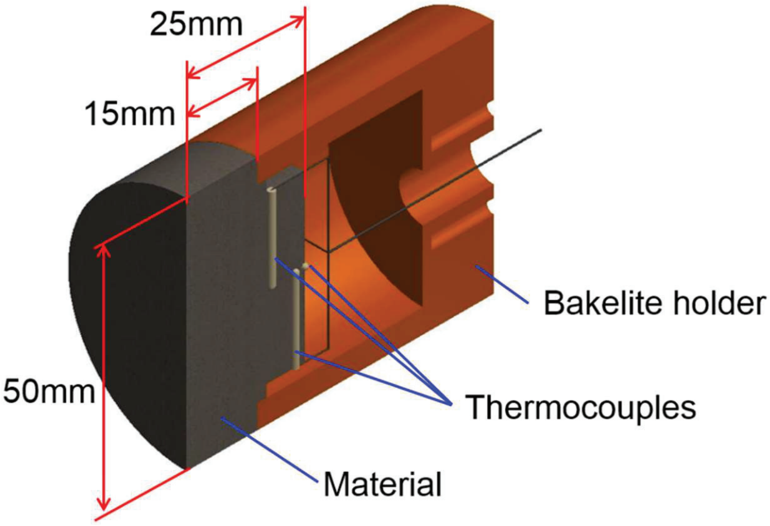

Fig. 2.5 Illustration of the Bakelite attachment to the test specimen

Chapter 3

Numerical Method

3.1 Introduction

The final goal of this chapter is to analyze the thermal response of porous carbon-based materials subjected to arcjet heating environments. In order to achieve this, a high-fidelity numerical method was developed. This methodology was aimed at solving, in two-dimensional axisymmetric form, the flow field and the material response in a coupled manner. It was also expected to account for the radial non-uniformity in the distribution of arcjet freestream along the heating surface of the test specimen.

In this chapter, numerical analyses of the flow field properties within the arc heater and the test chamber sections are first described using a set of codes named ARCFLO3+. This code set combines three codes and analyzes flow sequentially from the arc heater section, the nozzle section, to the test chamber section. The calculated flow distribution results at the downstream of arc heater section are imposed as the boundary conditions at the entrance of the nozzle section for the analysis of flow therein. Finally, the flow distribution results at the nozzle exit are imposed as the input boundary conditions for the flow analysis within the test chamber section. For the arc heater flow field analysis, a thermochemical equilibrium code known as ARCFLO3 was applied. The test chamber flow field, on the other hand, was analyzed using a thermochemical nonequilibrium code set as described later in this chapter. Radiative heating by the arcjet freestream was estimated using a three-band gray-gas model described in section 3.2.2 below. The flow field calculation codes were then validated using the experimentally obtained data, already explained in Chapter 2, before conducting the final thermal response analysis of the test specimens.

The thermal response of each of the test specimens was analyzed following two different numerical approaches. In the first approach, only the solid material's energy conservation equation was solved in a two-dimensional axisymmetric form, through a coupling method between the flow field and material response simulations. Conservation equations for the gas mass, momentum and energy were ignored in this approach and therefore, by extension, leaving out the convective transport contribution to the overall heat transfer. The main reason for this approach was because the objective in this case was to mainly investigate the contribution of radiative heat transfer within the test materials. Hence, in this approach, only Eq. (3.78) of the governing equations in section 3.4.1 of this Chapter was solved.

However, independent arcjet experiments were done by setting the pressure transducers both at the inside and outside of the experimental attachment arm as illustrated in Fig. 3.1. This was done in order to monitor the pressure-time history at the rear surface of the test specimen. Two sets of experiments were conducted for this purpose. Results from the two sets of experiments, represented by the continuous and dotted graphs, reported an increase in pressure during the arcjet flow heating as shown in Fig. 3.2. These results strongly indicated the possibility of gas flow through the pores of the test specimen. This motion of the gas was likely to have originated from the incoming arcjet freestream. These observations suggested that the convective energy transfer through the gas motion within the pores was capable of augmenting the overall thermal transfer within the test materials.

The above results motivated our desire to investigate further the role of convective transfer in the overall heat transfer process within the porous carbon-based materials. Therefore, the second approach in the analysis of the material thermal response was instigated. In this approach, a preliminary thermal response analysis was conducted by coupling conductive, radiative, and convective energy transports in a separately developed numerical calculation model. In this new model, the mass, momentum, and energy conservation equations for the gas were incorporated in the governing equations, and then solved alongside the solid material's energy conservation equation, basically solving all the governing equations as expressed in Eq. (3.74) to Eq. (3.78) in section 3.4.1 of the current Chapter. However, these calculations were carried out in an uncoupled manner, owing to the elaborate and exhaustive coupling procedure between the CFD flow and material response codes.

3.2 Physical and Numerical Models for the Arc Heater Flow Field

3.2.1 Governing Equations

Axisymmetric viscous flow in the arc heater section was calculated using ARCFLO3 code to solve mass, momentum, and total energy conservation equations by assuming thermochemical equilibrium within the flow field. In this code, eleven chemical species air model was used with a look up table to calculate the thermodynamic properties at the high temperature state of the gas mixture. However, since our current study utilized nitrogen as the test gas, the look up table was modified to contain the elemental mass fractions of both nitrogen and oxygen, with an assumed negligible contribution from the oxygen-bearing species. The thermochemical equilibrium properties of the gas were calculated using the free energy minimization method. The governing conservation equations for solving the radiative flow field in the arc heater section were expressed as shown in Eq. (3.1).

$$\frac{\partial Q}{\partial t}+\frac{\partial\left(E-E_{vis}\right)}{\partial x}+\frac{\partial\left(F-F_{vis}\right)}{\partial y}+\frac{1}{y}\left(H-H_{vis}\right)=F_{rad} \tag{3.1}$$

Components of the conservative variables Q, inviscid flux vectors E and F, viscous flux vectors E_{vis} and F_{vis}, as well as the inviscid and viscous axisymmetric source terms H and H_{vis} respectively, were given as shown in Eq. (3.2) below. F_{rad} in Eq. (3.1) above refers to the radiative source term.

$$\begin{gathered}
Q=\begin{bmatrix}\rho\\ \rho u\\ \rho v\\ e\end{bmatrix};E=\begin{bmatrix}\rho u\\ \rho u^2+p\\ \rho uv\\ \left(e+p\right)u\end{bmatrix};F=\begin{bmatrix}\rho v\\ \rho uv\\ \rho v^2+p\\ \left(e+p\right)v\end{bmatrix};H=\begin{bmatrix}\rho v\\ \rho uv\\ \rho v^2\\ \left(e+p\right)v\end{bmatrix}\\
E_{vis}=\begin{bmatrix}0\\ \tau_{xx}\\ \tau_{xy}\\ \tau_{xx}u+\tau_{xy}v-q_x\end{bmatrix};F_{vis}=\begin{bmatrix}0\\ \tau_{yx}\\ \tau_{yy}\\ \tau_{yx}u+\tau_{yy}v-q_y\end{bmatrix};H_{vis}=\begin{bmatrix}0\\ \tau_{xy}\\ \tau_{y\theta}\\ \tau_{xy}u+\tau_{yy}v-q_y\end{bmatrix}
\end{gathered} \tag{3.2}$$

The shear stresses in Eq. (3.2) were evaluated by following the bulk viscosity assumption by Stokes, in which the shear stresses are taken to be directly proportional to the first derivative of the mass averaged velocities. Therefore, the shear stress tensors were expressed as follows:

$$\tau_{xx}=\frac{2}{3}\mu\left(2\frac{\partial u}{\partial x}-\frac{\partial v}{\partial y}-\frac{v}{y}\right) \tag{3.3}$$

$$\tau_{xy}=\tau_{yx}=\mu\left(\frac{\partial u}{\partial y}+\frac{\partial v}{\partial x}\right) \tag{3.4}$$

$$\tau_{yy}=\frac{2}{3}\mu\left(2\frac{\partial v}{\partial y}-\frac{\partial u}{\partial x}-\frac{v}{y}\right) \tag{3.5}$$

$$\tau_{y\theta} = 2\mu\left(\frac{\partial v}{\partial y} - \frac{v}{y}\right) \tag{3.6}$$

3.2.2 Radiation Model

Radiative heat fluxes at the wall of the constrictor section in an arc heater are generally evaluated using a multi-band model. Accuracy inadequacies of the two-band model that was developed earlier led to the birth of the three-band radiation model [1] applied in this study. This new model was developed based on the Planck-Rosseland-Gray (PRG) model. In the PRG model, an absorption coefficient at a given point and wavelength in a flow field is classified into either Planck, Rosseland or Gray-gas group based on a local optical depth. The mean absorption coefficient for the three groups is evaluated through integration in wavelength. Radiative heat flux is calculated separately for each group and the total heat flux is obtained by the sum of the individual heat fluxes. In this study, a similar approach was used in modeling of the radiation. However, instead of applying the PRG model groups, this model solely divided the Gray-gas into three groups and the absorption coefficients were classified a priori into appropriate groups.

The radiative transport equation in cylindrical coordinates [2] was solved using a temperature-dependent three-band model. It should be noted that this three-band model has the capability of reproducing the line-by-line calculation results by accounting for the important radiation mechanisms for the high temperature air. The general governing equation for radiation is expressed as follows,

$$\frac{dI_\lambda}{ds_p} = \kappa_\lambda\left(B_\lambda - I_\lambda\right) \tag{3.7}$$

where, I_λ refers to the intensity of radiation traveling along a ray path s_p, κ_λ is the absorption coefficient at a given wavelength λ and B_λ is the Planck's function at a given wavelength λ. The total radiative heat flux q is determined by integrating I_λ over a solid angle $d\Omega$ at all the wavelength regions. This is expressed in Eq. (3.8).

$$q_\lambda(r) = \int I_\lambda(r)\cos\alpha d\Omega \tag{3.8}$$

When Eq. (3.7) is integrated and substituted into Eq. (3.8), the resulting expression is as shown in Eq. (3.9) [3].

$$q_\lambda(r) = q_\lambda^+(r) + q_\lambda^-(r) \tag{3.9}$$

In Eq. (3.9) above, $q_\lambda^+(r)$ and $q_\lambda^-(r)$ are the radiative heat fluxes toward and away from point *r*, respectively. For the gray-gas model, and taking the direction toward *r* to be positive, the net heat flux in each of the three groups was calculated by finding the difference between the heat fluxes toward and away from point *r* as shown in Eq. (3.10).

$$q_{G_i}(r) = q_{G_i}^+(r) - q_{G_i}^-(r) \tag{3.10}$$

Where $i = 1,2,3$. The values of $q_{G_i}^+(r)$ and $q_{G_i}^-(r)$ were evaluated using Eqs. (3.11) and (3.12), respectively.

$$q_{G_i}^+(r) = 4\int_0^{\frac{\pi}{2}} \left\{ \begin{array}{l} B_G(R)D_3\left(\int_0^{rcos\gamma}\kappa_G dy + \int_0^{\sqrt{R^2-r^2sin^2\gamma}}\kappa_G dy\right) \\ +\int_0^{rcos\gamma}\kappa_G B_G D_2\left(\int_y^{rcos\gamma}\kappa_G dy'\right)dy \\ +\int_0^{\sqrt{R^2-r^2sin^2\gamma}}\kappa_G B_G D_2\left(\int_0^{rcos\gamma}\kappa_G dy' + \int_0^{y}\kappa_G dy'\right)dy \end{array} \right\} cos\gamma d\gamma \tag{3.11}$$

$$q_{G_i}^{-}(r) = -4\int_0^{\frac{\pi}{2}} \left\{ \begin{aligned} & B_G(R)\, D_3\left(\int_{rcos\gamma}^{\sqrt{R^2 - r^2 sin^2\gamma}} \kappa_G dy \right) \\ & + \int_{rcos\gamma}^{\sqrt{R^2 - r^2 sin^2\gamma}} \kappa_G B_G \times D_2 \left(\int_{rcos\gamma}^{y} \kappa_G dy' \right) dy \end{aligned} \right\} cos\gamma d\gamma \tag{3.12}$$

The geometrical parameters for the cylindrical coordinates used in Eqs. (3.11) and (3.12) above are given in Fig. 3.3. The total radiative heat flux in the gray-gas model was defined as the sum of the net heat flux in the individual gas groups, which can be expressed as follows.

$$q_G(r) = \sum_{i=1}^{3} \left(q_{G_i}^{+}(r) - q_{G_i}^{-}(r) \right) \tag{3.13}$$

The overall absorption coefficient of the gas mixture was given by the sum of the individual species coefficients [4] as shown in Eq. (3.14).

$$\begin{aligned} \sigma_{\lambda,s} &= exp\left(\frac{A_{\lambda 1}^{s}}{z} + A_{\lambda 2}^{s} + A_{\lambda 3}^{s} \ln z + A_{\lambda 4}^{s} z + A_{\lambda 5}^{s} z^2 \right) \\ Z &= \frac{10^4}{T_v} \end{aligned} \tag{3.14}$$

3.2.3 Validation of the Arc Heater Calculation Code

Accuracy of all the components of the CFD flow codes in this study were validated using their respective experimental data. The ARCFLO3 code used to calculate the arc heater flow field was validated by comparing the computed results with the corresponding experimental data, particularly, the mass averaged enthalpy. Since the two sets of experiments were conducted with specimens of different configurations (i.e. 25, and 50 mm diameters), two independent validations were carried out in the arc heater section. Initially, the computed results which were calculated using the originally measured electrical power input slightly overestimated the measured mass averaged enthalpy. Therefore, in a bid to harmonize this anomaly, the power input to the code set was controlled through a trial and error approach to eventually achieve a fair agreement between the calculation and the measurement. For the 25 mm diameter blunt body case, the calculated mass averaged enthalpy was 14.41 MJ/kg and for the 50 mm diameter specimen, this value was estimated to be 15.5 MJ/kg. Comparing these values against their corresponding measured values in Table 2.2 and Table 2.4, respectively, in Chapter 2, it can be stated confidently that the ARCFLO3 code was valid enough for application in our study.

3.3 Physical and Numerical Models for Nozzle and Shock Layer Flow Fields

3.3.1 Governing Equations

The shock layer flow field over the test specimen was assumed to be thermochemical nonequilibrium. Chemical species such as N, N_2, N^+, N_2^+, C, CN, C_3, and C^+ were included in the calculation to simulate the high temperature nitrogen flow with the ablation product species. A computer code developed in the past to calculate the thermal response of ablative materials [5] was used in this study. This code was able to simulate the possible surface reactions attributed to the present calculated results. Such reactions included the surface recombination of the atomic nitrogen, nitridation, and sublimation as given in Eq. (3.15), (3.16), and (3.17), respectively. Both reactions in Eq. (3.16), and (3.17) can lead to the surface recession of the test materials.

$$N + N \rightarrow N_2 \tag{3.15}$$

$$C + N \rightarrow CN \tag{3.16}$$

$$3C \rightarrow C_3 \tag{3.17}$$

In the measurements, a small amount of surface recession was observed. Our study calculation was also used to reproduce the experimentally obtained surface contours for the test specimens, as will be shown later.

The mass fluxes of CN and $\mathrm{C_3}$ were evaluated by following the approach used by Sakai *et. al*. [6] as given in Eqs. (3.18), and (3.19), respectively.

$$J_{\mathrm{CN}} = \left(\frac{M_{\mathrm{CN}}}{M_{\mathrm{N}}}\right)\rho_{\mathrm{N}}\alpha_{\mathrm{nit}}\sqrt{\frac{\hat{R}T_w}{2\pi M_{\mathrm{N}}}} \tag{3.18}$$

$$J_{\mathrm{C_3}} = \frac{\alpha_{\mathrm{sub}}\max\left(0, P_{\mathrm{e,C_3}} - P_{\mathrm{C_3}}\right)}{\sqrt{\dfrac{2\pi\hat{R}T_w}{M_{\mathrm{C_3}}}}} \tag{3.19}$$

where: M_{CN} , M_{N} , $M_{\mathrm{C_3}}$ represent the atomic weights for species CN, N, and C_3 in kg/mol, respectively. $\hat{R}$ is the universal gas constant in J/(mol-K), T_w is the wall temperature in K, ρ_{N} is the density for species N in kg/m^3, and $P_{\mathrm{C_3}}$ represents the vapor pressure, in Pa, for the C_3 species. The equilibrium vapor pressure $P_{\mathrm{e,C_3}}$ in Eq. (3.19) was similarly expressed as in Ref. [5]. The reaction probabilities for the nitridation and sublimation processes are given as follows in Eqs. (3.20) and (3.21), respectively:

$$\alpha_{\mathrm{nit}} = 8.441\times10^{-3}\exp\left(\frac{-2322}{T_w}\right) \tag{3.20}$$

$$\alpha_{\mathrm{sub}} = 0.023 \tag{3.21}$$

The atomic nitrogen recombination at the ablating surface of the test specimen was calculated by imposing either a non-catalytic or finite catalytic condition. The finite catalytic value was determined through a trial and error approach as will be explained in the next Chapter for the Results and Discusion.

Axisymmetric viscous flow within the test chamber was calculated using Navier-Stokes equations that incorporated the elemental density conservation equations, and at the same time assuming thermochemical nonequilibrium reactions within the flow field. In the study, eleven chemical species for high temperature air ($N, O, N_2, O_2, NO, N^+, O^+, N_2^+, O_2^+, NO^+, e^-$) and ten chemical species for ablation products ($C, C_2, C_3, CN, CO, C^+, H, H_2, C_2H, H^+$) were assumed and a look up table was implemented to calculate the thermodynamic properties at the high temperature state of the gas mixtures. A modification of the thermodynamic table was similarly done to accommodate our nitrogen test gas, as has been explained earlier.

In this study, a constant elemental ratio of the freestream gas in the entire computational domain was assumed. Therefore, the concept of elemental density conservation equations that was proposed by Park [7] was applied. Instead of solving the conservation equations for all the species above, equations for the elemental densities of N, O, C, H, which were expressed as $\tilde{\rho}_N, \tilde{\rho}_O, \tilde{\rho}_C, \tilde{\rho}_H$ respectively, were introduced and at the same time an equal number of the species conservation equations were eliminated. The densities of the chemical species were related to the above elemental densities by the following expressions:

$$\frac{\tilde{\rho}_N}{M_N} = \frac{\rho_N}{M_N} + 2\frac{\rho_{N_2}}{M_{N_2}} + \frac{\rho_{NO}}{M_{NO}} + \frac{\rho_{N^+}}{M_{N^+}} + 2\frac{\rho_{N_2^+}}{M_{N_2^+}} + \frac{\rho_{NO^+}}{M_{NO^+}} + \frac{\rho_{CN}}{M_{CN}} \tag{3.22a}$$

$$\frac{\tilde{\rho}_O}{M_O} = \frac{\rho_O}{M_O} + 2\frac{\rho_{O_2}}{M_{O_2}} + \frac{\rho_{NO}}{M_{NO}} + \frac{\rho_{O^+}}{M_{O^+}} + 2\frac{\rho_{O_2^+}}{M_{O_2^+}} + \frac{\rho_{NO^+}}{M_{NO^+}} + \frac{\rho_{CO}}{M_{CO}} \tag{3.22b}$$

$$\frac{\tilde{\rho}_C}{M_C} = \frac{\rho_C}{M_C} + 2\frac{\rho_{C_2}}{M_{C_2}} + \frac{\rho_{CN}}{M_{CN}} + \frac{\rho_{CO}}{M_{CO}} + 3\frac{\rho_{C_3}}{M_{C_3}} + \frac{\rho_{C^+}}{M_{C^+}} + 2\frac{\rho_{C_2H}}{M_{C_2H}} \tag{3.22c}$$

$$\frac{\tilde{\rho}_H}{M_H} = \frac{\rho_H}{M_H} + 2\frac{\rho_{H_2}}{M_{H_2}} + \frac{\rho_{C_2H}}{M_{C_2H}} + \frac{\rho_{H^+}}{M_{H^+}} \tag{3.22d}$$

The M_s in the above set of equations denoted the molecular weight of the species s with their values specified in Table 3.1. The assumption made in this case was that the number density of each element was constant as mentioned earlier. Hence, the overall density of the flow ρ was given by the total sum of the individual elemental densities as expressed in Eq. (3.23).

$$\rho = \tilde{\rho}_N + \tilde{\rho}_O + \tilde{\rho}_C + \tilde{\rho}_H \tag{3.23}$$

The total number of equations at this point are 26, that is, 21 species conservation equations, 4 elemental density conservation equations and the total density conservation equation. The density conservation equations for the 4 species $N_2, O_2, C_2,$ and H_2 were removed and instead, their density conservation equations were determined by solving Eq. (3.22). Again, Eq. (3.23) was used to replace the total density conservation equation. In that sense, only 17 conservation equations for the chemical species and 4 elemental density conservation equations for the 21 species, together with two conservation equations for momentum, the total energy conservation equation, and the conservation equation for vibrational-electronic energy were solved. These conservation equations were solved using Navier-Stokes equations, and expressed in two-dimensional axisymmetric form as shown in Eq. (3.24).

$$\frac{\partial Q}{\partial t} + \frac{\partial E}{\partial x} + \frac{\partial F}{\partial y} + \frac{1}{y} H = W \tag{3.24}$$

From Eq. (3.24), Q is the vector defining conservative variables, E and F are the convective flux vectors, H is the vector for the axisymmetric flow source terms and W is the source vector. Within E, F, and H, existed their respective inviscid and viscous flux vectors given by the expressions in Eq. (3.25).

$$E = \left(E_{inv} - E_{vis}\right) \tag{3.25a}$$

$$F = \left(F_{inv} - F_{vis}\right) \tag{3.25b}$$

$$H = \left(H_{inv} - H_{vis}\right) \tag{3.25c}$$

Individual components of the above vectors were defined using the expressions given in Eq. (3.26) below.

$$Q = \begin{bmatrix} \tilde{\rho}_s \\ \rho_s \\ \rho u \\ \rho v \\ E_t \\ E_v + E_e \end{bmatrix}; E_{inv} = \begin{bmatrix} \tilde{\rho}_s u \\ \rho_s u \\ \rho u^2 + p \\ \rho uv \\ \left(E_t + p\right)u \\ \left(E_v + E_e\right)u \end{bmatrix}; F_{inv} = \begin{bmatrix} \tilde{\rho}_s v \\ \rho_s v \\ \rho uv \\ \rho v^2 + p \\ \left(E_t + p\right)v \\ \left(E_v + E_e\right)v \end{bmatrix}; H_{inv} = \begin{bmatrix} \tilde{\rho}_s v \\ \rho_s v \\ \rho uv \\ \rho v^2 \\ \left(E_t + p\right)v \\ \left(E_v + E_e\right)v \end{bmatrix}; W = \begin{bmatrix} 0 \\ W_s \\ 0 \\ 0 \\ 0 \\ W_v \end{bmatrix} \tag{3.26}$$

$$E_{vis} = \begin{bmatrix} \tilde{\rho}_s u_s \\ \rho_s u_s \\ \tau_{xx} \\ \tau_{yx} \\ \tau_{xx}u + \tau_{xy}v - q_x - q_{v_x} - \sum_s \rho_s u_s h_s \\ -q_{v_x} - \sum_s \rho_s u_s e_{v,s} \end{bmatrix}; F_{vis} = \begin{bmatrix} \tilde{\rho}_s v_s \\ \rho_s v_s \\ \tau_{xy} \\ \tau_{yy} \\ \tau_{yx}u + \tau_{yy}v - q_y - q_{v_y} - \sum_s \rho_s v_s h_s \\ -q_{v_y} - \sum_s \rho_s v_s e_{v,s} \end{bmatrix}; H_{vis} = \begin{bmatrix} \tilde{\rho}_s v_s \\ \rho_s v_s \\ \tau_{xy} \\ \tau_{y\theta} \\ \tau_{xy}u + \tau_{yy}v - q_y - q_{v_y} - \sum_s \rho_s v_s h_s \\ -q_{v_y} - \sum_s \rho_s v_s e_{v,s} \end{bmatrix}$$

To evaluate the shear stresses in the above equations, Stokes' assumption for bulk viscosity was utilized. Therefore, the shear stress tensors were similarly expressed as in Eqs. (3.3) – (3.6). The conduction heat flux vectors in this study were evaluated by following Fourier's law of heat conduction as expressed in Eq. (3.27).

$$q_x = -k\frac{\partial T}{\partial x} \tag{3.27a}$$

$$q_y = -k\frac{\partial T}{\partial y} \tag{3.27b}$$

$$q_{v_x} = -k_v \frac{\partial T_v}{\partial x} \tag{3.27c}$$

$$q_{v_y} = -k_v \frac{\partial T_v}{\partial y} \tag{3.27d}$$

3.3.2 Transport Coefficients

Blottner *et. al*. [8], developed a viscosity model for the reacting flows in order to evaluate the viscosity of the individual species within flows. The same model was applied in our study to determine the species' viscosities within the flow, excluding the electron viscosity which was evaluated using an approach of curve fitting by Ahn *et. al*. [9]. The respective expressions for the species' viscosities and the electron viscosity were given by Eqs. (3.28) and (3.29).

$$\mu_{l,s} = 0.1 exp\left[\left(A_s \ln T + B_s\right)\ln T + C_s\right] \tag{3.28}$$

$$\mu_{l,e^-} = A_{e^-}\left(\frac{T}{300}\right)^{0.8} \tag{3.29}$$

The values of A_s, B_s, C_s, and A_{e^-} are defined in Table [3.2].

The translational-rotational and vibrational-electronic temperature conductivities were evaluated following Eucken's relation which was postulated by Vincenti and Kruger [10]. From the relation, the translational-rotational and vibrational-electronic conductivities could be defined by the expressions given in Eq. (3.30a) and (3.30b), respectively:

$$k_{l,s} = \mu_{l,s}\left(\frac{5}{2}c_{v,tr,s} + c_{v,rot,s}\right) \tag{3.30a}$$

$$k_{vl,s} = \mu_{l,s} c_{v,vib,s} \tag{3.30b}$$

where $c_{v,tr,s}$, $c_{v,rot,s}$, and $c_{v,vib,s}$ are the specific heat capacities at constant volume for the species s

evaluated under translational, rotational, and vibrational temperatures, respectively. The respective expressions for the $c_{v,tr,s}$, $c_{v,rot,s}$, and $c_{v,vib,s}$ are given in Eqs. (3.31), (3.32), and (3.33).

$$c_{v,tr,s} = \frac{3}{2}\frac{\hat{R}}{M_s} \tag{3.31}$$

$$c_{v,rot,s} = \begin{cases} \dfrac{\hat{R}}{M_s} \rightarrow for\left(N_2, O_2, NO, N_2^+, O_2^+, NO^+, C_2, CN, CO, C_3, H_2, C_2H\right) \\ 0 \rightarrow for\left(N, O, N^+, O^+, C, C^+, H, H^+, e^-\right) \end{cases} \tag{3.32}$$

$$c_{v,vib,s} = \begin{cases} \dfrac{\hat{R}}{M_s} \rightarrow for\left(N_2, O_2, NO, N_2^+, O_2^+, NO^+, C_2, CN, CO, C_3, H_2, C_2H\right) \\ 0 \rightarrow for\left(N, O, N^+, O^+, C, C^+, H, H^+, e^-\right) \end{cases} \tag{3.33}$$

The total viscosity and conductivity of the flow gas were calculated using the semi-empirical mixing formula suggested by Wilke [11], as follows:

$$\mu_l = \sum_s \frac{X_s \mu_{l,s}}{\phi_s} \tag{3.34a}$$

$$k_l = \sum_s \frac{X_s k_{l,s}}{\phi_s} \tag{3.34b}$$

$$k_{vl} = \sum_s \frac{X_s k_{vl,s}}{\phi_s} \tag{3.34c}$$

$$X_s = c_s \frac{M}{M_s}, M = \left(\sum_s \frac{c_s}{M_s}\right)^{-1} \tag{3.35}$$

$$\phi_s = \sum_{r \neq e^-} X_r \left[1 + \sqrt{\frac{\mu_{l,s}}{\mu_{l,r}}} \left(\frac{M_r}{M_s}\right)^{0.25}\right]^2 \left[\sqrt{8\left(1 + \frac{M_s}{M_r}\right)}\right]^{-1} \tag{3.36}$$

In this study, a constant diffusion coefficient was assumed for all the species of the flow gas. Using a constant Schmitt number of 0.5, the diffusion coefficient for each of the species was expressed by the formula given in Eq. (3.37) below.

$$d_{coef} = \frac{\mu}{0.5\rho} \tag{3.37}$$

Neglecting both the thermal and pressure diffusion effects, diffusion velocity of the components of the gas mixture can be taken to be directly proportional to the mass concentration. As a result, the diffusive fluxes could be respectively expressed in the x and y directions as:

$$\rho_s u_s = -\rho d_{coef} \frac{\partial c_s}{\partial x} \tag{3.38a}$$

$$\rho_s v_s = -\rho d_{coef} \frac{\partial c_s}{\partial y} \tag{3.38b}$$

3.3.3 Equation of State

The total energy equation was solved by summing up the individual energy components as given by the expression in Eq. (3.39).

$$E_t = \sum_s \rho_s c_{v,s} T + \sum_s \rho_s h_s^0 + \frac{1}{2} \sum_s \rho_s \left(u^2 + v^2\right) + E_v + E_e \tag{3.39}$$

Equation (3.39) can be solved to evaluate the value of the translational-rotational temperature T. The specific heat capacity for the species at a constant volume $c_{v,s}$ in Eq. (3.39) was given by the sum of the individual specific heats for both the translational and rotational temperatures as shown below.

$$c_{v,s} = c_{v,tr,s} + c_{v,rot,s} \tag{3.40}$$

The expressions for the $c_{v,tr,s}$ and $c_{v,rot,s}$ had been given earlier in Eqs. (3.31) and (3.32), respectively. The values of the species' enthalpy of formation h_s^0 in Eq. (3.39) above are defined in Table [3.1].

Vibrational energy for the species contained in a harmonic oscillator at the vibrational temperature T_v was evaluated by taking the sum of the individual species' vibrational energies as expressed in Eq. (3.41).

$$E_v = \sum_s \rho_s e_{v,s} \tag{3.41}$$

The vibrational energy values for the species were independently evaluated for the individual species as $e_{v,s}$ in the following expression:

$$e_{v,s} = \begin{cases} \dfrac{\hat{R}}{M_s}\dfrac{\theta_{v,s}}{(xa)^{r_s}-1} \\ \\ \dfrac{\hat{R}}{M_s}\dfrac{\theta_{v,s,1}+2\theta_{v,s,2}+\theta_{v,s,3}}{(xe)^{r_s}-1} \\ \\ \dfrac{\hat{R}}{M_s}\dfrac{\theta_{v,s,1}+2\theta_{v,s,2}+\theta_{v,s,3}}{(xd)^{r_s}-1} \end{cases} \tag{3.42}$$

Where the values of xa, xd and xe were defined using Eq. (3.43) below.

$$\begin{aligned} xa &= exp\left(\frac{226}{T_v}\right) \\ xd &= exp\left(\frac{920}{T_v}\right) \\ xe &= exp\left(\frac{46}{T_v}\right) \end{aligned} \tag{3.43}$$

The values of the characteristic vibrational temperature $\theta_{v,s,1\sim3}$ in Eq. (3.42) above are given in Table [3.3]. Each of the energy contained in the excited electronic state was assumed to be populated according to the Boltzmann distribution function and governed by the vibrational-electronic temperature T_{ve} in the two-temperature model used in this study. Considering electronic excitation up to the first state, the total electronic energy E_e can be calculated by adding up the individual species' electronic energies as expressed in Eq. (3.44). The electronic energy for each of the species was calculated using the expression in Eq. (3.45).

$$E_e = \sum_s \rho_s e_{el,s} \tag{3.44}$$

$$e_{el,s} = \begin{cases} \dfrac{\hat{R}}{M_s}\left[\dfrac{\theta_{el,s}(xb)^{r_s}}{(g_{0,s} + g_{1,s}(xb)^{r_s})}\right] \rightarrow for \begin{pmatrix} s = N, O, N^+, O^+ \\ r_s = 7,6,6,10 \end{pmatrix} \\[2ex] \dfrac{\hat{R}}{M_s}\left[\dfrac{\theta_{el,s,1}(xb)^{r_s}}{(g_{0,s} + g_{1,s}(xb)^{r_{s1}})} + \dfrac{\theta_{el,s,2}(xb)^{r_s}}{(g_{0,s} + g_{1,s}(xb)^{r_{s2}})}\right] \rightarrow for \begin{pmatrix} s = O_2 \\ r_{s1} = 3, r_{s2} = 5 \end{pmatrix} \\[2ex] \dfrac{\hat{R}}{M_s}\left[\dfrac{\theta_{el,s}(xbpp)^{r_s}}{(g_{0,s} + g_{1,s}(xbpp)^{r_s})}\right] \rightarrow for \begin{pmatrix} s = N_2^+ \\ r_s = 4 \end{pmatrix} \\[2ex] \dfrac{\hat{R}}{M_s}\left[\dfrac{\theta_{el,s}(xbp)^{r_s}}{(g_{0,s} + g_{1,s}(xbp)^{r_s})}\right] \rightarrow for \begin{pmatrix} s = C, C^+ \\ r_s = 4,17 \end{pmatrix} \end{cases} \tag{3.45}$$

Similarly, the values of xb, xbp and $xbpp$ in Eq. (3.45) above were evaluated using Eq. (3.46).

$$\begin{aligned} xb &= exp\left(\frac{-3785.5}{T_{ve}}\right) \\ xbp &= exp\left(\frac{-3590}{T_{ve}}\right) \\ xbpp &= exp\left(\frac{-3330}{T_{ve}}\right) \end{aligned} \tag{3.46}$$

In Eq. (3.45), $g_{0,s}$ and $g_{1,s}$ are the ground state and first excitation state degeneracies, respectively, while $\theta_{el,s}$ refers to the characteristic temperature of the first excitation state. The values of these constants are given in Table [3.4].

The gas static pressure p was calculated by summing up the partial pressures of all the species within the flow. This was done through the expression given in Eq. (3.47). On the other hand, the electron pressure p_e portion of Eq. (3.47) in the currently used two-temperature model was deduced using Eq. (3.48).

$$p = \sum_{s \neq e^-} \rho_s \frac{\hat{R}}{M_s} T + p_e \tag{3.47}$$

$$p_e = \rho_{e^-} \frac{\hat{R}}{M_{e^-}} T_v \tag{3.48}$$

The specific enthalpy h_s was calculated using the expression in Eq. (3.49) below.

$$h_s = c_{v,s} T + \frac{\hat{R}}{M_s} + h_s^0 + e_{v,s} + e_{el,s} \tag{3.49}$$

The vibrational and electronic energies' relation, given in Eq. (3.50), were utilized in solving for the vibrational temperature using the Newton iteration method.

$$E_v + E_e = f(\rho, \rho_s, T_{ve}) \tag{3.50}$$

3.3.4 Chemical Reaction Model

Table [3.5] presents a summary of the chemical reaction schemes used in this study. Similar reactions to the ones previously used by Suzuki in Ref. [4] were applied in this study. The reaction rate coefficients were determined using the two-temperature model developed by Park [12]. From the model, the forward and backward reaction rates were obtained through the expressions in Eqs. (3.51) and (3.52), respectively.

$$k_f\left(T_a\right) = C_f T_a^{\eta} exp\left(\frac{-\theta_{d,s}}{T_a}\right) \tag{3.51}$$

$$k_b\left(T_a\right) = \frac{k_f\left(T_a\right)}{K_{eq}\left(T_a\right)} \tag{3.52}$$

The constants C_f, η and $\theta_{d,s}$ above are defined in Table [3.5]. The values of the equilibrium constants K_{eq} were determined through the curve fits that matched the experimental data. This was done by expressing K_{eq} in the form given in Eq. (3.53).

$$K_{eq} = exp\left[A_1 Z + A_2 + A_3 \ln\left(\frac{1}{Z}\right) + \frac{A_4}{Z} + \frac{A_5}{Z^2}\right] \tag{3.53}$$

where Z in the above equation was defined as follows in Eq. (3.54).

$$Z = \frac{T_a}{10^4} \tag{3.54}$$

The values of the evaluation constants A_i used in Eq. (3.53) are given in Table [3.6].

Park [13] developed a two-temperature kinetic model to assess the dissociation reaction rate coefficients. The same model was also applied in the present research study. In this model, an assumption is made that both the forward and backward dissociation reaction rate coefficients for two-body collisions are a function of the geometric-average of translational and vibrational temperatures, as expressed in Eq. (3.55). For the case where involved colliding particles are electrons, the forward reaction rate coefficients are defined as a function of the vibrational temperature only. This is expressed in Eq. (3.56) below.

$$\begin{aligned} k_f &= k_f(T_a) \\ T_a &= (TT_{ve})^{0.5} \end{aligned} \tag{3.55}$$

$$\begin{aligned} k_f &= k_f(T_a) \\ T_a &= T_{ve} \end{aligned} \tag{3.56}$$

The backward reaction rate coefficients, on the other hand, solely depend on the colliding particles' translational temperatures and expressed as follows.

$$\begin{aligned} k_b &= k_b(T_a) \\ T_a &= T \end{aligned} \tag{3.57}$$

For the electron impact ionization reaction, the coefficients for the reaction rates depend on the vibrational temperature only as expressed in Eq. (3.58). The reaction rate coefficients for the remaining cases of neutral exchange, associate ionization, as well as the charge exchange reactions are all stated purely as a function of the translational temperature as shown in Eq. (3.59).

$$\begin{aligned} k_f &= k_f\left(T_a\right) \\ k_b &= k_b\left(T_a\right) \\ T_a &= T_{ve} \end{aligned} \tag{3.58}$$

$$\begin{aligned} k_f &= k_f\left(T_a\right) \\ k_b &= k_b\left(T_a\right) \\ T_a &= T \end{aligned} \tag{3.59}$$

Since we used similar reaction schemes as the ones used by Suzuki in Ref. [4], the chemical reactions were basically identical. The dissociation reactions shown in Table [3.5] were expressed in Eq. (3.60), in order of their reaction rates. The remaining chemical reactions were expressed in a general form as shown in Eq. (3.61a), with their general equivalent reaction rates given in Eq. (3.61b).

$$\begin{aligned} R_1 &= \sum_s \left[k_f \frac{\rho_{N_2}}{M_{N_2}} \frac{\rho_s}{M_s} - k_b \frac{\rho_N}{M_N} \frac{\rho_N}{M_N} \frac{\rho_s}{M_s} \right] \\ R_2 &= \sum_s \left[k_f \frac{\rho_{O_2}}{M_{O_2}} \frac{\rho_s}{M_s} - k_b \frac{\rho_O}{M_O} \frac{\rho_O}{M_O} \frac{\rho_s}{M_s} \right] \\ R_3 &= \sum_s \left[k_f \frac{\rho_{NO}}{M_{NO}} \frac{\rho_s}{M_s} - k_b \frac{\rho_N}{M_N} \frac{\rho_O}{M_O} \frac{\rho_s}{M_s} \right] \\ R_4 &= \sum_s \left[k_f \frac{\rho_{C_2}}{M_{C_2}} \frac{\rho_s}{M_s} - k_b \frac{\rho_C}{M_C} \frac{\rho_C}{M_C} \frac{\rho_s}{M_s} \right] \\ R_5 &= \sum_s \left[k_f \frac{\rho_{CN}}{M_{CN}} \frac{\rho_s}{M_s} - k_b \frac{\rho_C}{M_C} \frac{\rho_N}{M_N} \frac{\rho_s}{M_s} \right] \\ R_6 &= \sum_s \left[k_f \frac{\rho_{H_2}}{M_{H_2}} \frac{\rho_s}{M_s} - k_b \frac{\rho_H}{M_H} \frac{\rho_H}{M_H} \frac{\rho_s}{M_s} \right] \end{aligned} \tag{3.60}$$

$$A + B \rightleftharpoons C + D \tag{3.61a}$$

$$R_i = k_f \frac{\rho_A}{M_A}\frac{\rho_B}{M_B} - k_b \frac{\rho_C}{M_C}\frac{\rho_D}{M_D} \tag{3.61b}$$

$$i = \left(7 \sim 36\right)$$

The chemical reaction rates in Eq. (3.60) and (3.61) above were used to express the species chemical source terms W_s in Eq. (3.62). Even though $W_{N_2}, W_{O_2}, W_{C_2}$ and W_{H_2} were also expressed in this equation, they had been carefully eliminated in the governing equation that was given earlier in Eq. (3.24) and their respective elemental densities introduced instead.

$$\begin{aligned}
W_N &= M_N \begin{pmatrix} 2R_1 + R_3 + R_5 + R_7 + R_8 - R_{11} + R_{12} + R_{14} - R_{16} \\ -R_{19} - 2R_{21} + R_{23} - R_{24} - R_{28} + R_{30} - R_{32} - R_{33} \end{pmatrix} \\
W_O &= M_O \begin{pmatrix} 2R_2 + R_3 - R_7 - R_8 + R_9 - R_{10} + R_{11} - R_{13} + R_{15} \\ -R_{19} - 2R_{20} - R_{22} - R_{27} - R_{30} + R_{31} + R_{32} - R_{34} \end{pmatrix} \\
W_{N_2} &= M_{N_2}\left(-R_1 - R_8 - R_{12} - R_{23} - R_{26} + R_{28} - R_{31}\right) \\
W_{O_2} &= M_{O_2}\left(-R_2 + R_7 + R_{10} + R_{22} + R_{24} + R_{25} + R_{27} - R_{29}\right) \\
W_{NO} &= M_{NO}\left(-R_3 - R_7 + R_8 + R_{13} - R_{25} + R_{29}\right) \\
W_{N^+} &= M_{N^+}\left(R_{22} - R_{23} + R_{24} + R_{25} + R_{33}\right) \\
W_{O^+} &= M_{O^+}\left(-R_{25} + R_{27} + R_{28} - R_{31} + R_{34}\right) \\
W_{N_2^+} &= M_{N_2^+}\left(R_{21} + R_{23} + R_{26} + R_{31} + R_{32}\right) \\
W_{O_2^+} &= M_{O_2^+}\left(R_{20} - R_{24} - R_{26} - R_{27} + R_{29} + R_{30}\right) \\
W_{NO^+} &= M_{NO^+}\left(R_{19} - R_{22} - R_{28} - R_{29} - R_{30} - R_{32}\right) \\
W_C &= M_C\left(2R_4 + R_5 - R_9 + R_{10} - R_{12} + R_{13} - R_{14} - R_{17} - R_{35}\right) \\
W_{C_2} &= M_{C_2}\left(-R_4 + R_9 + R_{14} - R_{15} + R_{16} + R_{17} + R_{18}\right) \\
W_{CN} &= M_{CN}\left(-R_5 + R_{11} + R_{12} - R_{13} - R_{14} + R_{16}\right) \\
W_{CO} &= M_{CO}\left(-R_9 - R_{10} - R_{11} - R_{15}\right) \\
W_{C_3} &= M_{C_3}\left(R_{15} - R_{16} - R_{17}\right) \\
W_H &= M_H\left(2R_6 - R_{18} - R_{36}\right) \\
W_{H_2} &= M_{H_2}\left(-R_6 + R_{18}\right) \\
W_{C_2H} &= M_{C_2H}\left(-R_{18}\right) \\
W_{H^+} &= M_{H^+}\left(R_{36}\right)
\end{aligned} \tag{3.62}$$

3.3.5 Exchange of Energy between the Various Energy Modes

The vibrational source term that was introduced in Eq. (3.26) was solved by the expression given in Eq. (3.63).

$$W_v = Q_{t-v} + Q_{d-v} + Q_{t-e} + Q_{e-e} + Q_{e-ex} \tag{3.63}$$

The terms on the right-hand side of Eq. (3.63) were defined as; the translational-vibrational energy transfer rate, the vibrational energy transfer rate through dissociation, the translational-electron energy transfer rate, the electron-electronic energy transfer rate, and the energy transfer rate in electronic excitation, respectively. The rate of energy exchange between the translational and the vibrational energy modes was given by Park's modification of the Landau-Teller equation in Ref [4] as,

$$Q_{t-v} = \sum_{s=mole} Q_{t-v,s} \tag{3.64}$$

where $Q_{t-v,s}$ was expressed as follows:

$$\begin{gathered} Q_{t-v,s} = \rho_s \frac{e^{*}_{v,s}(T) - e_{v,s}}{\tau_{s_{LT}} + \tau_{c,s}} \left| \frac{T_{shock} - T_v}{T_{shock} - T_{v,shock}} \right|^{S-1}, \\ S = 3.5exp\left(\frac{-5000}{T_{shock}} \right) \end{gathered} \tag{3.65}$$

From Eq. (3.65), the average Landau-Teller relaxation time $\tau_{s_{LT}}$ could be solved using the expression given in Eq. (3.66).

$$\tau_{s_{LT}} = \frac{\sum X_r}{\sum \frac{X_r}{\tau_{sr_{LT}}}} \tag{3.66}$$

where,

$$\tau_{sr_{LT}} = \frac{1}{p} exp\left(AT^{-1/3} - B \right) \tag{3.67}$$

The value of the pressure p required for the evaluation of $\tau_{sr_{LT}}$ was given in atm. The constants A and B were taken from the works of Park and his co-researchers in Ref [12] and [14], and their respective values defined in Table [3.7]. The collision limited relaxation time $\tau_{c,s}$ in Eq. (3.65) was evaluated using Eq. (3.68).

$$\tau_{c,s} = \frac{1}{c_s \tau_{sr} n_s} \tag{3.68}$$

The values of the average molecular speed c_s of the species s and the limiting collision cross-section τ_{sr} were calculated using Eq. (3.69).

$$c_s = \sqrt{\frac{8\hat{R}T}{\pi M_s}}, \qquad \tau_{sr} = 10^{-20} \left(\frac{50000}{T} \right)^2 \tag{3.69}$$

The rate of vibrational energy transfer through dissociation was calculated by solving Eq. (3.70). The vibrational energy equation is able to account for the preferential removal or disposal of the highly excited vibrational states in dissociation or recombination through the preferential dissociation model.

$$Q_{d-v} = \sum_{s=mole} Q_{d-v,s}, \qquad Q_{d-v,s} = e_{v,s} W_s \tag{3.70}$$

The elastic energy transfer between electrons and the heavy particles was evaluated through the translational-electron energy transfer rate. Basically, when there is a difference in the temperature values between T and T_{ve}, the elastic collision between the electrons and the heavy particles tends to equilibrate the two temperatures. The rate of the equilibration process can be solved as shown in Eq. (3.71).

$$Q_{t-e} = 3\rho_{e^-} R\left(T - T_{ve}\right)\sqrt{\frac{8\hat{R}T}{\pi M_s}}\sum_s \frac{\rho_s}{M_s^2}\sigma_s \tag{3.71}$$

where σ_s is defined as the cross-section of the energy transfer between the electrons and the heavy particles of species s .

The other energy exchange mechanism considered in the current study is the electron-electronic energy transfer rate. Since the electronic excitation, ionization, and ionic recombination of both the atomic and molecular species frequently occur as a result of collisions with the electrons, the energies involved in exchange rates are either extracted from or discharged into the electron gas. The energy transfer rate in this case can be calculated using the expression given in Eq. (3.72).

$$\begin{aligned} Q_{e-e} &= \sum_{s=N^+,O^+,C^+,H^+} Q_{e-e,s}, \\ Q_{e-e,s} &= -E_\infty W_s \end{aligned} \tag{3.72}$$

The values of the ionization potential E_∞ in the above expression are defined in Table [3.8].

The final energy exchange case that was considered in this study was the energy transfer rate in electronic excitation. This was evaluated using Eq. (3.73) as follows.

$$\begin{aligned} Q_{e-ex} &= \sum_s Q_{e-ex,s}, \\ Q_{e-ex,s} &= e_{el,s} W_s \end{aligned} \tag{3.73}$$

3.3.6 Numerical Approach

The flow field governing equations that were introduced earlier in Eq. (3.24) were integrated using the cell-centered finite volume method. The convective numerical flux terms were evaluated by applying the Advection Upstream Splitting Method, combining flux difference splitting and flux vector splitting methods, (AUSM-DV) upwind scheme introduced by Wada and Liou [15]. To improve the spatial accuracy to higher orders, a Monotonic Upwind Scheme for Conservation Laws (MUSCL) scheme was applied. The central differencing scheme was used for the calculation of the viscous flux terms. In order to achieve an enhanced convergence of the solution, time integration was calculated using the Lower-Upper Symmetric Gauss Seidel (LU-SGS) algorithm. This algorithm was combined with a diagonal point implicit method by Eberhardt and Imlay [16] in order to maintain the stability of the reaction terms.

3.4 Physical and Numerical Models for Material Thermal Response

3.4.1 Governing Equations

Thermal response analysis of each test specimen was done by solving two-dimensional axisymmetric gas mass, momentum and energy conservation equations alongside solid material's energy conservation equation. The gas convective energy and solid material's energy conservation equations were decoupled and independently solved within the same numerical model. The governing equations were then expressed as follows.

$$\frac{\partial \rho \varepsilon}{\partial t}+\frac{\partial(\rho u)\varepsilon}{\partial x}+\frac{1}{r}\frac{\partial(\rho v)r\varepsilon}{\partial r}=0 \tag{3.74}$$

$$\frac{\partial(\rho u)\varepsilon}{\partial t}+\frac{\partial\left(\rho u^2+p\right)\varepsilon}{\partial x}+\frac{1}{r}\frac{\partial(\rho u v)r\varepsilon}{\partial r}=-\varepsilon f_x \tag{3.75}$$

$$\frac{\partial(\rho v)\varepsilon}{\partial t}+\frac{\partial(\rho u v)\varepsilon}{\partial x}+\frac{1}{r}\frac{\partial\left(\rho v^2+p\right)r\varepsilon}{\partial r}=-\varepsilon f_r \tag{3.76}$$

$$\frac{\partial e_{gas}\varepsilon}{\partial t}+\frac{\partial\left(e_{gas}+p\right)u\varepsilon}{\partial x}+\frac{1}{r}\frac{\partial\left(e_{gas}+p\right)vr\varepsilon}{\partial r}=\frac{\partial}{\partial x}\left(k_{gas}\frac{\partial T_{gas}}{\partial x}\right)+\frac{1}{r}\frac{\partial}{\partial r}\left(rk_{gas}\frac{\partial T_{gas}}{\partial r}\right)+\alpha\left(T_{sol}-T_{gas}\right) \tag{3.77}$$

$$\frac{\partial e_{sol}}{\partial t}=\frac{\partial}{\partial x}\left(k_{eff}\frac{\partial T_{sol}}{\partial x}\right)+\frac{1}{r}\frac{\partial}{\partial r}\left(rk_{eff}\frac{\partial T_{sol}}{\partial r}\right)-\alpha\left(T_{sol}-T_{gas}\right) \tag{3.78}$$

where ρ is gas density in kg/m^3, ε is porosity, u and v are the respective axial and radial velocity components in m/s, p is pressure in Pa, x and r are axisymmetric coordinates in m, t is time in s, f_x and f_r are axial and radial gas friction force per unit volume in N/m^3, respectively, e_{sol} and e_{gas} are the respective solid material and gas energy per unit volume in J/m^3, T_{sol} and T_{gas} are solid material and gas temperatures in K, k_{gas} is the gas conductivity in W/(m-K), k_{eff} is the effective conductivity in w/(m-K), and α is the coefficient of heat transfer in W/(m^3-K). The right-hand side of the gas momentum conservation expressions in Eqs. (3.75) and (3.76) denoted the gas friction force whereas the last terms in Eqs. (3.77) and (3.78) for the gas energy and solid material energy conservation equations, respectively, represented the relaxation term. This term was purposely included in the governing equations in order to equilibrate the gas and solid material temperatures. Gas friction force was evaluated by the expression given in Eq. (3.79).

$$\begin{aligned} f_x &= \frac{\mu}{\gamma}u, \\ f_r &= \frac{\mu}{\gamma}v \end{aligned} \tag{3.79}$$

where γ is permeability in m^2, and μ is viscosity in (N-s)/m^2.

The governing equations for the gas were numerically integrated using an implicit method while the solid material energy conservation equation was solved using an explicit method. The governing equations for the gas were discretized using the cell-centered finite volume scheme and the numerical flux functions evaluated using the AUSM-DV method. To achieve a higher order accuracy in space for the gas governing equations, a MUSCL interpolation scheme was similarly employed as was done in Ref. [1]. For the solid material, the governing equation was similarly discretized using the cell-centered finite volume scheme and its viscous flux function evaluated using a 2nd order central differencing scheme.

3.4.2 Physical Modeling of Radiative Conductivity

The value of the radiative conductivity was determined statistically through a ray tracing calculation approach. This was done using a set of digital models for the internal structures of each study material. Even though this procedure was initially developed for studying the 0.12 g/cm^3 material [17], it was similarly applied in this study to analyze the other two test materials with higher densities. The evaluation procedure for the radiative conductivity involved the development of: (1) the three-dimensional (3D) X-ray computed tomography (CT) models for the internal structures of the test materials and, (2) the model for evaluating the radiation extinction coefficient. These models are described below.

3.4.2.1 Three-dimensional X-ray CT Models for the Specimens' Internal Structures

The data for the tomogram and binarized images of the study materials were obtained using a micro-focus X-ray CT system (FLEX-M345, Beam sense) at the National Institute of Advanced

Industrial Science and Technology (AIST) Chubu, Japan. The current and voltage of the X-ray tube were set at 100 μA and 60 V, respectively. The bulk materials analyzed were rectangular parallelepiped in shape, with dimensions of 3 mm x 3 mm x 10 mm. The samples were manually cut from the bulk material. The tomogram and binarized images are illustrated in Fig. 3.4(a) and (b), respectively. The spatial resolutions for the images were about 2.12 μm for both 0.12 and 0.15 g/cm^3 materials, and 2.22 μm for 0.27 g/cm^3 material. 3D digital models were then developed using the binarized images, for purposes of conducting ray tracing calculations to evaluate the radiative extinction coefficients for the test specimens. The threshold binarization criterion was determined to ensure that the effective porosity values for the 3D digital models were similar to the corresponding values of the study materials. The effective porosity values for the materials were about 93%, 90%, and 85% for 0.12, 0.15 and 0.27 g/cm^3 materials, respectively. The effective porosity value for the 0.27 g/cm^3 material was calculated by assuming that the char residue generated from pyrolysis of the resin was an amorphous carbon. Therefore, the density of the char residue was set to 2 g/cm^3, which is the nominal density of an amorphous carbon. The developed digital models were represented by cubic elementary volumes of sides 1.69 mm for both 0.12 and 0.15 g/cm^3 test materials, and 1.33 mm for the 0.27 g/cm^3 test material. A sample of the elementary volume for 0.12, and 0.15 g/cm^3 test materials is shown in Fig. 3.5.

The resolution of the CT data obtained was believed to be sufficient enough for the study of the internal structure of the 0.27 g/cm^3 test material. It should be clear at this point, that the 0.27 g/cm^3 test material (char) in this study was developed from the 0.15 g/cm^3 test material through the procedure explained in section 2.2.2 of Chapter 2. A Standard Triangulated Language (STL) model was also used to visualize the internal structures of 0.15 and 0.27 g/cm^3 test materials and their results compared in Fig. 3.6. From Fig. 3.6(a), carbon fibers which are the main constituent of the carbon material are well visible. The STL model was also able to show the difference in Fig. 3.6(b), clearly indicating the presence of the char residue. This observation confirmed the validity of our binarization procedures for the evaluation of the radiative extinction coefficients of the two materials. However, the ray tracing calculations were done using the 3D voxel models due to the high computational constraints of the STL models.

3.4.2.2 Modeling of Radiative Extinction Coefficients

The optical extinction coefficients for the materials were statistically evaluated using the set of the calculated ray tracing data. This was done by following the method by Petrasch *et. al*. to analyze porous ceramic material [18]. In this method, an extinction coefficient is calculated by assuming that the material is both homogeneous and semi-transparent, and that light attenuation in the material follows Beer-Lambert law. Under these assumptions, an initial light of intensity I_o is reduced after propagating along a given ray path of distance s_p. The ratio of the intensity at s_p, $I(s_p)$ to the initial intensity is expressed as follows in Eq. (3.84).

$$\frac{I\left(s_p\right)}{I_o} = exp\left(-\beta s_p\right) \tag{3.80}$$

where β is the extinction coefficient in m^{-1}. The left-hand side of Eq. (3.80) is independently interpreted, using the geometrical optics concept, as the ratio of the extant rays after propagating the path length s_p to the initially emitted rays from the source.

The following ray tracing procedure was conducted using the 3D digital model to statistically evaluate the left-hand side of Eq. (3.80). First, the rays were emitted from an origin every 15° in all global directions within the model. The origin of the rays was randomly specified for 50000 different positions. Next, the ratio of the extinct rays at the path length s_p to the total number of rays was calculated as a function of the path length. It should be noted that reflection of the rays at the solid surface was not accounted for in this study. This, therefore, implies that the electromagnetic energy emitted was fully absorbed at the solid carbon surfaces. The above calculated ratio was interpreted as the probability density function for the extinct rays along the path length. The probability of a ray being extinct at a path length less than s_p was calculated using the cumulative distribution function $G\left(s_p\right)$, through integration of the probability density function of the path length obtained by ray tracing data. Finally, the probability of a ray being extant through the path length s_p was given by the term $1-\int_0^{s_p} G\left(s_p\right) ds_p$ in the expression below.

$$\frac{I\left(s_p\right)}{I_o} = 1-\int_0^{s_p} G\left(s_p\right) ds_p = exp\left(-\beta s_p\right) \tag{3.81}$$

The ray tracing simulation calculation results for the right-hand side of Eq. (3.81) were plotted as shown in Fig. 3.7, and labeled as “Extinction ratio”. In this study, five different 3D digital model results were presented for each test material and in each case, curves were fitted to determine the value of the extinction coefficient β as 4692 ± 882, 6656 ± 666 and 13610 ± 1182 m^{-1} for 0.12, 0.15 and 0.27 g/cm^3 test materials, respectively.

In order to verify the validity of our porous carbon material model, the calculated extinction coefficient results were compared with the data reported by Petrasch and his co-researchers and found to agree fairly well. This agreement was used as a confirmation for the satisfactory accuracy of our model.

The effect of scattering on the extinction coefficient was ignored in our study, as was similarly done previously in the study in Ref. [17]. In that study, the effect of scattering was examined for the case of 0.12 g/cm^3 test material by following a previously applied approach [19]. From the study, just a slight difference between the extinction coefficient values with and without scattering was noted. The small difference implied that the material under study was relatively isotropic in nature. Thus, this approximation was applied for the other two test materials in this study.

3.4.3 Thermophysical Properties

Since the heating tests in this study were carried out in a nitrogen arcjet freestream, thermochemical equilibrium flow for the nitrogen gas was assumed within the porous matrices of the test materials. Therefore, the gas equilibrium properties and transport properties, including the gas conductivity were calculated following a previously utilized approach given in Ref. [1]. Again, the radiative transfer within the materials was calculated using diffusion approximation, as expressed in Eq. (3.82). This approximation was assumed to be valid for our study due to the large optical depth obtained based on the evaluated extinction coefficients and the depths of material specimens. The effective thermal conductivity k_{eff} in Eq. (3.78) was deduced by summing up the apparent solid material thermal conductivity k_{sol} and the radiative conductivity k_{rad} as shown in Eq. (3.83).

$$k_{rad} = \frac{16\sigma_{SB}T^3}{3\beta} \tag{3.82}$$

$$k_{eff} = k_{sol} + k_{rad} \tag{3.83}$$

The effective thermal conductivity in Eq. (3.83) assumed a local thermal equilibrium between the gaseous and the solid phases. Therefore, our numerical approach ignored the thermal nonequilibrium state in which each of the energy transfer modes is normally analyzed separately as described by Kaviany [20]. Further simplification for this effective thermal conductivity suggests that the gas that fills the pores of the test materials does not participate in the radiative transfer, and as a result, the coupling effect between the flow motion and radiation was ignored in this case.

Figure 3.8 illustrates variation of the effective, apparent solid and radiative conductivities with temperature. Currently, temperature dependence on solid thermal conductivity, particularly at elevated heating temperatures, is unknown. As a result, the value of solid thermal conductivity was evaluated by the following approach given in Ref. [17]. A linear function extrapolated from the measurement of the rigid carbon insulation material was used to calculate the values of k_{sol} up to 1000 K temperature range. Based on an independent analysis of the manufacturer's specification data for the effective thermal conductivity of the carbon-based material, this was a likely reasonable treatment. Between 1000 and 3000 K temperature range, a constant solid thermal conductivity was set, guided by the following analysis. The radiative conductivity calculated from our study was subtracted from the thermal conductivity data availed by the manufacturer to get a relatively constant difference of about 0.23 W/(m-K). This difference was interpreted as the solid thermal conductivity. From Figs. 3.18, it can be seen that radiative transfer within the test materials effectively dominated the energy transfer modes after about 1500 K.

The temperature-dependent specific heat capacities for all the test materials were calculated by following Potts formula [21] as given in Eq. (3.84),

$$C_p = \frac{c_2 T}{\sqrt{T^2 + c_1^2}} \ , \tag{3.84}$$

where $c_1 = 800$ K, and $c_2 = 2300$ J/(kg-K).

3.4.4 Computational Meshes and Boundary Conditions

Different computational meshes were used for the various calculations in this study. Computations were made to validate the ARCFLO3+ code set used for the analysis of the flow variables within the arc heater, the nozzle, and the test chamber sections. Calculations were also done to analyze the thermal response of the test materials. Since two sets of calculations were conducted for thermal response analysis, two separate boundary conditions were set to suit the individual needs of each calculation. The boundary conditions for each of the calculations above are explained as follows:

The computational mesh shown in Fig. 3.9 was used to analyze the flow fields for the arc heater, and the nozzle sections as labelled in the same Figure. For the arc heater section, a computational mesh with a total of 180×40 grid points was used. The radial temperature distribution at a given constant pressure was set as the initial condition. The constrictor wall was treated as permeable so as to numerically simulate the radial inward injection of the test gas. The remaining walls were treated as non-slip with a constant wall temperature condition imposed. The end boundary at the downstream was slightly extended away from the nozzle throat to impose a supersonic outflow condition. A blackbody with a given wall temperature was also imposed for the calculation of radiative transfer. The black body was used due to its ability to absorb all the radiation that falls on its surface. The nozzle section was analyzed using a computational mesh with 200×50 grid points. Flow distribution at the nozzle throat, calculated from the arc heater section, was imposed as the inflow boundary condition at the upstream end of the nozzle. An isothermal and non-slip wall conditions were also imposed.

For the test chamber section, the mesh configuration shown in Fig. 3.10 was used. Calculations for the first set of experiments were done using the computational mesh with a total of 130×111 grid points. An inflow condition from the computed steady state solution within the nozzle section was imposed at the nozzle exit region (indicated in Fig. 3.10). The wall boundaries were treated as non-slip, non-catalytic, and with an isothermal condition of 500 K. At the blunt body wall, both the fully- and non-catalytic conditions were imposed at the isothermal wall condition. Along the outflow boundary, zero order extrapolation was imposed. For the second set of experiments, calculations for the test chamber flow field were done using a similar grid structure to the one shown in Fig. 3.10. The total number of grid points in this case was 105×70. The boundary conditions were imposed in a similar manner as was done in the first case above. In both the test cases, an artificial viscous wall (shown in Fig. 3.10), that was arbitrarily fixed, was used to represent the test chamber wall. Although this wall was approximately fixed, its influence at the core of the arcjet flow analysis near the flat faced blunt probe was negligible as demonstrated previously [22].

The computational meshes for solving the solid material energy conservation equation using the coupling method is given in Fig. 3.11. A multi-block grid structure was used to analyze the thermal response of the test specimens. The boundary conditions were set on various surfaces, as shown in the same figure, so as to appropriately simulate the arcjet heating and cooling conditions. The net wall heat flux q_{net} time history along the heating surface was determined from the CFD flow calculation as expressed in Eq. (3.85). Distribution results for the q_{net} are plotted in the next Chapter for the Results.

$$q_{net} = q_{CFD} - \varepsilon\sigma_{SB}\left(T_w^4 - T_\infty^4\right) \tag{3.85}$$

The value of q_{CFD} in Eq. (3.85) was composed of both the convective and diffusion terms, which were evaluated by following the approach given by Suzuki *et.* a*l*. in Ref. [5]. At the contact surfaces of the test specimen and the Bakelite holder, an adiabatic state was assumed. Bakelite is a plastic made from synthetic components, which was used in this study due to its excellent heat resistance properties at high heating temperatures. Effect of the gap between the test specimen and the Bakelite holder was accounted for by imposing a radiative cooling condition therein, and an incoming radiation temperature T_∞ was set at 400 K to replicate the in-depth measurements at the end of the test. Boundary for the rear surface was set in order to replicate the measured data.

For the thermal response analysis using an uncoupled approach, the boundary conditions were defined separately for the test specimen and the CFD flow. The computational grid system for this particular calculation is shown in Fig. 3.12. The main difference between Fig. 3.11 and Fig. 3.12 is the fact that in Fig. 3.11, both the flow and material response meshes were combined for purposes of coupling calculation. Figure 3.12 only shows material response mesh since it was solely used for uncoupled calculations. A single-block grid structure was used in the case of Fig. 3.12. The boundary conditions (b.c.) were set to appropriately simulate the arcjet heating and cooling conditions as explained below.

Material boundary conditions: during heating, time histories of the wall heat flux along the heating surface were calculated from a normalized heat flux distribution that was numerically simulated from the arcjet wind tunnel flows using an integrated numerical method by Sakai and his colleagues in Ref. [6]. This heat flux distribution was then appropriately set to replicate the experimentally measured time history of the surface temperature at the stagnation point as shown in Fig. 3.13. The measured and the calculated time histories of the surface temperature, both with radiation (in continuous graphs) and without radiation (dotted graphs), were compared. At this point, it was observed that the radiative conductivity had no discernible effect on the calculated surface temperature distribution. The quasi-steady state surface temperature for the $0.12, \text{and} \, 0.15$ g/cm^3 materials was approximated at 2800 K while that for the 0.27 g/cm^3 material was approximately 2700 K.

After heating, a radiative cooling boundary was imposed at the heating surface. The test specimens were similarly firmly held using the Bakelite tubes at the surfaces indicated by the blue lines in Fig. 3.12, with adiabatic conditions set therein. At the side surface, radiative cooling was employed while the boundary at the rear surface was set to replicate the measured temperature data. Radiative cooling was extended to the side surface adjacent to the rear surface. In this case, the incoming radiation temperature was set at 300 K.

Flow boundary conditions: The measured Pitot pressure value during experiments was imposed along the heating surface during heating. After heating, the gas density and internal energy were fixed using zero order extrapolation. At the rear surface, the internal energy was evaluated through zero order extrapolation while the initial gas density was retained to enhance flow out of the test specimen. Solid wall condition was imposed along the surfaces which made contact with the Bakelite holder (surfaces indicated by the blue lines in Fig.3.12). Zero order extrapolation was imposed for flow velocities and the pressure along the rest of the surfaces (indicated by the green lines in Fig. 3.12), effectively implying that these surfaces were permeable to the gas flow. Along the indicated side surface in the same figure, zero order extrapolations were also used for both the gas density and internal energy.

3.4.5 Coupling Method

An explicit coupling approach that is similar to the one used by Chen *et. al*. [23] was applied in calculating the unsteady interaction processes between the arcjet flow and the test specimen. It should be remembered that this method was only applied in the analysis of the thermal response using only the solid material energy conservation equation expressed in Eq. (3.78). The energy equation was numerically integrated with time-dependent boundary conditions. Therefore, heat flux values along the heating surface should be known at every time step. This can be done through updating of the boundary conditions after every time step using nonequilibrium flow calculation. However, this procedure is prohibitively time consuming and as such, an iteration process was employed at several time-points to obtain the heat flux values. Integration of the energy equation was then done by interpolating the boundary conditions at a given time using the time values between the known discrete time-points. In this study, the time-points were determined through trial and error, with the aim of achieving a smooth connection between the adjacent time-points. Calculation time-points of 32, 42, and 62 were selected for the $0.12, 0.15 \text{ and } 0.27$ g/cm^3 materials, respectively. The selections of the time-points were roughly guided by the individual heating times for the test specimens, and then broken down as follows. In the 0.12 g/cm^3 material: for the first 0.5s $t = 0.01, 0.03, 0.05, 0.1, 0.15, 0.2, 0.3, 0.4$ and 0.5s. Between 0.5 and 2.0s, a constant value of 0.25s was set. Thereafter, 0.5s constant interval was used up to 10 sec when heating ended. For the 0.15 and 0.27 g/cm^3 materials, a similar trend in the time-point selection was followed up to the end of their respective heating times of 15 and 25s. These time-points were chosen in order to achieve smooth connection between adjacent time-points and also to prevent the code set from blowing up.

The detailed process of coupling, illustrated in Fig. 3.14, is given as follows: the shock layer flow field was first calculated at a chosen time-point n and a known wall temperature T_w^n to determine the wall heat flux distribution at the time. This is indicated by process (1) in the figure. Thereafter, the material energy equation was integrated up to the next time-point $n+1$ by tentatively imposing the heat flux values determined at time-point n as the boundary condition in order to evaluate the wall temperature T_w^{n+1}, as illustrated by process (2) in the figure. The shock layer flow field calculations were then repeated using the T_w^{n+1} values to determine the wall heat flux distribution at time-point $n+1$. This presented by process (3) in the figure. Finally, the thermal response of the test specimen was integrated in time by interpolating the wall heat flux distribution at the intermediate time steps between the known adjacent time-point values as represented by process (4) in the same figure. This process was done throughout the heating time for the test materials.

During the coupling calculation, the heated surface of the test specimen receded as a result of the chemical reactions at the surface. A new specimen surface line was hence calculated based on the amount of receded distance at a given time step. Consequently, numerical mesh systems, both for the CFD flow and the test specimen response calculations, were redrawn at each time step until the end of heating. The rate of mass loss r_{ml} along the heating surface is evaluated from the CFD calculations using the following expression in Eq. (3.86).

$$r_{ml} = \frac{\left(M_C / M_{CN}\right) J_{CN} + \left(M_C / M_{C_3}\right) J_{C_3}}{\rho} \tag{3.86}$$

The total amount of surface recession sr in the normal direction is given by integrating r_{ml} with time during calculation. This is expressed in Eq. (3.87).

$$sr = \int r_{ml} dt \tag{3.87}$$

3.4.6 Grid Convergence Study

Both the CFD flow field, and the test specimen response solutions' independence on the calculation mesh structures were analyzed through the convergence study for both the arc heater and the test chamber flow, as well as for the test specimen's response calculation grid systems. Grid convergence was analyzed through comparison of the results obtained from the various mesh systems with grid points as summarized in Table 3.9. In this section, the grid convergence results are separately examined for the CFD flow field and the test specimen response meshes as follows.

The arc heater flow field grid convergence was analyzed by comparing the results obtained from the calculations of the mass flow rate of the arcjet freestream, the mass averaged enthalpy, and the heater wall pressure. Calculations were conducted for the Base grid and the Fine grid (generated by doubling the number of the Base grid points in the radial direction) and the maximum variation in the results of the above variables was found to be about 1%, as summarized in Table 3.10. Grid refinement in the axial direction actually posted a much reduced difference compared to the radial direction. This suggested that grid refinement would only add a negligible value to the computed results at inflated computational resources. Consequently, the decision to carry out the final calculations using the Base grid structure was reached.

The test chamber flow grid convergence study was done separately for two calculation cases: first, for the flow over the flat faced blunt probe of diameter 25 mm, and then for flow analysis over the 50 mm diameter test specimen during the coupling calculation. In the first case, a total of 130×111 grid points were used in the i and j directions, respectively, and the solution convergence was studied by refining the grid size near the heating wall surface. This is the region within which the shock wave is estimated to appear. Since much importance should be focused around the shock wave region, this region was deemed appropriate for the convergence study. In this study, wall refinement values of 1 and 3 μm were used to calculate and compare the results for the stagnation point Pitot pressure and the average heat flux values for the test specimen axially placed 50 mm away from the physical nozzle exit. Comparison results shown in Table 3.11 depicted a deviation of about 0.1% for the pressure distribution and about 0.6% for the heat flux distribution. Therefore, we believe that this convergence study was satisfactory.

The flow field grid for coupling calculation was analyzed for convergence by examining the effect of the number of grid points normal to the wall surface on the heat flux distribution along the heating surface. In this case, three meshes were analyzed (see Table 3.9). The observed heat flux difference along the surface was about 10% between the Coarse and the Base grids and within 2% between the Base and the Fine grids as indicated in Table 3.12. This trend indicated a satisfactory grid converged solution state with the Base grid. It should be noted that 105 grid points were determined along the specimen surface within the flow field grid, based on an independent uncoupled calculation results. The computed solution was relatively unaffected by altering the number of grid points along the surface, i.e. by using 75, 105, and 145 grid points for the Coarse, the Base, and the Fine grids, respectively.

Convergence study for the test material response grids was done by conducting a coupled calculation between the grid blocks to examine instantaneous (at 15, 40 and 200 s) temperature distribution along the axial distance. The computed results for the Coarse, Base and Fine grids are shown in Fig. 3.15. An acceptably converged solution was observed between the Base and Fine grids with an error margin of about 1%. A peculiar deviation in results was observed with the Coarse grids, particularly after 40 sec of calculation. The error margin between these two grid systems shot up to about 8% around this time. This could be quite influential in determining the temperature time history distribution, especially at the inner depths of the test specimen. Therefore, the Base grids were deemed sufficient enough to achieve a converged solution.

References

[1] Sakai, T., “Computational Simulation of High-Enthalpy Arc Heater Flows,” *Journal of Thermophysics and Heat Transfer*, Vol. 21, No. 1, 2007, pp. 77–85.

[2] Nicolet, W. E., Shepard, C. E., Clark, K. C., Balakrishnan, A., Kesselring, J. P., Suchsland, K. E., Resse, J. J., “Analytical and Design Study of High-pressure, High-enthalpy Constricted Arc Heater,” AEDC-TR-75-47, July, 1975.

[3] Sakai, T., “The Computation of Strongly Radiating Hypersonic Flowfields,” Ph.D. Thesis, Department of Aeronautics and Space Engineering, Tohoku University, Japan, 1999.

[4] Suzuki, T., “Study of Ablative Heatshied for Entry Capsule,” Ph.D. Thesis, Department of Aeronautics and Space Engineering, Tohoku University, Japan, 2004.

[5] Suzuki, T., Sakai, T., and Yamada, T., “Calculation of Thermal Response of Ablator Under Arc-Jet Condition,'' *Journal of Thermophysics and Heat Transfer,* Vol. 21, No. 2, 2007, pp. 257–266.

[6] Sakai, T., Suzuki, T., Fujita K., and Ito T., “Calculation of High-Enthalpy Aerothermal Environment in an Arcjet Facility,” *Journal of Thermophysics and Heat Transfer*, Vol. 21, No. 1, 2007, pp. 249–251.

[7] Park, C., “*Nonequilibrium Hypersonic Aerothermodynamics*,” Wiley, New York, 1990.

[8] Blottner, F. G., Johnson, M., Ellis, M., “Chemically Reacting Viscous Flow Program for Multi-Component Gas Mixture,” Sandia Laboratories, Albuquerque, New Mexico, Report No. SC-RR-70-754, 1971.

[9] Ahn, H.-K., Sawada, K., and Park, C., “CFD Calculation of Heat Fluxes in Turbulent Flow for Pioneer-Venus Probe,” AIAA Paper 98-0833, 1998.

[10] Vincent, W. G., and Kruger, C. H., “*Introduction to Physical Gas Dynamics*,” Wiley, New

York, 1967, pp. 375–435.

[11] Wilke, C. R., “A Viscosity Equation for Gas Mixtures,” *Journal of Chemical Physics*, Vol. 18, No. 4, 1950, pp. 517–519.

[12] Park, C., “Review of Chemical-Kinetic Problems of Future NASA Missions, I: Earth Entries,” *Journal of Thermophysics and Heat Transfer*, Vol. 7, No. 3 1993, pp. 385–398.

[13] Park, C., Jaffe, R. L., and Partridge, H., “Chemical-Kinetic Parameters of Hyperbolic Earth Entry,” *Journal of Thermophysics and Heat Transfer*, Vol. 15, No. 1, 2001, pp. 76–90.

[14] Park, C., Howe, J. T., Jaffe, R. L., and Candler, G. V., “Review of Chemical-Kinetic Problems of Future NASA Missions, II: Mars Entries,” *Journal of Thermophysics and Heat Transfer*, Vol. 8, No. 1 1994, pp. 9–23.

[15] Wada, Y., and Liou, M. S., “A Flux Splitting Scheme With High-Resolution and Robustness for Discontinuities,” AIAA Paper 94-0833, 1994.

[16] Eberhardt, S., and Imlay, S., “Diagonal Implicit Scheme for Computing Flows with Finite Rate Chemistry,” *Journal of Thermophysics and Heat Transfer*, Vol. 6, No. 2 1992, pp. 208–216.

[17] Horiuchi, T., Sakai, T., Fukui, H., Shimamoto, D., Hotta, Y., Ishida, Y., Suzuki, T., and Fujita, K. “Thermal Response Analysis of Porous Carbon-based Non-Ablative Heatshield in An Arcjet Flow Condition,” Transactions of Japan Society for Aeronautical and Space Sciences, Vol. 61, No. 5, 2018, pp. 211–218.

[18] Petrasch, J., Wyss, P., and Steinfeld, A., “Tomography-based Monte Carlo Determination of Radiative Properties of Reticulate Porous Ceramics,” *Journal of Quantitative Spectroscopy and Radiative Transfer*, Vol. 105, 2007, pp. 180–197.

[19] Coquard, R., Baillis, D., and Randrianalisoa, J., "Homogeneous Phase and Multi-phase Approaches for Modeling Radiative Transfer in Foams," *International Journal of Thermal Sciences*, Vol. 50, No. 9, 2011, pp. 1648–1663.

[20] Kaviany, M., "Principles of Heat Transfer in Porous Media," 2nd Edition Springer, pp. 391–425.

[21] Potts, R. L., "Application of Integral Methods to Ablation Charring Erosion, A Review," *Journal of Spacecrafts and Rockets*, Vol. 32, No. 2, 1995, pp. 200–209.

[22] Gokcen, T., "Computation of Nonequilibrium Viscous Flows in Arc-Jet Wind Tunnel Nozzles," AIAA Paper 94-0254, 1994.

[23] Chen, Y.-K., Gökçen, T., and Edquist, K. T., "Two-Dimensional Ablation and Thermal Response Analyses for Mars Science Laboratory Heat Shield," *Journal of Spacecraft and Rockets*, Vol. 52, No. 1, January–February 2015, pp. 134–143.

Table [3. 1] Molecular weight, formation enthalpies and constant volume specific heats

Species	M_s [kg/mol]	h_s^o [J/mol]	C_{v_s} [J/mol. K]
N	0.0140067	4.707e+5	12.472
O	0.0160000	2.46814e+5	12.472
N_2	0.0280134	0.0	20.786
O_2	0.0320000	0.0	20.786
NO	0.0300067	8.9789e+4	20.786
N^+	0.0140062	1.873e+6	12.472
O^+	0.0159995	1.561e+6	12.472
N_2^+	0.0280129	1.503e+6	20.786
O_2^+	0.0319995	1.165e+6	20.786
NO^+	0.0300062	9.842e+5	20.786
C	0.0120000	7.112e+5	12.472
C_2	0.0240000	8.293e+5	20.786
CN	0.0260067	4.368e+5	20.786
CO	0.0280000	-1.138e+5	20.786
C_3	0.0360000	8.110e+5	24.944
C^+	0.0119995	1.798e+6	12.472
H	0.0010079	2.160e+5	12.472
H_2	0.0020158	0.0	20.786
C_2H	0.0250079	4.739e+5	24.944
H^+	0.0010074	1.528e+6	12.472
e^-	5.4858e-7	0.0	12.472

Table [3. 2] Coefficients of viscosity for Blottner model and curve fits

Species	A_s	B_s	C_s
N	0.011557200	0.6031679	-12.4327495
O	0.020314400	0.4294404	-11.6031403
N_2	0.026814200	0.3177838	-11.3155513
O_2	0.044929000	-0.0826158	-9.2019475
NO	0.043637800	-0.0335511	-9.5767430
N^+	0.011557200	0.6031679	-12.4327495
O^+	0.020314400	0.4294404	-11.6031403
N_2^+	0.026814200	0.3177838	-11.3155513
O_2^+	0.044929000	-0.0826158	-9.2019475
NO^+	0.043637800	-0.0335511	-9.5767430
C	-8.328500e-3	0.7703240	-12.7378000
C_2	-8.431100e-3	0.7876060	-13.0268000
CN	-8.381100e-3	0.7860330	-12.9406000
CO	-0.019527394	1.0132950	-13.9787300
C_3	-8.431200e-3	0.7876090	-12.8240000
C^+	-8.328500e-3	0.7703240	-12.7378000
H	-8.391200e-3	0.7743270	-13.6653000
H_2	-8.334600e-3	0.7815380	-13.5351000
C_2H	-8.431100e-3	0.7876060	-13.0268000
H^+	-8.391200e-3	0.7743270	-13.6653000
e^-	0.58980e-16		

Table [3. 3] Harmonic oscillator characteristic vibrational temperatures

Species	$\theta_{v,s}$[K]
N_2	3390.0
O_2	2260.0
NO	2712.0
N_2^+	3390.0
O_2^+	2260.0
NO^+	2712.0
C_2	2712.0
CN	2938.0
CO	3164.0
C_3	1748.0, 92.0, 2944.0
H_2	6328.0
C_2H	2760.0, 920.0, 4600.0

Table [3. 4] Characteristic temperatures and the degeneracies of electronic levels

Species	$\theta_{el1,s}$[K]	$g_{0,s}$	$g_{1,s}$
N	264985.0	4	10
O	113565.0	9	5
O_2	22713, 18927.5	3	2
N^+	113565.0	9	5
O^+	378550.0	4	10
N_2^+	53280.0	2	4
C	71800.0	1	5
C^+	122060.0	2	2

Table [3. 5] Reaction rates coefficients

Reactions	M	C_f	η	$\theta_{d,s}$	T_a	Source
Dissociation reaction						
(1) $N_2+M \rightleftharpoons N+N+M$	N,O,C,H	3.0×10^{16}	-1.6	113,200	$\sqrt{TT_v}$	Ref. [13]
	e^-	3.0×10^{18}	-1.6	113,200	T_v	
	others	7.0×10^{15}	-1.6	113,200	$\sqrt{TT_v}$	
(2) $O_2+M \rightleftharpoons O+O+M$	N,O,C,H	1.0×10^{16}	-1.5	59,500	$\sqrt{TT_v}$	
	others	2.0×10^{15}	-1.5	59,500	$\sqrt{TT_v}$	
(3) $NO+M \rightleftharpoons N+O+M$	N,O,NO,N^+,O^+	1.1×10^{11}	0.0	75,500	$\sqrt{TT_v}$	Ref. [12]
	others	5.0×10^{9}	0.0	75,500	$\sqrt{TT_v}$	
(4) $C_2+M \rightleftharpoons C+C+M$	all	3.7×10^{8}	0.0	69,900	$\sqrt{TT_v}$	Ref. [13]
(5) $CN+M \rightleftharpoons C+N+M$	all	2.5×10^{8}	0.0	87,740	$\sqrt{TT_v}$	
(6) $H_2+M \rightleftharpoons H+H+M$	all	2.2×10^{8}	0.0	48,300	$\sqrt{TT_v}$	
Neutral exchange reaction						
(7) $NO+O \rightleftharpoons N+O_2$		8.4×10^{6}	0.0	19,450	T	Ref. [13]
(8) $N_2+O \rightleftharpoons NO+N$		6.4×10^{11}	-1.0	38,400	T	
(9) $CO+C \rightleftharpoons C_2+O$		2.0×10^{11}	-1.0	58,000	T	
(10) $CO+O \rightleftharpoons O_2+C$		3.9×10^{17}	-0.18	69,200	T	
(11) $CO+N \rightleftharpoons CN+O$		1.0×10^{8}	0.0	38,600	T	
(12) $N_2+C \rightleftharpoons CN+N$		1.1×10^{8}	-0.11	23,200	T	

(13) $CN+O \rightleftharpoons NO+C$		1.6×10^{7}	0.1	14,600	T	
(14) $CN+C \rightleftharpoons C_2+N$		5.0×10^{7}	0.0	13,000	T	
(15) $CO+C_2 \rightleftharpoons C_3+O$		1.0×10^{6}	0.0	41,200	T	
(16) $C_3+N \rightleftharpoons CN+C_2$		1.0×10^{6}	0.0	34,200	T	
(17) $C_3+C \rightleftharpoons C_2+C_2$		1.0×10^{6}	0.0	16,400	T	
(18) $C_2H+H \rightleftharpoons C_2+H_2$		1.0×10^{7}	0.0	16,770	T	

Table [3.5] Reaction rates coefficients (cont'd)

Reactions	M	C_f	η	$\theta_{d,s}$	T_a	Source
Associate ionization reaction						
(19) $N+O \rightleftharpoons NO^{+}+e^{-}$		5.3×10^{6}	-1.6	31,900	T	Ref. [13]
(20) $O+O \rightleftharpoons O_2^{+}+e^{-}$		7.1×10^{-4}	-1.5	80,600	T	Ref. [12]
(21) $N+N \rightleftharpoons N_2^{+}+e^{-}$		4.4×10^{1}	0.0	67,500	T	Ref. [13]
Charge exchange reaction						
(22) $NO^{+}+O \rightleftharpoons N^{+}+O_2$		1.0×10^{6}	0.5	77,200	T	Ref. [12]
(23) $N^{+}+N_2 \rightleftharpoons N_2^{+}+N$		1.0×10^{6}	0.5	12,200	T	
(24) $O_2^{+}+N \rightleftharpoons N^{+}+O_2$		8.7×10^{7}	0.14	28,600	T	
(25) $O^{+}+NO \rightleftharpoons N^{+}+O_2$		1.4×10^{-1}	1.9	26,600	T	
(26) $O_2^{+}+N_2 \rightleftharpoons N_2^{+}+O_2$		9.9×10^{6}	0.0	40,700	T	
(27) $O_2^{+}+O \rightleftharpoons O^{+}+O_2$		4.0×10^{6}	-0.09	18,000	T	Ref. [12]
(28) $NO^{+}+N \rightleftharpoons O^{+}+N_2$		3.4×10^{7}	-1.08	12,800	T	
(29) $NO^{+}+O_2 \rightleftharpoons O_2^{+}+NO$		2.4×10^{7}	0.41	32,600	T	
(30) $NO^{+}+O \rightleftharpoons O_2^{+}+N$		7.2×10^{6}	0.29	48,600	T	
(31) $O^{+}+N_2 \rightleftharpoons N_2^{+}+O$		9.1×10^{5}	0.36	22,800	T	
(32) $NO^{+}+N \rightleftharpoons N_2^{+}+O$		7.2×10^{7}	0.0	35,500	T	

Electron impact ionization reaction						
(33) $N + e^- \rightleftharpoons N^+ + e^- + e^-$		2.5×10^{28}	-3.82	168,200	T_v	Ref. [13]
(34) $O + e^- \rightleftharpoons O^+ + e^- + e^-$		3.9×10^{27}	-3.78	158,500	T_v	
(35) $C + e^- \rightleftharpoons C^+ + e^- + e^-$		3.7×10^{25}	-3.0	130,720	T_v	
(36) $H + e^- \rightleftharpoons H^+ + e^- + e^-$		2.2×10^{24}	-2.8	157,800	T_v	

Table [3. 6] Equilibrium constant coefficients

Reactions	A_1	A_2	A_3	A_4	A_5
(1)	1.0606000	15.388700	1.392300	-11.53300	-0.004543
(2)	0.641830	16.240800	1.902600	-6.62770	0.035151
(3)	0.638170	14.497390	0.663360	-7.57730	-0.011025
(4)	-0.003732	-1.743400	-1.239400	-0.94952	-0.046182
(5)	0.967940	0.891310	0.729100	-3.95550	0.006488
(6)	-0.658710	-7.274200	-2.109600	-3.18230	0.013310
(7)	1.051600	-8.153000	-0.580820	-8.52510	0.037629
(8)	-2.493800	-5.014500	-5.165400	-5.65770	-0.044602
(9)	-0.950720	1.451300	-2.134600	-6.83130	-0.058964
(10)	0.093083	-0.047212	-1.409760	-0.55958	-0.037891
(11)	-2.66070	2.330000	-3.662800	-1.48870	-0.083264
(12)	-1.63550	0.830580	-2.995200	-1.37940	-0.079927
(13)	-2.58110	2.286300	-5.094600	-2.03780	-0.121920
(14)	-1.02900	-0.243940	-1.907200	-1.05870	-0.049527
(15)	-0.28311	-0.270560	0.131520	-1.49630	0.014474
(16)	1.71390	0.864690	2.767900	-4.39320	0.070493
(17)	1.71000	-0.878690	1.528200	-5.34260	0.024301
(18)	-1.55220	2.530300	-3.187600	-0.97903	-0.072396
(19)	-1.83520	2.259700	-3.056000	-2.47540	-0.057919
(20)	0.66478	7.843900	-0.584860	-16.21200	0.023273
(21)	-0.96709	10.417900	-2.340800	-16.64200	-0.010477
(22)	2.53886	15.597894	5.753987	-10.29616	0.296264
(23)	1.36071	14.774430	2.726324	-9.879787	0.044408
(24)	1.81733	15.017835	4.427498	-7.574115	0.185211
(25)	-2.29436	1.852541	-5.069929	-2.926134	-0.268345
(26)	-1.33413	0.946191	-3.531516	-5.130943	-0.146341
(27)	-1.11621	2.676006	-2.042267	-3.342510	-0.016489
(28)	-4.65440	0.040068	-10.963353	4.353604	-0.626582
(29)	1.62221	0.038401	3.270306	-2.942305	0.109134
(30)	-1.17815	-0.823465	-3.027662	0.416377	-0.0251856
(31)	3.94837	-2.399362	1.776403	-4.373308	-0.036555
(32)	-5.89939	5.259174	-5.060829	1.734790	-0.034435
(33)	-4.34056	4.842954	-2.825133	-1.197910	0.035351
(34)	2.54801	-1.020366	3.425799	-1.864180	0.071191
(35)	-0.28368	7.775281	-1.824398	-12.789612	-0.036117
(36)	-0.19210	7.539211	-1.903784	-15.510915	-0.025936

Table [3. 7] Coefficients for the vibrational relaxation time

Molecular species	Collision partner	A	B
N_2	N	180	23.1
	O	72.4	19.5
	N_2	221	24.8
	O_2	229	25.2
	NO	225	25.0
	N^+	180.73	23.2
	O^+	188.74	23.5
	N_2^+	221.35	24.8
	O_2^+	228.58	25.2
	NO^+	225.12	25.0
	C	171.42	22.8
	C_2	212.63	24.5
	CN	217.20	24.7
	CO	221.32	24.8
	C_3	234.75	25.4
	C^+	171.43	22.8
	H	58.34	19.3
	H_2	81.10	19.8
	C_2H	214.98	24.6
	H^+	58.35	19.3
O_2	N	72.4	19.5
	O	47.7	21.2
	N_2	134	22.4
	O_2	138	22.6
	NO	136	22.5
	N^+	108.21	21.3
	O^+	113.22	21.5
	N_2^+	133.99	22.4
	O_2^+	138.67	22.6
	NO^+	136.42	22.5
	C	102.41	21.1
	C_2	128.38	22.1
	CN	131.31	22.3
	CO	133.97	22.4
	C_3	142.69	22.8
	C^+	102.42	21.1
	H	34.27	18.9
	H_2	47.74	19.3
	C_2H	129.89	22.2
	H^+	34.28	18.9

Table [3. 7] Coefficients for the vibrational relaxation time (cont'd)

Molecular species	Collision partner	A	B
NO	N	49.5	20.5
	O	49.5	20.5
	N_2	49.5	20.5
	O_2	49.5	20.5
	NO	49.5	20.5
	N^+	137.44	22.0
	O^+	143.68	22.3
	N_2^+	169.29	23.4
	O_2^+	175.02	23.6
	NO^+	172.27	23.5
	C	130.22	21.8
	C_2	162.41	23.1
	CN	166.01	23.2
	CO	169.27	23.4
	C_3	179.92	23.9
	C^+	130.22	21.8
	H	43.92	19.1
	H_2	61.13	19.5
	C_2H	164.26	23.2
	H^+	43.93	19.1
C_2	N	127.69	21.7
	O	133.03	21.9
	N_2	154.36	22.8
	O_2	159.00	23.0
	NO	156.78	22.9
	N^+	127.69	21.7
	O^+	133.03	21.9
	N_2^+	154.36	22.8
	O_2^+	159.00	23.0
	NO^+	156.79	22.9
	C	121.44	21.5
	C_2	148.73	22.6
	CN	151.69	22.7
	CO	154.35	22.8
	C_3	162.93	23.2
	C^+	121.44	21.5
	H	42.23	19.0
	H_2	58.55	19.4
	C_2H	150.25	22.6
	H^+	42.24	19.0

Table [3. 7] Coefficients for the vibrational relaxation time (cont'd)

Molecular species	Collision partner	A	B
CN	N	149.84	22.3
	O	156.30	22.6
	N_2	182.38	23.7
	O_2	188.11	23.8
	NO	185.37	23.8
	N^+	149.84	22.3
	O^+	156.31	22.6
	N_2^+	182.38	23.7
	O_2^+	188.11	23.9
	NO^+	185.37	23.8
	C	142.31	22.0
	C_2	175.45	23.4
	CN	179.08	23.5
	CO	182.36	23.7
	C_3	192.97	24.1
	C^+	142.31	22.0
	H	48.92	19.1
	H_2	67.93	19.6
	C_2H	177.32	23.4
	H^+	48.93	19.1
CO	N	161.69	22.7
	O	168.86	22.9
	N_2	198.03	24.2
	O_2	204.50	24.4
	NO	201.40	24.3
	N^+	161.70	22.7
	O^+	168.86	22.9
	N_2^+	198.03	24.2
	O_2^+	204.50	24.4
	NO^+	201.40	24.3
	C	47.7	22.3
	C_2	190.24	23.8
	CN	194.31	24.0
	CO	198.00	24.2
	C_3	210.01	24.7
	C^+	153.38	22.3
	H	52.20	19.2
	H_2	72.57	19.7
	C_2H	192.33	23.9
	H^+	52.21	19.2

Table [3. 7] Coefficients for the vibrational relaxation time (cont'd)

Molecular species	Collision partner	A	B
C_3	N	1.52	18.5
	O	1.59	18.5
	N_2	1.90	18.5
	O_2	1.97	18.5
	NO	1.93	18.5
	N^+	1.52	18.5
	O^+	1.59	18.5
	N_2^+	1.90	18.5
	O_2^+	1.97	18.5
	NO^+	1.93	18.5
	C	1.43	18.5
	C_2	1.81	18.5
	CN	1.86	18.5
	CO	1.90	18.5
	C_3	2.03	18.5
	C^+	1.43	18.5
	H	0.47	18.4
	H_2	0.66	18.4
	C_2H	1.83	18.4
	H^+	0.47	18.4
H_2	N	180.24	21.5
	O	181.67	21.6
	N_2	186.19	21.7
	O_2	186.97	21.7
	NO	186.61	21.7
	N^+	180.24	21.5
	O^+	181.67	21.6
	N_2^+	186.19	21.7
	O_2^+	186.97	21.7
	NO^+	186.61	21.7
	C	178.37	21.5
	C_2	185.15	21.7
	CN	185.71	21.7
	CO	186.19	21.7
	C_3	187.59	21.7
	C^+	178.37	21.5
	H	111.30	19.9
	H_2	136.31	20.5
	C_2H	185.44	21.7
	H^+	111.32	19.9

Table [3. 7] Coefficients for the vibrational relaxation time (cont'd)

Molecular species	Collision partner	A	B
C_2H	N	31.14	19.2
	O	32.46	19.3
	N_2	37.77	19.5
	O_2	38.93	19.5
	NO	38.38	19.5
	N^+	31.14	19.2
	O^+	32.46	19.3
	N_2^+	37.77	19.5
	O_2^+	38.93	19.5
	NO^+	38.38	19.5
	C	29.59	19.2
	C_2	36.37	19.4
	CN	37.10	19.5
	CO	37.77	19.5
	C_3	39.92	19.6
	C^+	29.59	19.2
	H	10.23	18.6
	H_2	14.19	18.7
	C_2H	36.75	19.5
	H^+	10.23	18.6

Table [3. 8] Ionization potentials of atomic species

Species	E_∞[eV]
N	14.53414
O	13.61806
C	11.26030
H	13.59844

Table [3. 9] Flow field and material computational meshes

Grids	Coarse	Base	Fine
Flow field:			
Arc heater	-	126×40	126×80
Test chamber	105×30	105×70	105×150
Material:			
B1	15×100	36×100	45×100
B2	11×90	11×90	11×90
B3	6×90	8×90	8×90
B4	18×70	41×70	76×70

Table [3. 10] Arc heater section grid convergence study results

Description	Base grids	Fine grids	% difference
Mass flow rate, g/s	18.42	18.43	0.05
Mass averaged enthalpy, MJ/kg	14.42	14.59	1.16
Wall pressure, kPa	565.2	567.9	0.48

Table [3. 11] Test chamber flow grid convergence study results

Description	Base grids	Fine grids	% difference
Wall refinement, mm	0.003	0.001	66.67
Stagnation point Pitot pressure, kPa	52.83	52.77	0.11
Stagnation point heat flux, MW/m^2	12.30	12.38	0.65

Table [3. 12] Flow grid convergence results for coupling calculations

Description	Coarse grids	Base grids	Fine grids
Stagnation point heat flux, MW/m^2	2.825	3.145	3.209
Difference between results, %	10.2		2.0

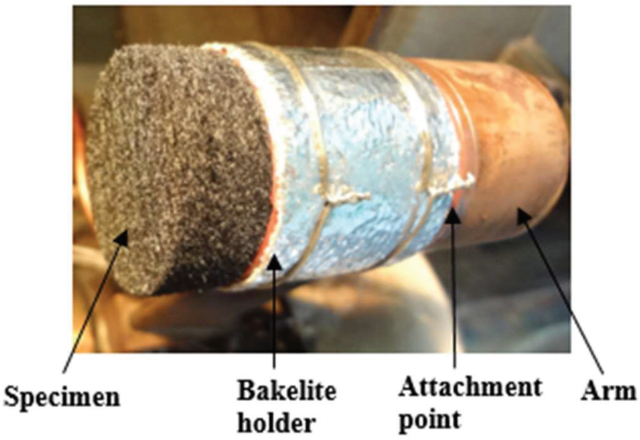

(a) Specimen set up

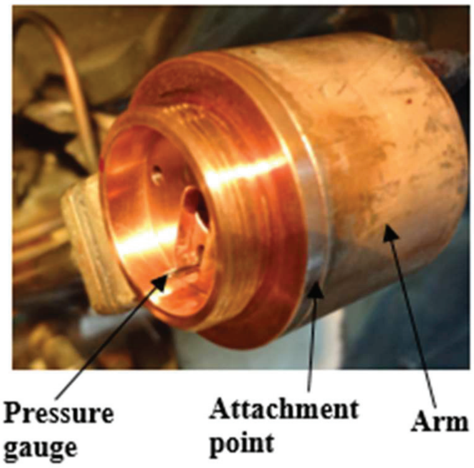

(b) Gauge inside the arm

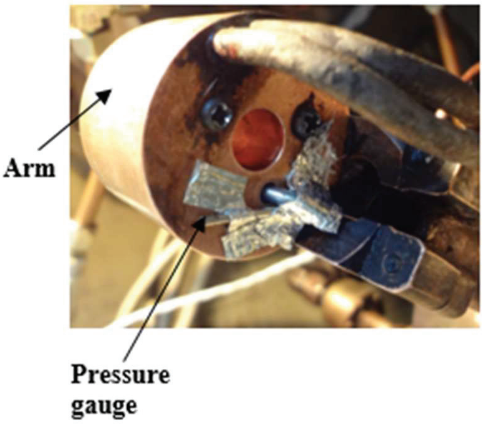

(c) Gauge outside the arm

Fig. 3.1 Illustration of rear surface pressure transducer positions

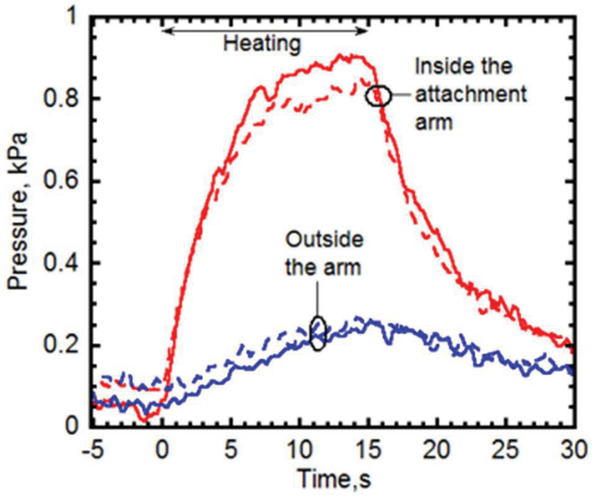

Fig. 3.2 Rear surface pressure time histories

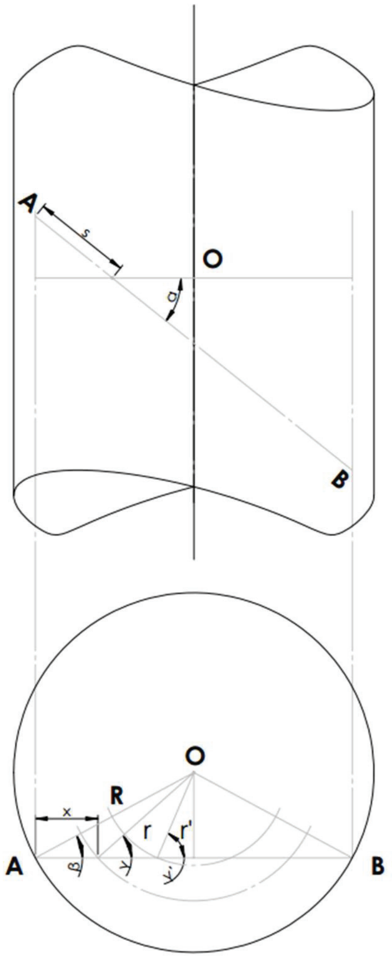

Fig. 3.3 Geometry for the cylindrical coordinates

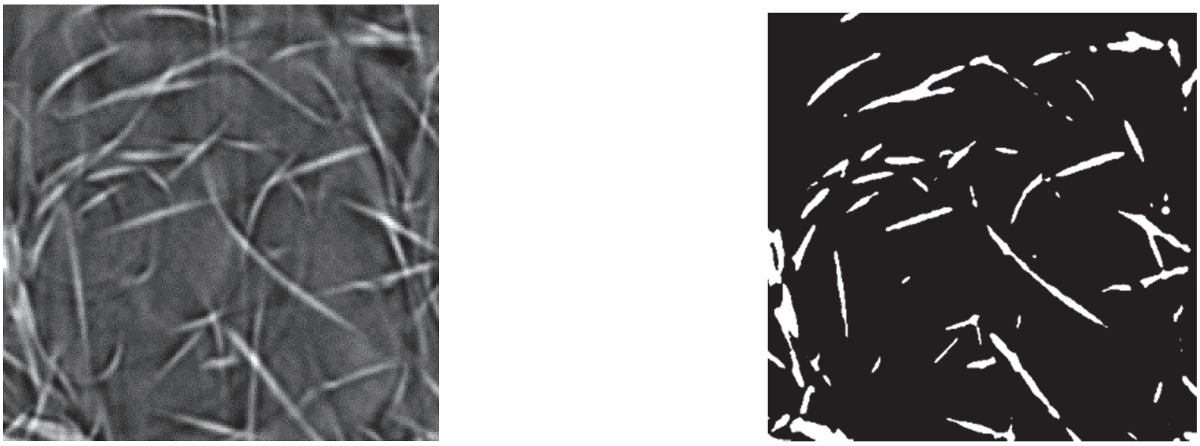

(a) 0.12 g/cm^3

Fig. 3.4 Tomogram (left) and binarized (right) images of the porous carbon materials

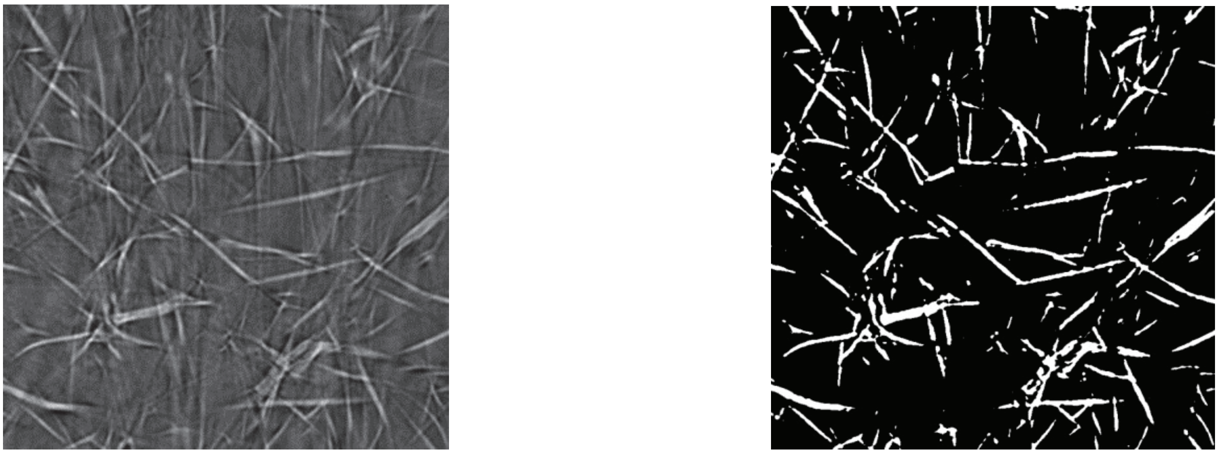

(b) 0.15 g/cm^3

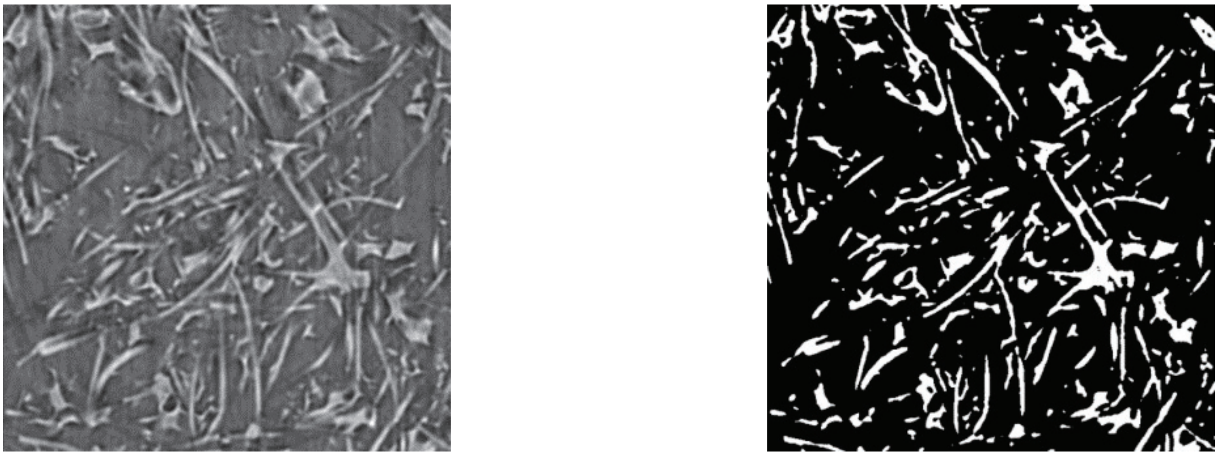

(c) 0.27 g/cm^3

Fig. 3.4 Tomogram (left) and binarized (right) images of the porous carbon materials

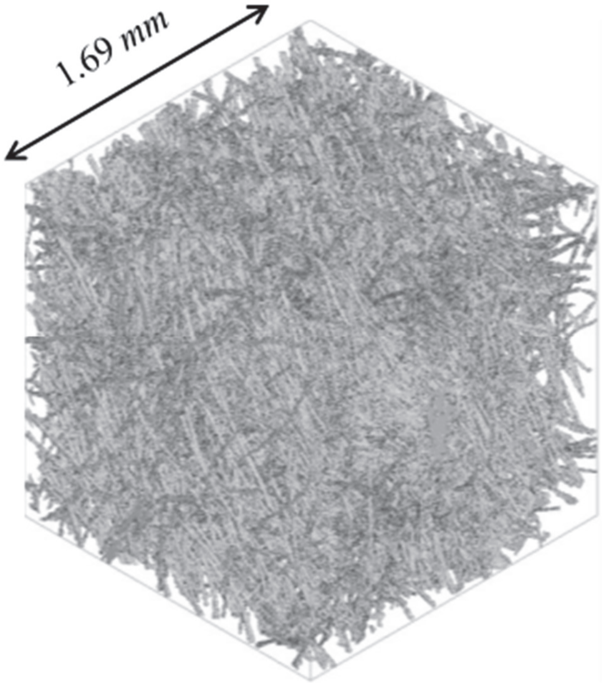

Fig. 3.5 3D digital model's elementary volume for the porous carbon materials

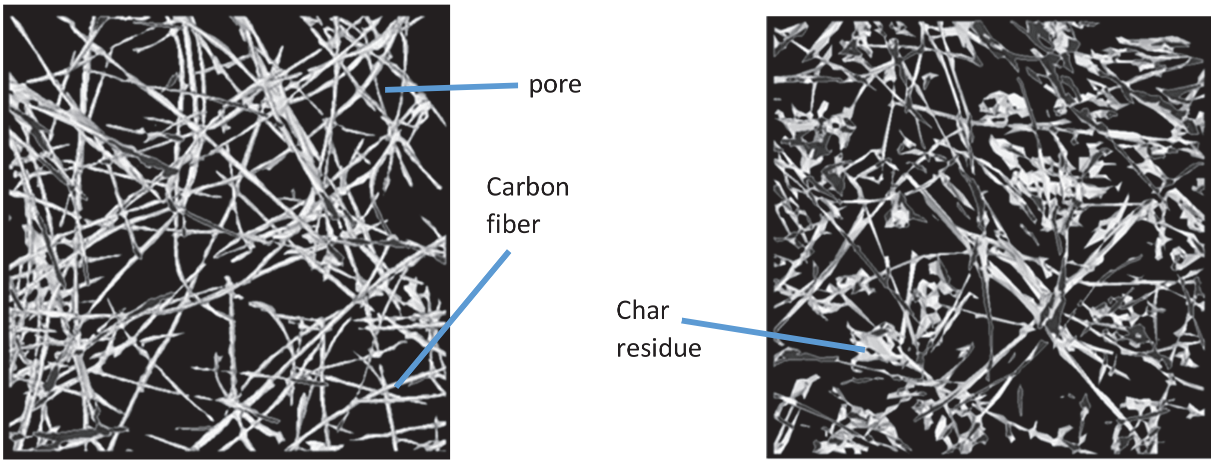

(a) 0.15 g/cm^3 (b) 0.27 g/cm^3

Fig. 3.6 Cross-sectional views of the STL models

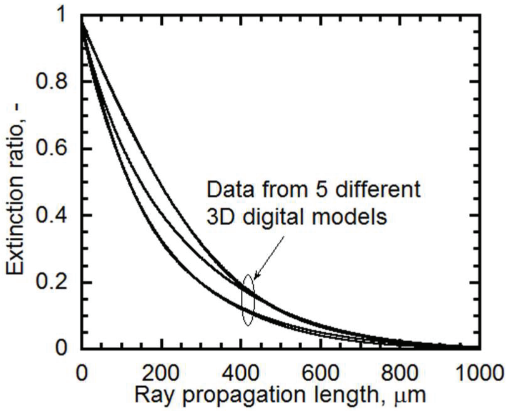

(a) 0.12 g/cm^3

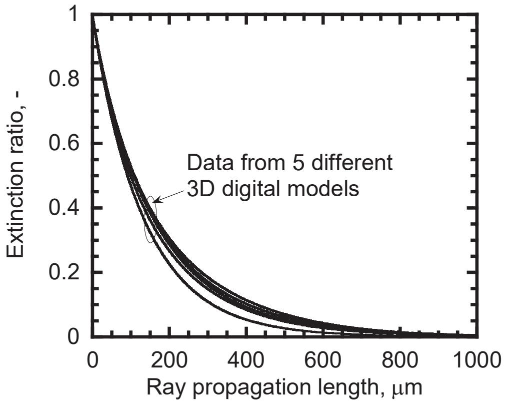

(b) 0.15 g/cm^3

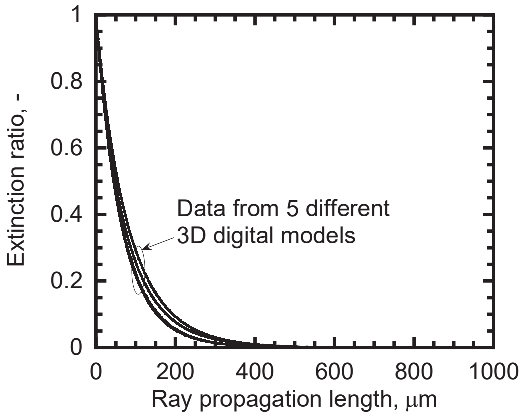

(c) 0.27 g/cm^3

Fig. 3.7 Variation of extinction ratio with ray path length

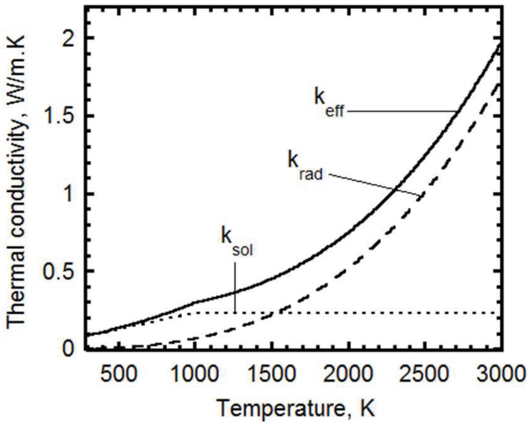

(a) 0.12 g/cm^3

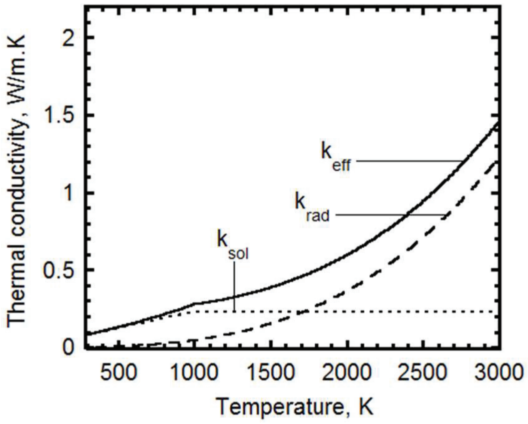

(b) 0.15 g/cm^3

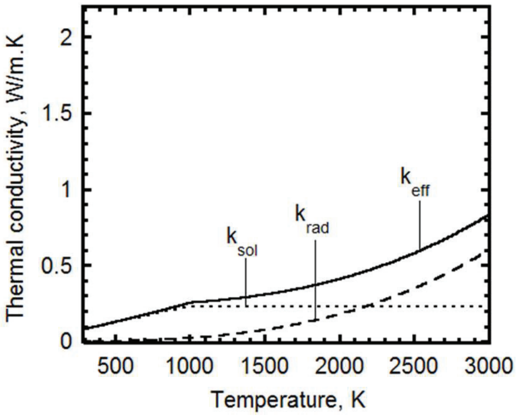

(c) 0.27 g/cm^3

Fig. 3.8 Effective thermal conductivity variation with temperature

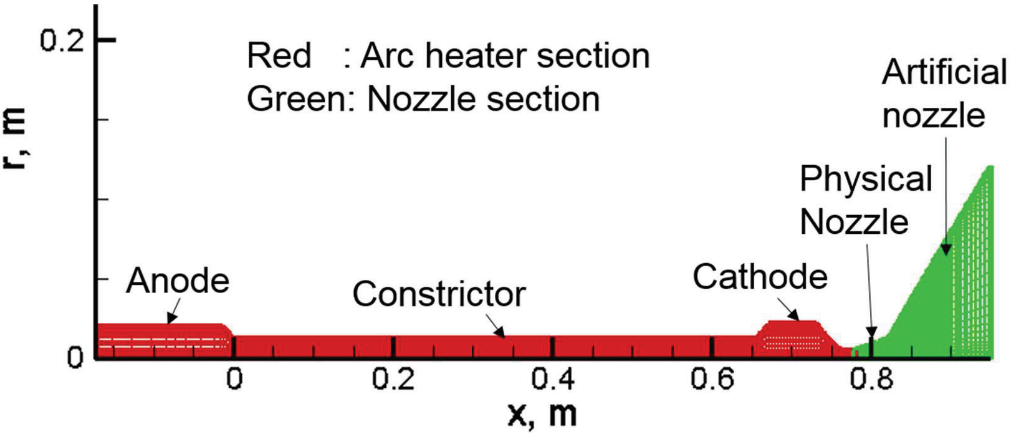

Fig. 3.9 Computational mesh for the arcjet freestream analysis

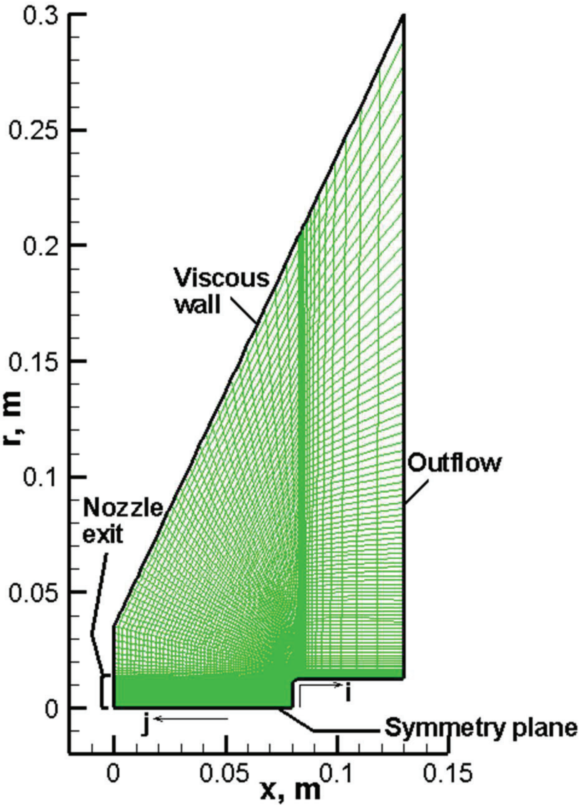

Fig. 3.10 Computational mesh for calculation of the test section flow fields

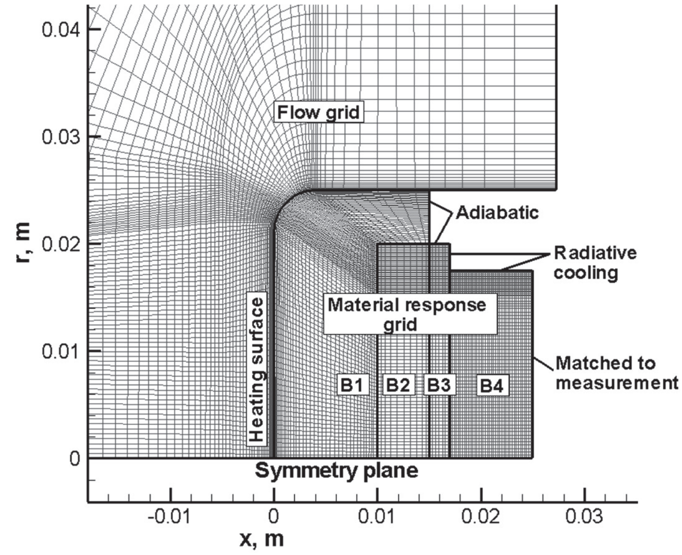

Fig. 3.11 Grid blocks for the coupling calculation

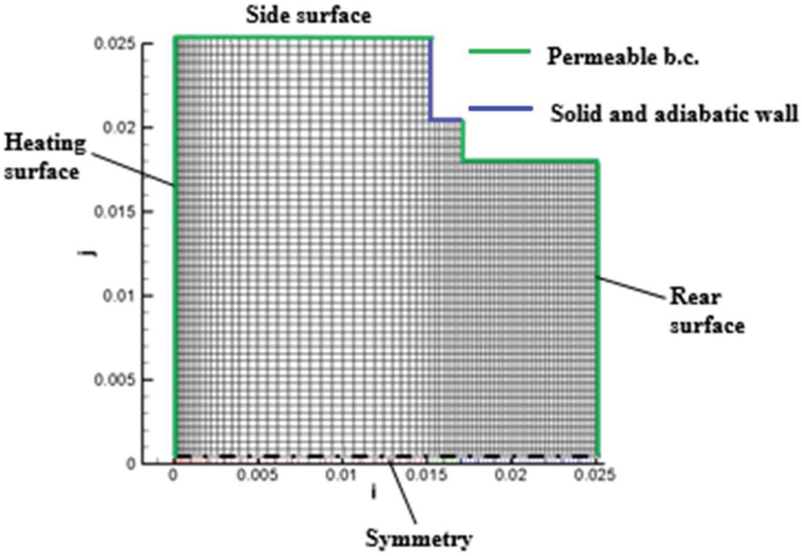

Fig. 3.12 Uncoupled calculation grid blocks

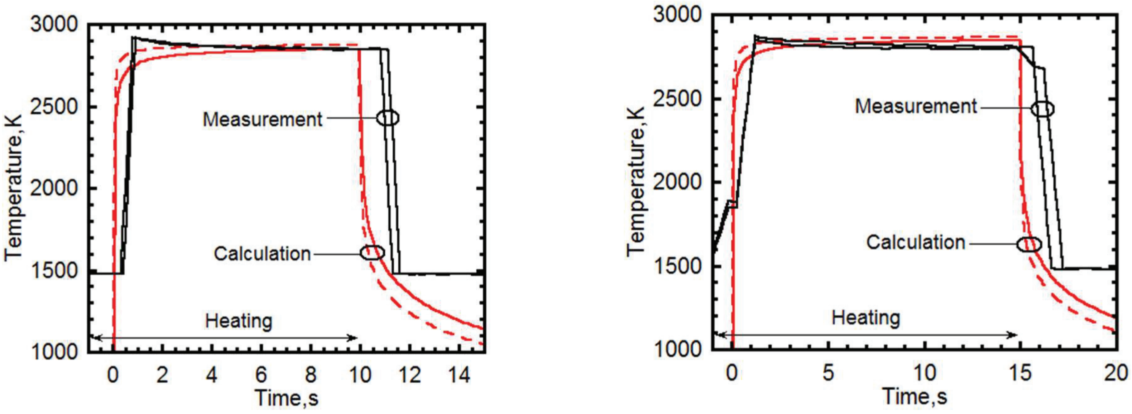

(a) 0.12 g/cm^3 (b) 0.15 g/cm^3

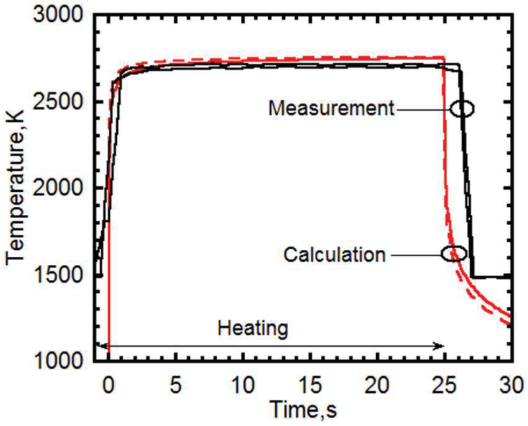

(c) 0.27 g/cm^3

Fig. 3.13 Comparison of measured and calculated surface temperature time histories

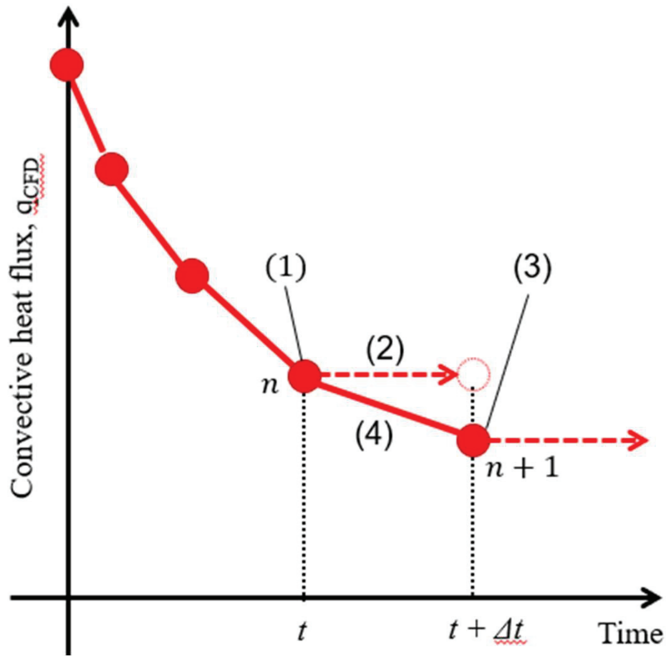

Fig. 3.14 Coupling process between arcjet flow and test material response calculations

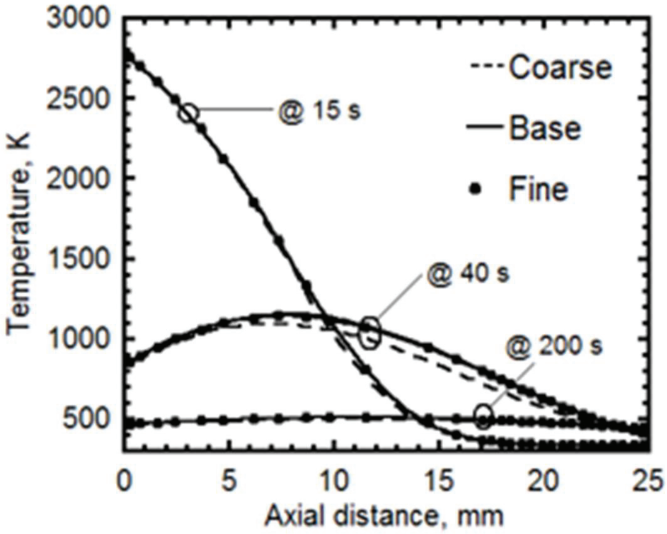

Fig. 3.15 Instantaneous axial temperature distribution

Chapter 4

Results and Discussion

4.1 Introduction

In this chapter, results from the experiments and calculations undertaken in this study are described and discussed. The computed results are presented to see how our present methodologies numerically demonstrate the arcjet flow field and the heating tests in this study. The results are then discussed giving possible reasons for any cases of disparity noted. The computed results include: operating conditions within the heater section and flow properties over the shock layer, heat flux distribution and surface temperature time histories, radiative transfer during heating and the in-depth temperature field development. This study results are divided into two sections: arcjet flow modeling, and TPS thermal response analysis. The arcjet flow modeling is further divided into Case 1 and Case 2 calculation while the TPS thermal response is analyzed through both coupled and uncoupled calculations. A summary of these calculations is given in Table 4.1 Both the results and discussion are presented as follows:

4.2 Arcjet Flow Analysis

4.2.1 Arc Heater Operating Conditions

Calculation results for the high enthalpy arc heater operating conditions were compared with the measured data as summarized in Table 4.2. From the Table, several parameters were measured during the first set of experiments. However, of particular importance to our study was the mass averaged enthalpy. This is because the mass averaged enthalpy helps us to understand the amount of heat energy that is distributed within the test materials. From the results, the maximum error margin between calculation and measurement was worked out and presented. The numerically computed mass averaged enthalpy was also compared against the manually calculated value and the difference between the two noted. Finally, results for the difference between the calculated and measured arcjet mass flow rate was presented. These results are discussed follows below.

The main reason for studying the arc heater operating conditions and flow field distribution of the arcjet freestream properties was to validate the ARCFLO3+ code set and the CFD flow calculation codes. Calculated data were compared against the data for several parameters measured during the experiments. The measured parameters during the experiments as presented in Table 4.2. From the results, maximum error margin of about 2% between the calculated and the measured mass averaged enthalpy was recorded. Furthermore, the numerically computed mass averaged enthalpy was compared against the manually calculated value and the difference between the two found to be 0.35%. This was a clear indication of an excellent demonstration of mass conservation. The difference between the calculated and the measured arcjet mass flow rate was found to be less than 1%. As a result, a fair validation success was achieved for the ARCFLO3+ code set. Going by these results, it is sufficient to state that good results agreement was achieved.

4.2.2 Distribution of the Arcjet Flow Properties

In the first set of experiments for the study of the arc heater operating conditions and flow over the flat faced test probe, two sets of calculations named as ‘Case 1’ and ‘Case 2’ were carried out as indicated in Table 4.1. In Case 1 calculations, the input arc heater power was matched with the measured experimental value. Case 2 calculations, on the other hand, were conducted using reduced arc heater input power to try and match the measured mass averaged enthalpy with the calculated value. Thereafter, the calculated results were compared between Case 1 and Case 2 as well as with the corresponding measured data. First, the centerline momentum flux and total enthalpy distributions along the axial direction were compared for Case 1 and Case 2 results as shown in Fig. 4.1. Note that, based on normal shock relations, momentum flux is a measure of the Pitot pressure value behind the shock wave over the Pitot probe. Results were compared for both Case 1 and Case 2 calculations in which the flat faced blunt body was placed 80 mm away from the nozzle exit. A near constant difference in momentum flux results of about 5% was maintained between the two calculation cases up to the downstream region. However, as seen from Fig. 4.1, this difference seemed to diminish further downstream of the nozzle exit. The centerline enthalpy values, also shown in Fig. 4.1, were generally constant along the entire axial distance. The value of the mass averaged enthalpy in the arc heater section for Case 2 calculations was lower than that for Case 1 calculations by about 14% due to the reduced value of the input power used in Case 2 calculations. As a result, centerline total enthalpy for Case 2 calculations was reduced by about 19% compared to Case 1 calculations results.

The measured stagnation point Pitot pressure values at various axial positions of 50, 60, 70 and 80 mm from the physical nozzle exit were compared with their corresponding calculated pressure distributions as shown in Fig. 4.2. Finally, the measured heat flux values were compared with their corresponding calculated heat flux and the total enthalpy distribution values at the same axial positions as shown in Fig. 4.3. For the heat flux calculations, the limiting cases of non-catalytic and fully catalytic flows, represented by the dotted and continuous graphs respectively, were considered alongside the total enthalpy just ahead of the shock wave as displayed in Fig. 4.3. In the fully catalytic case, the surface reactions were totally enhanced whereas the non-catalytic flow prohibited the surface reactions.

From both Fig. 4.2 and 4.3, reasonable comparisons were achieved from the analysis of flow over the blunt body at 50, 60, 70, and 80 mm axial positions from the physical nozzle exit. Results were also compared for Case 1 and Case 2 calculations. Radial profiles for the momentum flux ahead of the shock wave and radial profiles for the total enthalpy for each axial position are included in Fig. 4.2 and 4.3, respectively for reference purposes.

For the heat flux calculations, results for both the fully catalytic and non-catalytic cases were included to demonstrate the prediction accuracy criteria for the present approach. Generally, the heat flux measurement using a Gardon gauge assumes a fully catalytic gauge surface. However, the validity of this assumption is highly unlikely for a dissociated flow like in the case of the arcjet flows. As a result, the catalytic efficiency could decrease in such flow cases. In the present approach, the atomic oxygen was present in a fully dissociated state, and the mass fraction of the atomic nitrogen at the centerline was about 0.144. Even though, the effective catalytic efficiency in measurements is unknown, the lowest possible efficiency could be the non-catalytic case. Since the experimental centerline enthalpy is also unknown currently, a rational argument is the belief that the measured heat flux values fall in between the two calculation values derived from the limiting catalytic efficiency cases. Note that, results for the fully catalytic and non-catalytic calculations are denoted in Fig. 4.3 by continuous and dotted convective heat flux graphs, respectively.

From Fig. 4.2, for the case where the flat faced blunt body was placed 50 mm away from the nozzle exit, radial non-uniformity of the wall pressure along the surface is clearly visible. Based on the calculated momentum flux distribution ahead of the shock wave shown in the same Figure, expansion processes of the arcjet freestream continued right from the downstream region adjacent to the nozzle exit. Even though only Case 2 calculations results were included here, this tendency was qualitatively similar to Case 1 calculations results. Therefore, this non-uniformity in the radial direction was believed to be physically reasonable.

From the compared results, calculations were able to reasonably and acceptably predict the measurement trends. Case 1 calculations registered higher centerline results' deviation from the measured data by about 11%. A general agreement in the results was achieved with the other three axial position calculations for this particular case, with the maximum error in the compared results falling within 6%. Surprisingly, the pronounced overestimated arc heater pressure shown in Table 4.2 was quite minimized in this region. Improved results' harmony, in particular for the centerline values, was achieved with Case 2 calculations as demonstrated in both Fig. 4.2 and 4.3, although these results tended to underestimate the measurements away from the centerline in Fig. 4.2.

It is believed that the obtained overestimated mass averaged enthalpy in Case 1 calculations within the arc heater section strongly influenced the resulting heat flux values in the test section. From Fig. 4.3, it is quite evident that both the non-catalytic and fully catalytic results in Case 1 calculations overestimated the measurement. From these results' observation, it could be argued that the source of error in the calculations could be as a result of the higher calculated mass averaged enthalpy value in the arc heater section. On the contrary, Case 2 calculation results (for which the measured and calculated mass averaged enthalpies acceptably agreed) were able to capture the measured heat flux values in between the two limiting wall catalytic efficiency cases. Since Case 2 calculation results offered a satisfactory and consistent agreement with the other available experimental data, the impact of replicating the arc heater operational characteristics data on the prediction accuracy of the downstream arcjet freestream in the test section is believed to have been well demonstrated.

Results' comparisons were similarly done for the 60, 70, and 80 mm axial positions in the Fig. 4.2 and 4.3. From Fig. 4.2, calculation results showed that the radial distribution of the momentum flux ahead of the shock wave at each position flattened over the flat faced blunt body. This behavior of the arcjet freestream was well responded to by the calculated radial distribution of the Pitot pressure over the blunt body, and the overall agreement between the calculations and measurements seemed satisfactory. However, Case 1 calculation results tended to overestimate the measured centerline pressure value as was the case for the 50 mm axial position, though the 80 mm case was an exception. Again, Case 2 results offered both reasonable and consistent agreement with the measured data along the axial positions under study.

From Fig. 4.3, calculated radial distributions of the total enthalpy at 60, 70, and 80 mm axial positions were only varied by a slight margin. However, the calculated radial profiles for the wall heat flux values were qualitatively varied along these axial positions. This behavior was mainly due to variation of the radial pressure profiles along the axial positions, as already explained earlier. Case 2 results were able to satisfactorily predict the heat flux values at the centerline for these three axial positions, as expected. The measured values all lay near their corresponding values calculated under fully catalytic conditions. It should be noted that results for Case 1 calculations still showed a reasonable agreement with the measurements under the prediction criteria applied in this study. However, the measured values being closer to the values calculated with non-catalytic conditions implied a likely overestimation of the calculated total enthalpy.

The schematic diagram shown in Fig. 4.4 represents the distributions of the axial velocity and total enthalpy over the entire wind tunnel flow field (i.e. from the heater section up to the test section). The axial velocity and total enthalpy are represented in the figure as indicated by 1 and 2, respectively. From the figure, the axial velocity was seen to increase significantly from the nozzle throat toward the downstream region. The maximum total enthalpy occurred along the centerline of the heater section, and reduced gradually toward the wall. Within the nozzle section and further downstream, the total enthalpy value was relatively uniform in the wider central region.

From the coupling calculation, axial distribution of the arcjet flow temperature T_{tr} and T_{ve}, together with the mole fractions of both the atomic and molecular nitrogen species were plotted as shown in Fig. 4.5. The finite catalytic calculation results, immediately after heating, for the 0.15 g/cm^3 test material were displayed. The other test materials depicted similar trends in the behavior of the arcjet flow properties and therefore, their results were omitted. The shock standoff distance within the flow field is also indicated in Fig. 4.5(a).

From Fig. 4. 5(a), the effective shock layer thickness was defined by the shock standoff distance which was about 7 mm from the test material's heating surface. In Fig. 4.5(b), for the atomic and molecular nitrogen species' mole fractions, the finite catalytic calculation results at the end of heating indicated a near frozen chemical state within the shock layer. This state warranted large amounts of atomic nitrogen to reach the test material's wall surface. Reduction and increment in mass fractions of the atomic and molecular nitrogen, respectively, were observed at the boundary layer. This was due to the effect of the finite catalytic condition imposed in the calculation to enhance the species recombination reaction. At the heating surface, nitridation reaction facilitated recession at the surface of the test material. In the non-catalytic case, increased atomic nitrogen coupled with lower surface reactions as a result of the lower surface temperatures were expected. The lower surface temperatures in the non-catalytic calculations are generally brought about by the reduced species recombination reaction in the boundary layer.

4.3 TPS Thermal Response Analysis

During coupling calculation, the results presented were for the axial distribution of the arcjet flow temperature, atomic, and molecular nitrogen species' mole fractions, convective and net heat flux distribution, unsteady thermal diffusion into the test materials during heating, and the stagnation point time histories for both the surface and in-depth temperatures. Thermal response analyses were carried out for cases with (W) and without (W/o) radiative conductivity. Both the surface and in-depth temperature time histories were compared to validate the radiative conductivity model used in this study. Comparisons were also done for the finite catalytic and non-catalytic calculations to examine the effect of heat input from the test specimen's surface. The finite catalytic calculations were done to reproduce the measured surface temperatures with closer accuracy, for purposes of achieving good agreements in the in-depth temperature comparisons as seen in section 4.3.2.2 of this chapter. Since the actual catalytic value is currently unknown, this value was estimated as 0.025 through a trial and error approach. Two test runs of the experimental heating results were used for comparison with calculations. These results are discussed below.

4.3.1 Heat flux and Flow Distribution Analysis

Results for the convective heat flux values, net heat flux values, and the surface temperature time histories during heating, determined through coupling calculation, were plotted in Fig. 4.6. Again, the plotted results were for the 0.15 g/cm^3 test material. The convective heat flux values from CFD calculations q_{CFD} at several instantaneous coupling time-points were plotted against the distance along the heating surface as shown in Fig. 4.6(a). From the figure, the maximum value of q_{CFD} was recorded at the stagnation point, gradually reducing along the surface. This distribution trend indicated that the radial non-uniform arcjet flow properties were accounted for in the calculation. The net heat flux at the surface of the test specimen, given by Eq. (3.85) in section 3.4.4 of Chapter 3, was plotted in Fig. 4.6(c) at the selected time-points. Distribution of the temperature profiles along the heating surfaces of the test materials at the selected time-points were also plotted as shown in Fig. 4.6(b). The net heat flux distributions in Fig. 4.6(c) reduced with increasing surface temperature (Fig. 4.6(b)) during heating. It was also noted that the heating process reached a quasi-steady state after about 1s from the onset. From the results of the net heat flux at the surface of the specimen, reduction of heat input to the test specimen was demonstrated. Since the radius of the test specimen was 25 mm in this case, it suffices to mention that heating from the side surface was negligibly small compared to the contribution from the front surface.

Results for the calculated unsteady thermal diffusion within the test specimens for cases with and without radiative conductivity were compared. Figure 4.7 shows the results for the 0.15 g/cm^3 test material at instantaneous times during heating. The final change of shape at the heated surface of the test material was plotted in Fig. 4.7(b). The calculated unsteady thermal diffusion within the test specimen indicated an enhanced penetration of thermal transfer into the specimen when radiative conductivity term was included as opposed to the results from calculation without radiation. This observation showed the importance of radiation modeling for a reliable thermal response analysis. Temperature contours for two instantaneous times of t=1 and 15s were selected. 15s was chosen to represent the overall heating time for this test material.

The present coupling method effectively predicted the final shape of the test specimen at the heated surface as shown in Fig. 4.7(b). From the figure, a change in the shape of the test material as a result of surface recession can be noted. After heating, recession at the stagnation point (along the axial direction) on the surface of the test specimen was about 0.3 mm. This was largely contributed to by incorporation of the surface chemical reactions, more so nitridation, in the calculations. Though just slight, calculated recession value nearly replicated the corresponding value of 0.3±0.16 mm from the measurements. Moreover, calculation results were able to qualitatively reproduce the concave nature of the heated surface contours. This trend is only possible with coupled calculation in which the non-uniform radial distribution of the arcjet freestream properties must be accounted for. This was successfully achieved in the present study. Also, from the temperature distribution results, the overall agreement between the measurements and the calculations indicated that the selected time-points for the coupling calculations were reasonable enough and that this coupling approach can be argued to have worked acceptably well.

Computed results for the uncoupled calculations, arrived at by solving the gas flow conservation equations and the solid material energy conservation equation are presented next. Figure 4.8 demonstrates the spatial pressure and flow distribution within the pores of the test material. A single demonstration with 0.12 g/cm^3 test material was done to represent the other test materials since their distributions were qualitatively similar. From Fig. 4.8, the spatial pressure distribution within the test materials was seen to penetrate further in-depth from the heating surface with increased heating. Flow was initiated within the test materials by imposing different fractions of the arcjet freestream mass flux to the heating surfaces. Approximate amount of the mass flux for each test material was determined through trial and error approach, in order to achieve finer agreements between the measurements and calculations as will be seen later in Fig. 4.15. The amounts of mass flux used are summarized in Table 4.3. The flow vectors in Fig. 4.8 were used to show proof of flow within the pores of the test materials. The outflow from the rear and sides of the test materials was enhanced by imposing initial conditions at the boundaries along these surfaces.

The role of convective transfer alongside radiative transfer in the overall heat transfer within the test materials is demonstrated in Fig. 4.9. Since the radiative influence had been highlighted in the previous paragraphs of this section, here we only analyzed radiative calculations with and without convective transfer labelled as W/ convection and W/o convection respectively in the Fig. 4.9. Results were compared at two different times, i.e. soon after the onset of heating and just before the heating was terminated. From the results, calculation with convection recorded deeper thermal penetrations with increased heating across all the test materials. The level of penetration varied inversely with the density of the test material. The increased thermal penetration with convection clearly indicated that convective transfer augmented the overall heat transfer.

4.3.2 Temperature Distribution Comparison

4.3.2.1 Surface Temperature Time Histories

Time histories of the surface temperature at the stagnation point, calculated using coupling method, were compared with the measurements as shown in Fig. 4.10. In the comparison, the measured nominal quasi-steady state temperature values were given for all the test materials under study. In this case, the quasi-steady state implies the state for which the change in temperature with time is so slowly that it can be considered constant. Comparison also included results for both the finite-catalytic and non-catalytic calculations. Rapid temperature increase to about the quasi-steady state value was noted immediately after inserting the test specimens into the heating chamber, as shown in Fig. 4.10. The measured nominal quasi-steady temperature values were about 2915, 2870, and 2715 K for 0.12, 0.15, and 0.27 g/cm^3 test materials, respectively. The corresponding value for the finite-catalytic calculation was about 2840 K across all the test specimens. From the comparison, an overall agreement was obtained with finite-catalytic calculation results, even though slight overestimation (about 5%) of the measurements was noted with the 0.27 g/cm^3 material results. Non-catalytic calculations, on the other hand, consistently underestimated the measurements slightly in all the study cases. At this point, just a slight discernible difference was noted between calculation with and without radiative term, although calculation with radiation predicted a bit lower quasi-steady state surface temperature values due to the higher thermal conductivity value used.

In the uncoupled calculations analysis, the surface temperature distribution results were already shown earlier in Fig. 3.13 of Chapter 3. These results were calculated using the normalized heat flux distribution shown in Fig. 4.11. The normalized results in Fig. 4.11 were calculated using heat flux distribution values along the heating surface of the test material, got from the coupled calculations. Details of getting the normalized heat flux distribution had been explained earlier in section 3.4.4 of Chapter 3. The main reason for using the normalized heat flux values instead of the uniform heat flux distribution was to closely capture the radial non-uniformity of the flow field properties, since no coupling approach was implemented in these calculations. By doing so, the quasi-steady state surface temperature for 0.12, and 0.15 g/cm^3 test materials was determined to be about 2800 K while that for the 0.27 g/cm^3 test material was approximately 2700 K. The calculated quasi-steady state surface temperatures in Fig. 3.13 were similarly demonstrated and compared with the corresponding measurement values as was done with the coupled calculations. These values reasonably marched the measurement values of about 2900 K for the 0.12, and 0.15 g/cm^3 test materials and 2715 K for the 0.27 g/cm^3 test material. Matching the surface temperature distribution was purely aimed at achieving a satisfactory agreement in the in-depth temperature comparison as will be confirmed by the results in Fig. 4.14 and 4.15.

4.3.2.2 In-depth Temperature Time Histories

Figure 4.12 shows results comparison between the coupled calculation and measurement temperatures at a depth of 18 mm from the heating surface. In the figure, the measured data from the two experimental test runs were plotted in terms of max-min intervals. Finite-catalytic and non-catalytic results for calculations with radiation (labelled as W/ radiation in the figure) and finite-catalytic results for calculations without radiation (labelled as W/o radiation in the figure) were plotted and compared with the measured data. From the results, calculations with radiation offered a better in-depth temperature agreement with the measurements at the 18 mm depth in all the test cases as opposed to calculations without radiation. Disparity in the calculated results with and without radiation was seen to widen with reducing material density. This trend was effectively consistent with the difference in the effective thermal conductivity values that were shown earlier in Fig. 3.8 of Chapter 3, which indicated that radiative conductivity contribution was appreciated more in the lower density materials. From Fig. 3.8, it was seen that the level of results agreement improved with increasing material density for calculations with radiation. Better prediction of the measured surface temperature data by finite-catalytic calculation led to the overall acceptable agreement obtained with all the test cases for calculations with radiative terms. On the other hand, finite-catalytic calculations without radiation consistently underestimated the measurements across the test materials.

The discrete reason for the observed underestimation of the measurements by 0.12 g/cm^3 test material at the 18 mm depth is currently unclear. Even though the agreement between the measured and the calculated surface temperature was improved by assuming a finite-catalytic effect, prediction accuracy for the in-depth temperature was not satisfactory. Based on the results of Fig. 4.12(a) to (c), the observed difference between the calculation and the measurement seemed to magnify for the cases of lower density materials. In addition, the calculated temperature ramping rates near the heating surfaces were lower than the corresponding rates in the measurements.

One possible reason for this discrepancy was likely due to the convection transport by the gas occupying the pores of the test material, which was ignored in the coupling calculation. The porosity values of the test materials analyzed in this study were in the order of 90% as stated earlier, with 0.12 g/cm^3 test material having the highest value of about 93%. As a result, the heated surface of the test specimen was potentially permeable to the arcjet freestream. This implied that the incoming arcjet flow could deliver energy to the inner depths much faster than thermal conduction. Even if the arcjet flow penetration into the porous material was relatively weak, the pressure difference over the heated surface could promote gas motion through the pores, thereby resulting in convection of heat near the surface to the in-depth position. Such a scenario led to the next analysis in this study where the effect of convective heat transfer on the in-depth temperature time history was examined. This was done by solving conservation equations of the gas within the pores together with the material energy conservation equation whose results are considered in the current discussion.

In Fig. 4.13, results for the uncoupled calculations were plotted and compared with the measurements at 18 mm to demonstrate influence of convective transfer to the overall heat transport within the porous carbon-based materials. Results indicated a reduction in the peculiar phenomenon of delay in the onset of temperature rise during heating. This phenomenon was observed with the earlier coupled calculation which conveniently omitted the heat transfer by convection. A fair agreement between the measured and calculated peak temperatures was also achieved. Comparison results for temperature distribution within the test materials at the same depth were also made and plotted as shown in Fig. 4.14. Results for the level of convective contribution are summarized in Table 4.3. From Fig. 4.14, combined radiative and convective heat transfer results posted a fairly consistent agreement with the measurements, even though slight underestimation and overestimation of the measured peak temperatures by calculations were noted in the 0.12, and 0.27 g/cm^3 test materials, respectively. An investigation was also conducted through calculations with and without convection to verify the contribution of convective transfer to the overall heat transfer. Results indicated that imposing the right amount of arcjet freestream mass flux into the test materials could result in convective transfer that would greatly improve results' agreement in 0.12, and 0.15 g/cm^3 test materials as shown in Fig. 4.15(a) and (b), respectively. However, from Fig. 4.15(c), calculation results for 0.27 g/cm^3 test material were weakly influenced by convective transfer since 0% mass flux was imposed in this case.

At the 23 mm depth position, results for the coupling calculations were compared as shown in Fig. 4.16. From the results, effect of the radiation models and the rear surface boundary conditions on the calculated temperature time histories were relatively weak. A fair agreement of the results was obtained, possibly because calculations were carried out by imposing the measured thermocouple data at the centerline of the material's rear surface (located at 25 mm from the heating surface). Due to the close proximity of the 23 mm position to the rear surface, the effect of imposing such conditions greatly influenced calculations' results at this depth. However, since the accuracy of the temperature condition along the rear surface and off the centerline, as well as along the side surface where radiative cooling boundary condition was imposed (shown in Fig. 3.11 of Chapter 3) is currently unknown, the slight difference observed between calculation and measurements could be attributed to this uncertainty.

Comparison results for the influence of convective strength, given in Fig. 4.15, for the 18 mm depth were also extended to the 23 mm depth as shown in Fig. 4.17. Discussion for the uncoupled calculations' temperature time history results at this depth is basically similar to the one for the coupled calculations results in Fig. 4.16 and therefore, the details have been omitted here.

Table [4. 1] Summary for the numerical simulation analysis

Experiment	Calculation	Description
First set	Case 1	Input power is set to match the measured value
	Case 2	Input power is reduced to match the calculated mass averaged enthalpy value to the measured value
Second set	Coupled	CFD flow code is coupled to material response analysis code
	Uncoupled	Normalized heat flux value from CFD flow analysis is used to set the heating conditions for the material response analysis

Table [4. 2] Comparison of arc heater operating conditions

Condition	Measurements	Calculations	Error margin, %
Mass flow rate, g/s	18.6	18.42	0.97
Heater power, kW	644 ± 7	450.00	30.00
Arc voltage, V	1436 ± 5	2022.00	29.00
Arc current, A	449 ± 4	383.00	14.70
Heater wall pressure, kPa	510 ± 1	565.30	10.84
Mass average enthalpy, MJ/kg	14.7	14.41	1.97
Thermal efficiency, %	42	58.77	39.93

Table [4. 3] Computational conditions for the convection analysis

Description	Material 1	Material 2	Material 3
Density, g/cm^3	0.12	0.15	0.27
Mass flux, %	4	2	0

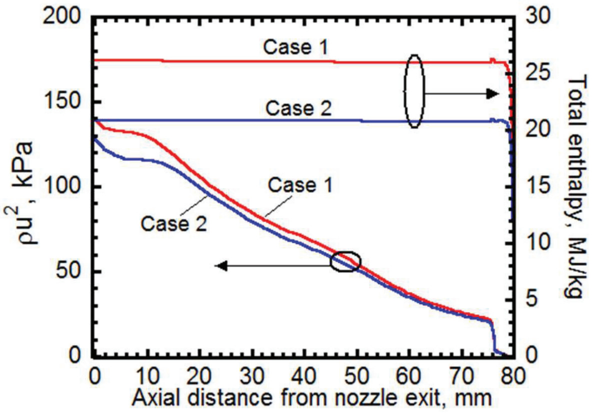

Fig. 4.1 Comparison of axial centerline momentum flux and total enthalpy

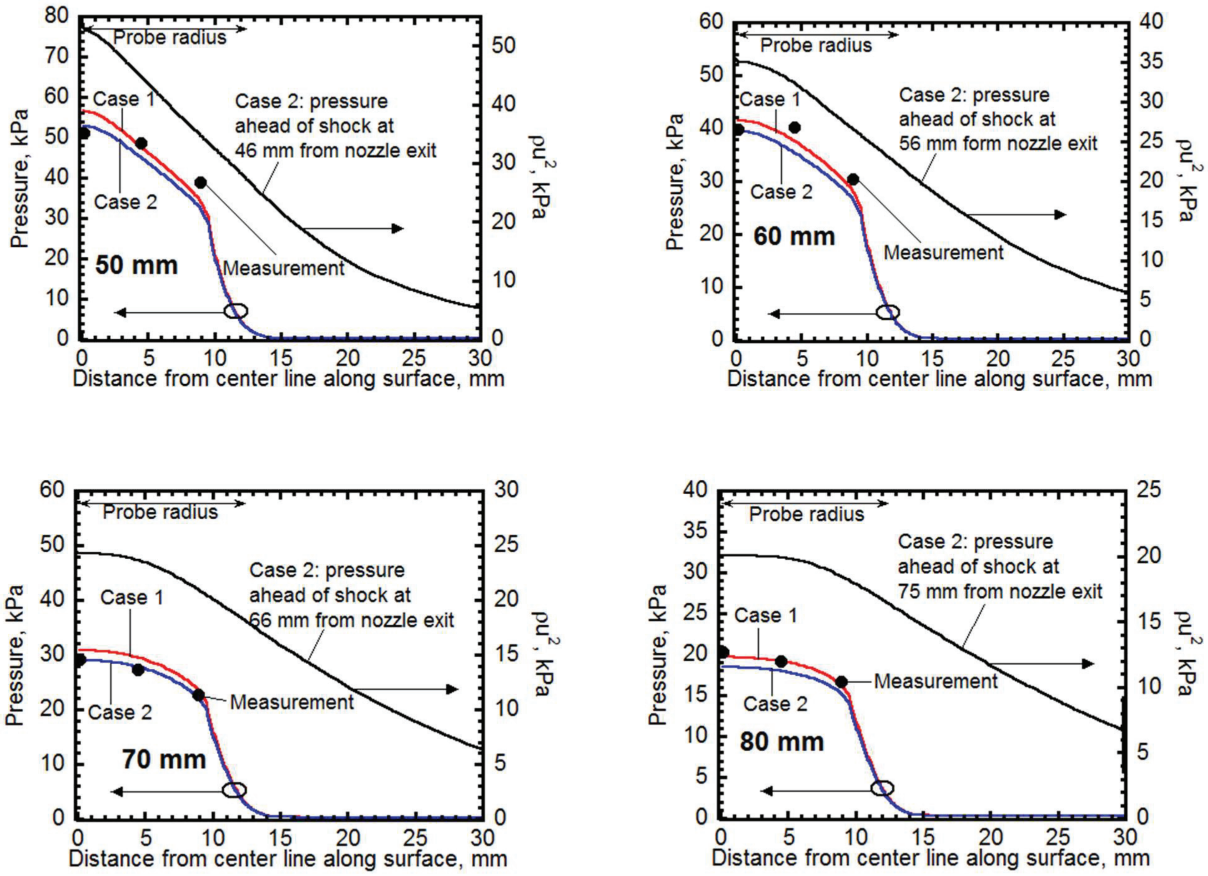

Fig. 4.2 Comparison of pressure at various axial positions from nozzle exit

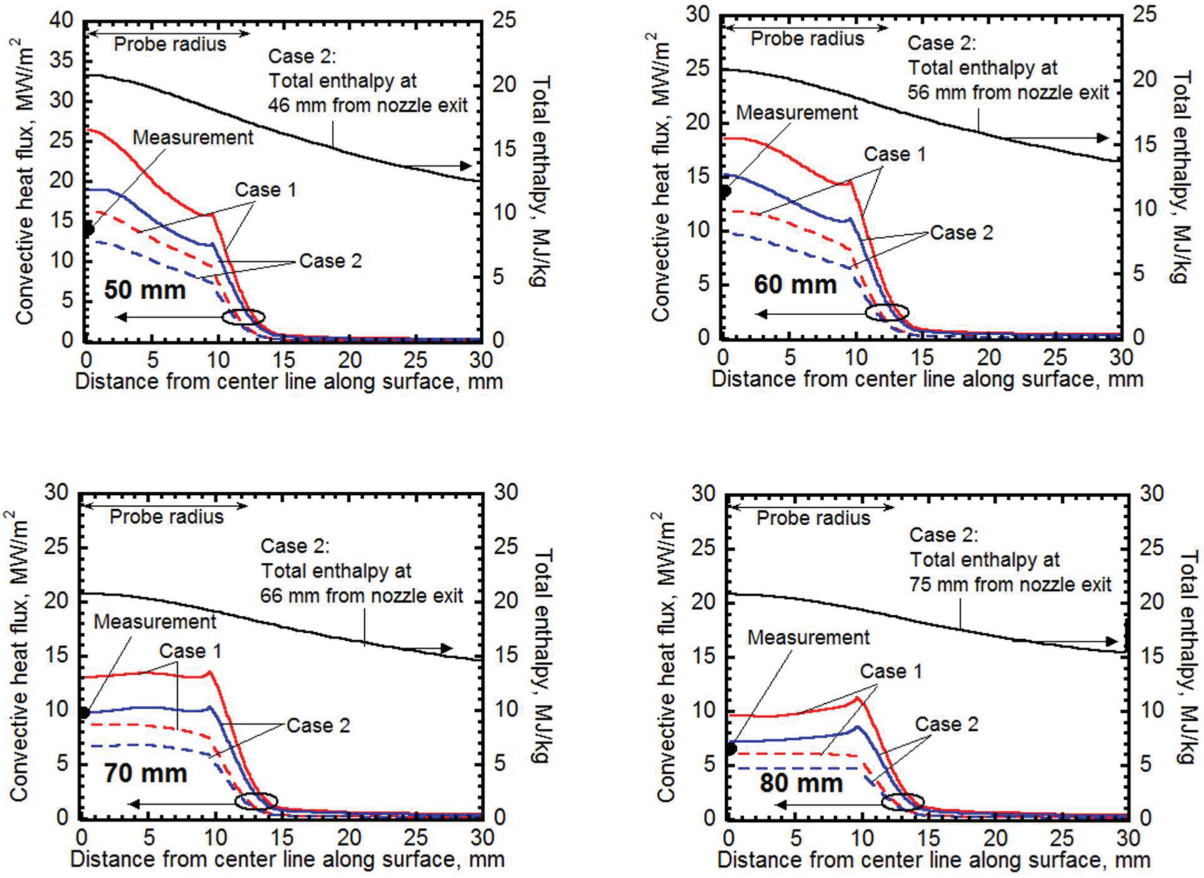

Fig. 4.3 Comparison of heat flux values at various axial positions from nozzle exit

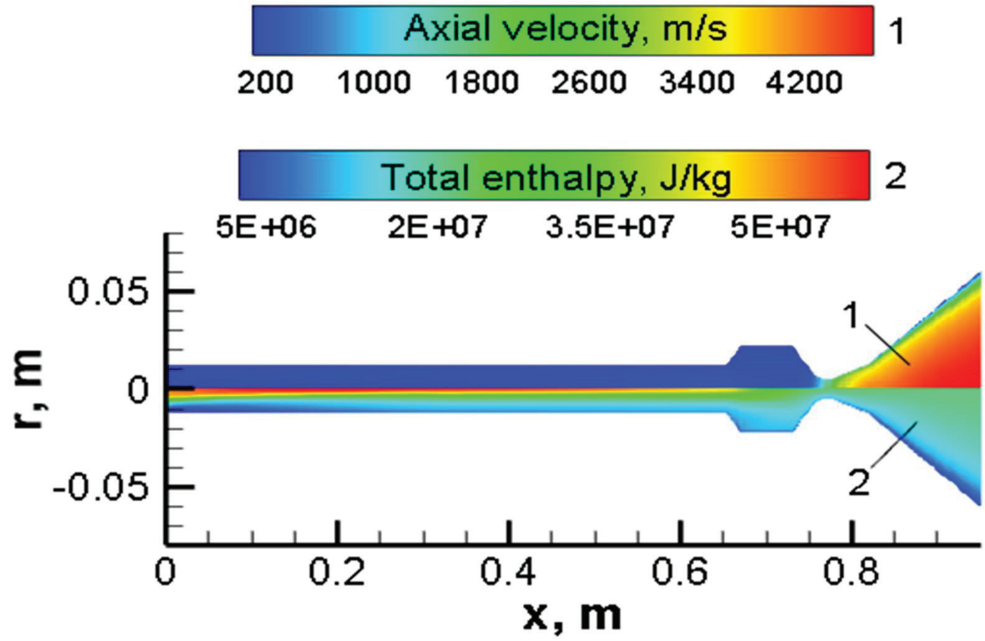

Fig. 4.4 Axial velocity and total enthalpy distributions over the entire flow field

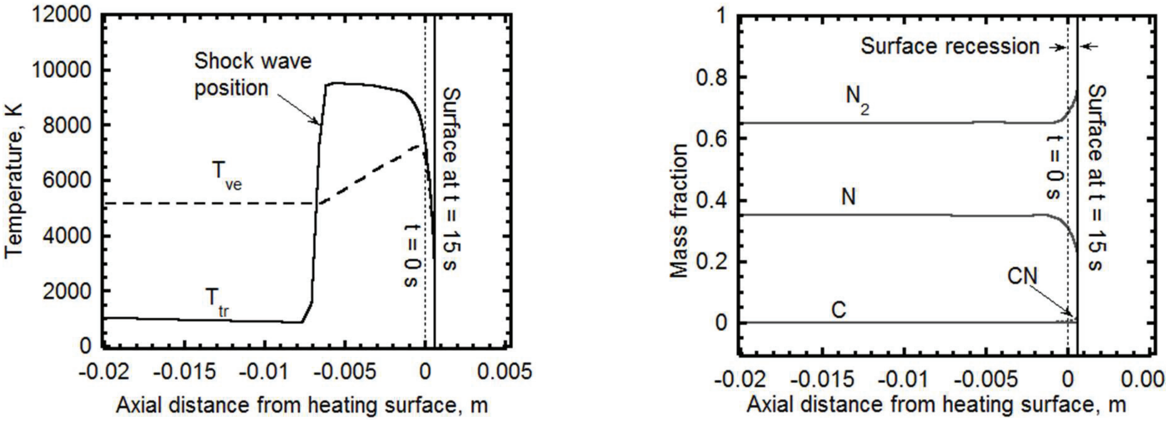

(a) Flow temperatures

(b) Species mole fractions

Fig. 4.5 Centerline flow temperature distribution and species mole fractions after 15s

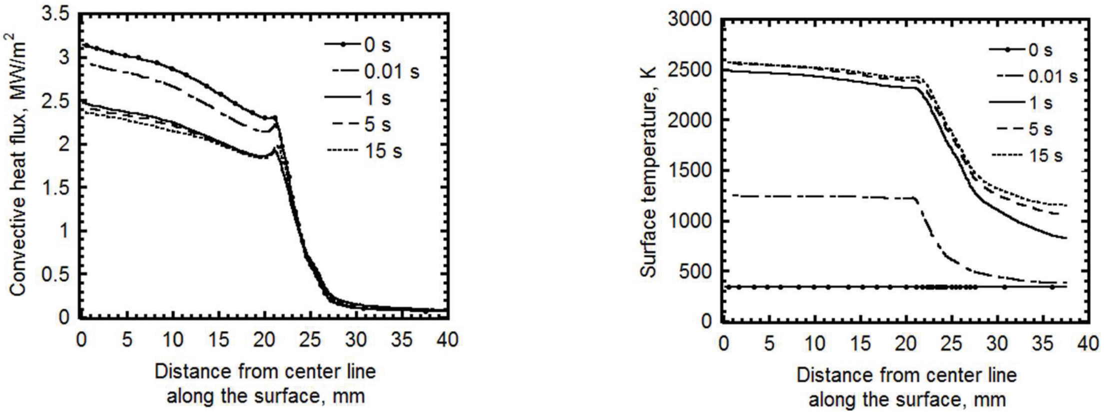

(a) Convective heat flux (b) Surface temperature

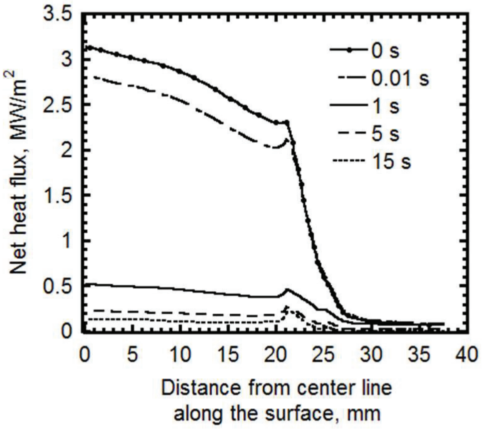

(c) Net heat flux

Fig. 4.6 Heat flux and temperature distributions along the heating surface

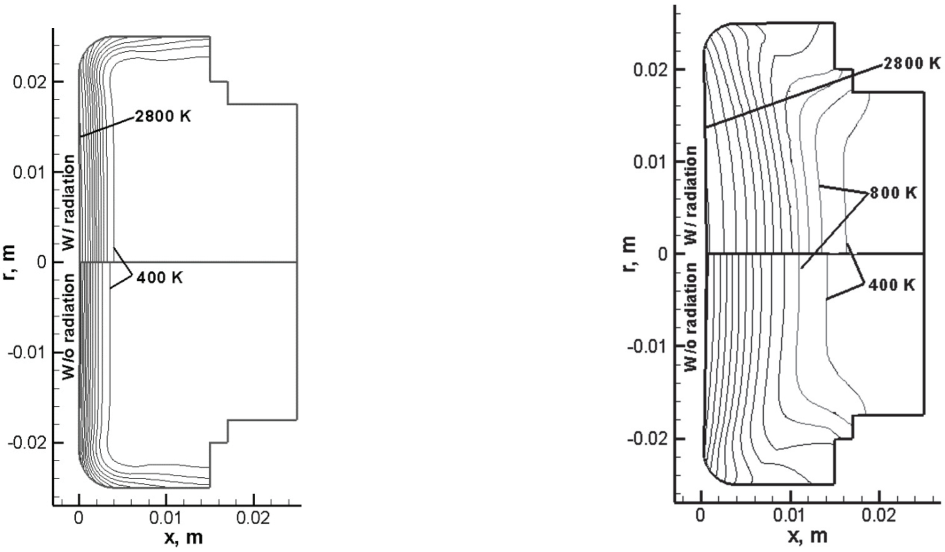

(a) 1 s

(b) 15 s

Fig. 4.7 Unsteady thermal diffusion through 0.15 g/cm^3 material

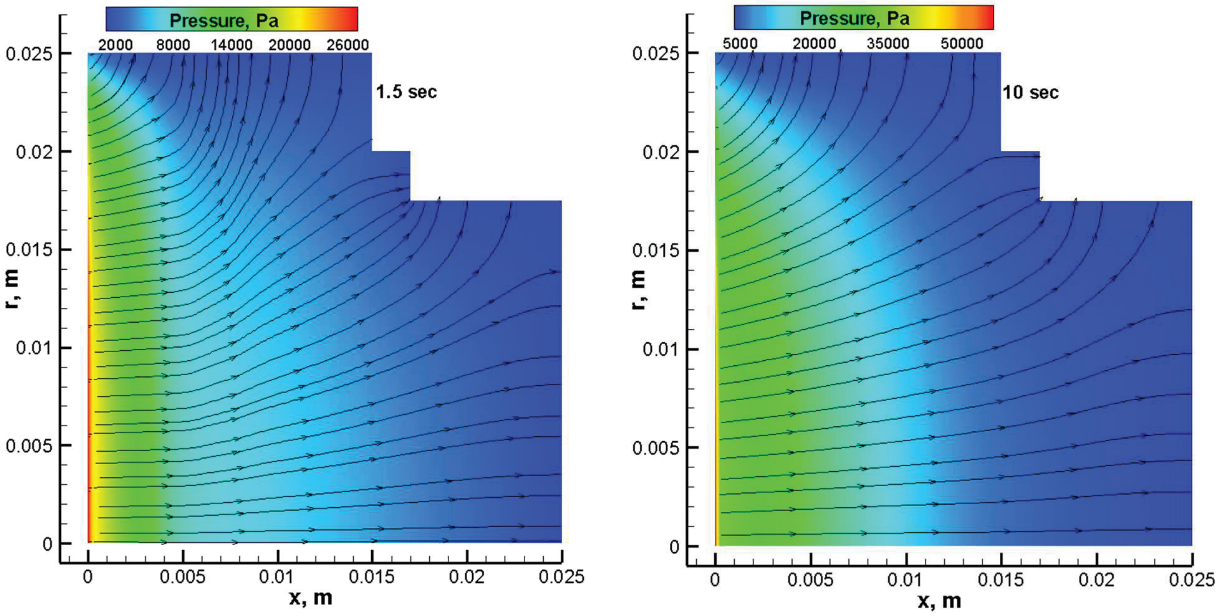

Fig. 4.8 Spatial pressure and flow distribution through 0.12 g/cm^3 material

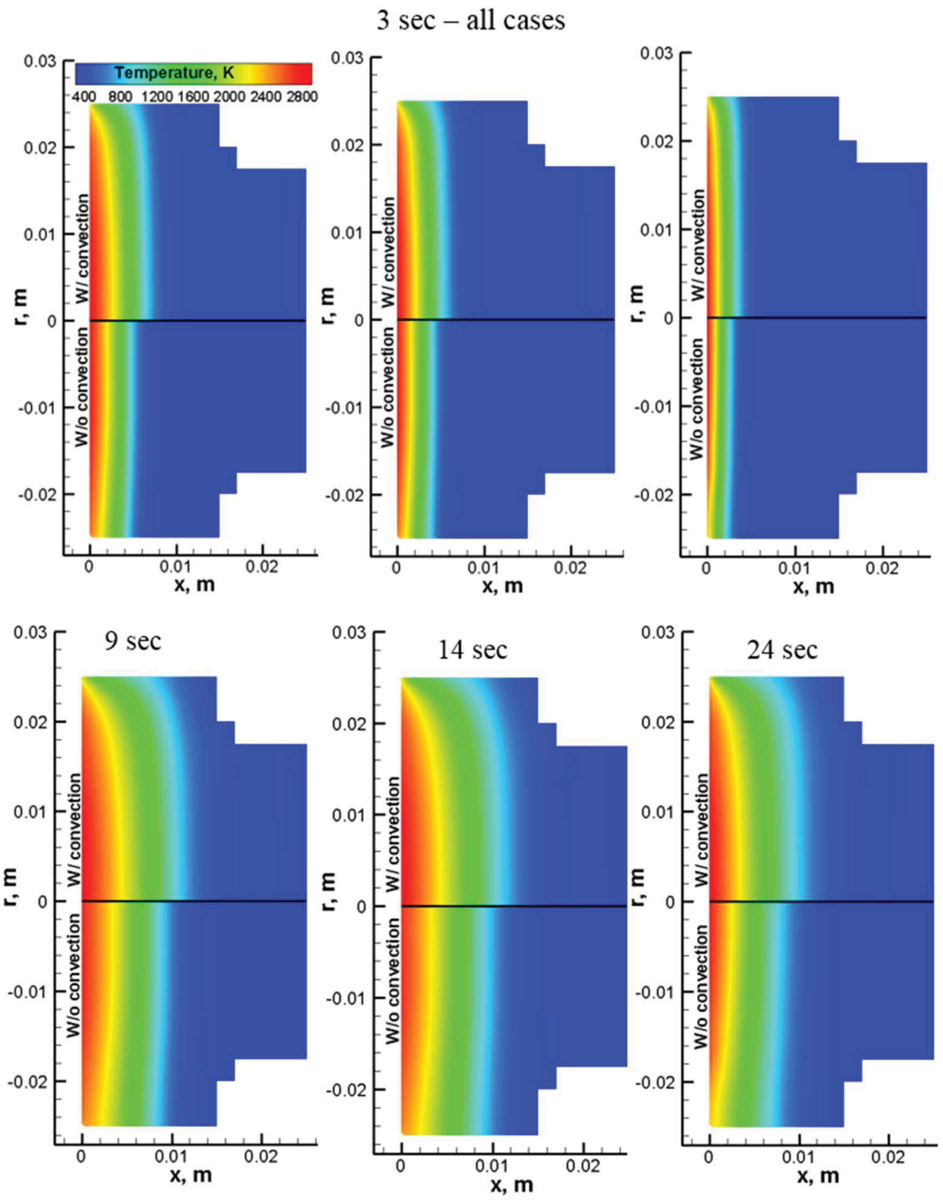

(a) 0.12 g/cm^3 (b) 0.15 g/cm^3 (c) 0.27 g/cm^3

Fig. 4.9 Temperature contour distribution within the test materials

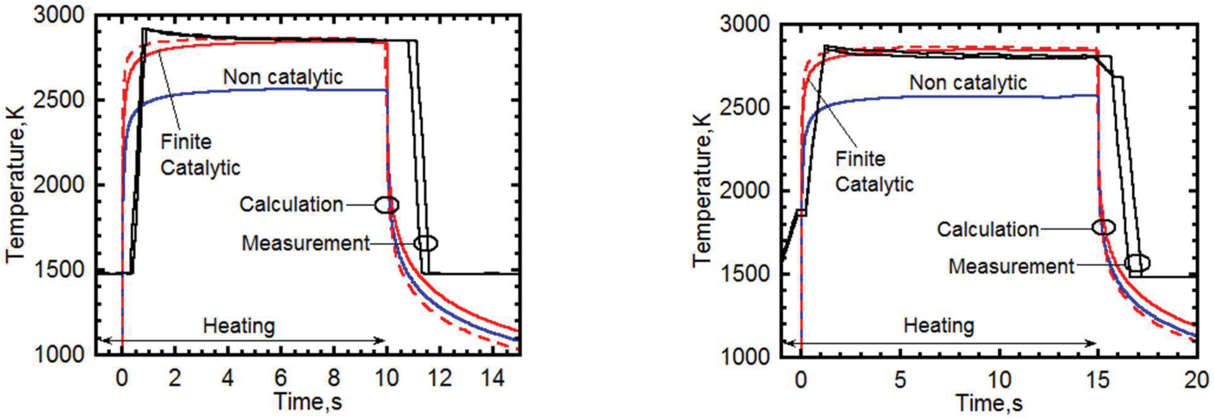

(a) 0.12 g/cm^3 (b) 0.15 g/cm^3

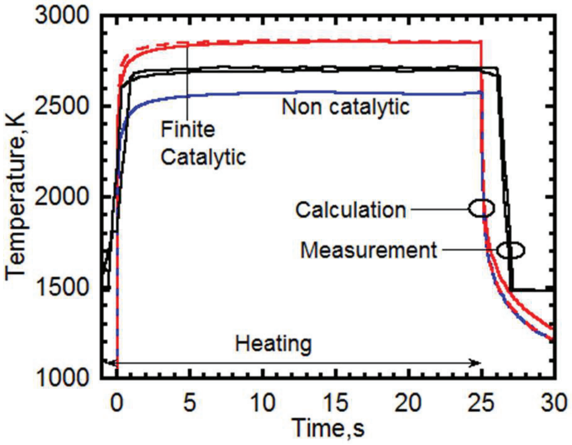

(c) 0.27 g/cm^3

Fig. 4.10 Stagnation point surface temperature time histories

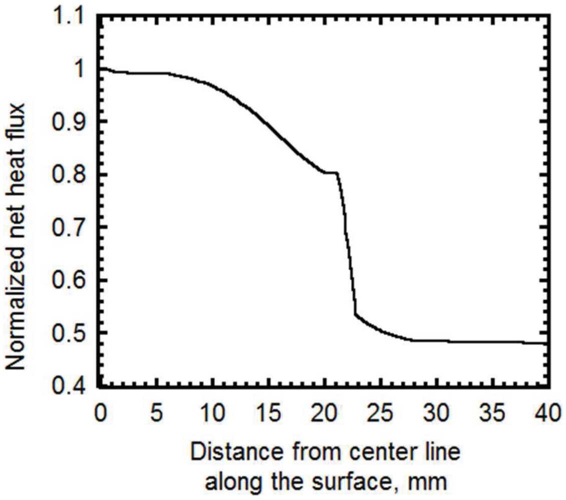

Fig. 4.11 Normalized heat flux distribution

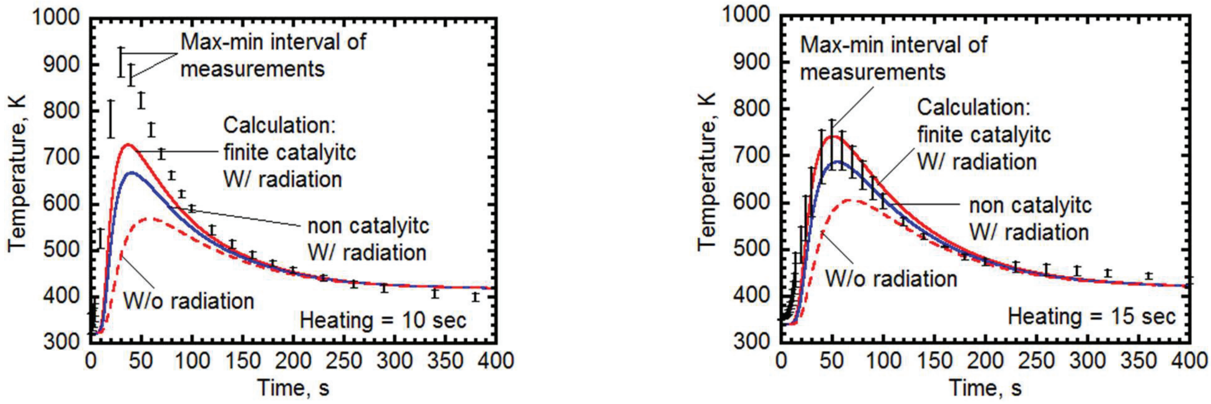

(a) 0.12 g/cm^3 (b) 0.15 g/cm^3

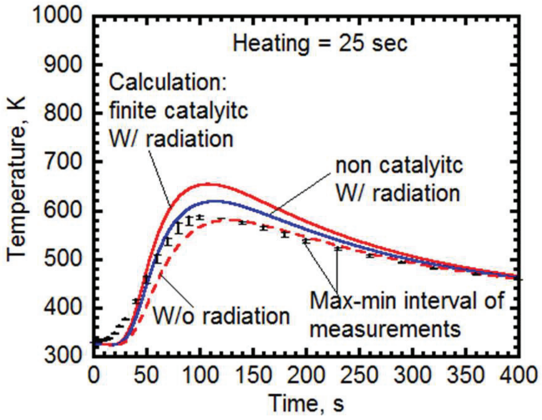

(c) 0.27 g/cm^3

Fig. 4.12 Temperature distribution at 18 mm depth position for coupled calculation

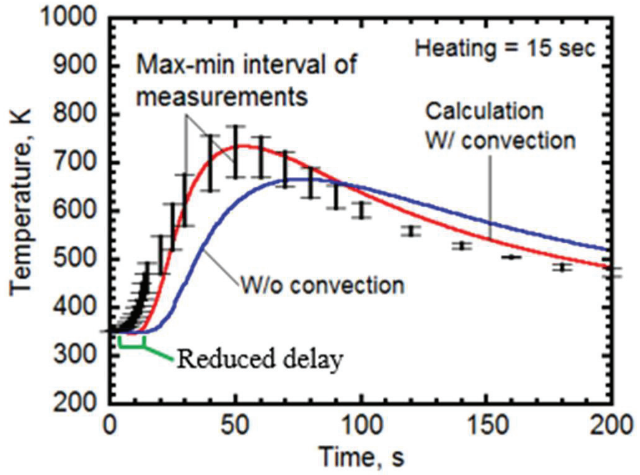

Fig. 4.13 Effect of the convective transfer in 0.15 g/cm^3 material at 18 mm depth

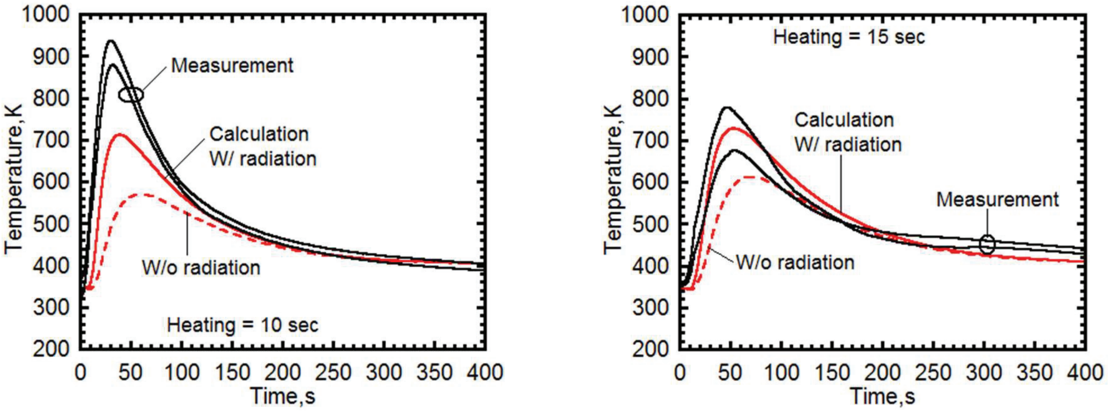

(a) 0.12 g/cm^3 (b) 0.15 g/cm^3

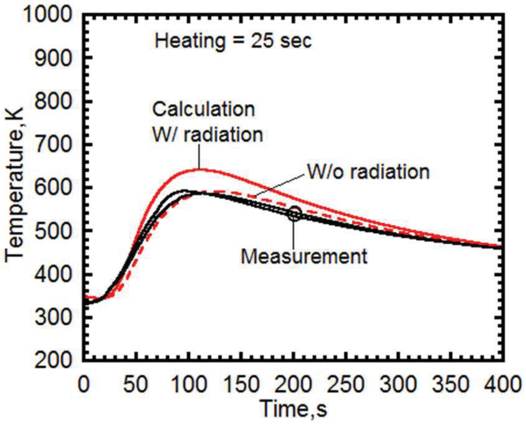

(c) 0.27 g/cm^3

Fig. 4.14 Temperature distribution at 18 mm depth for uncoupled calculations

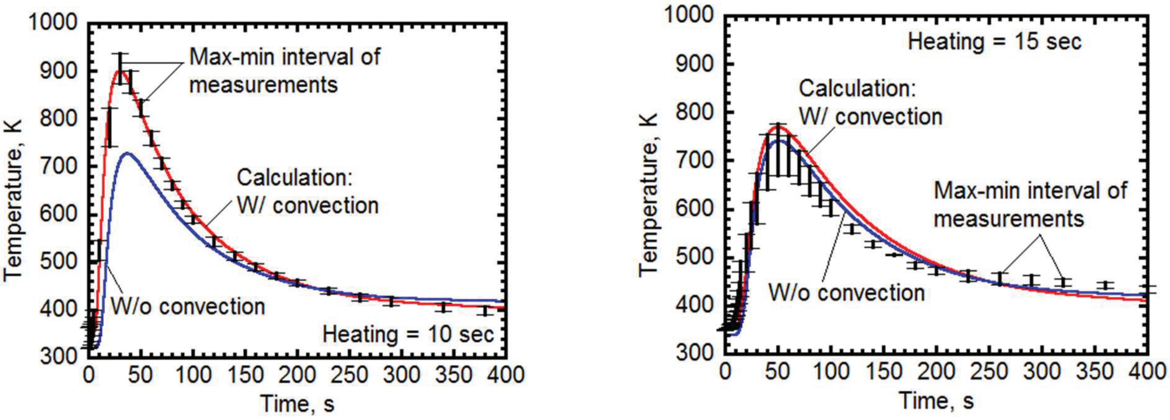

(a) 0.12 g/cm^3 (b) 0.15 g/cm^3

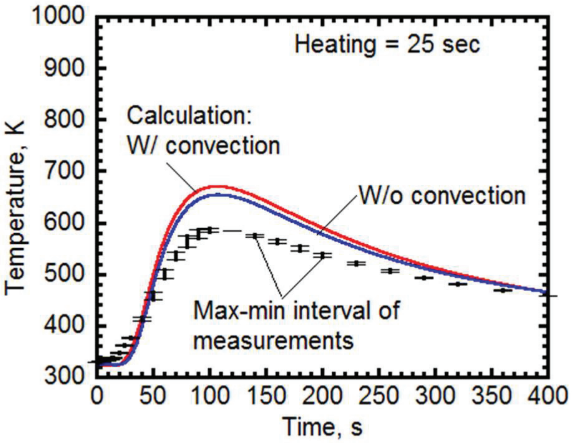

(c) 0.27 g/cm^3

Fig. 4.15 Influence of convective strength on temperature distribution at 18 mm depth

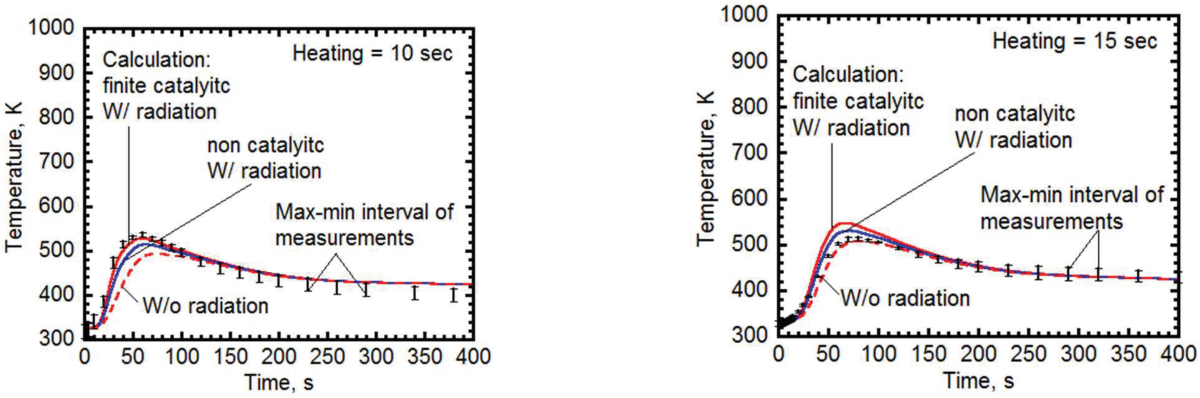

(a) 0.12 g/cm^3 (b) 0.15 g/cm^3

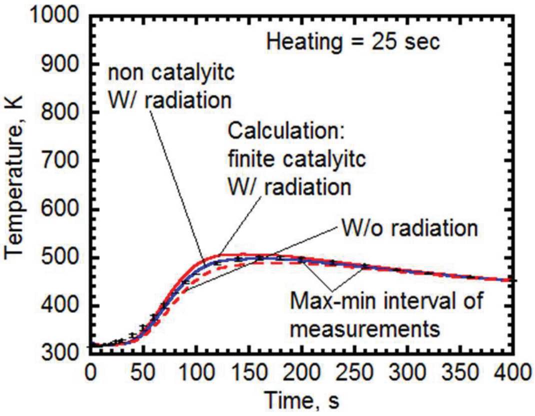

(c) 0.27 g/cm^3

Fig. 4.16 Coupled calculation in-depth temperature distribution at 23 mm position

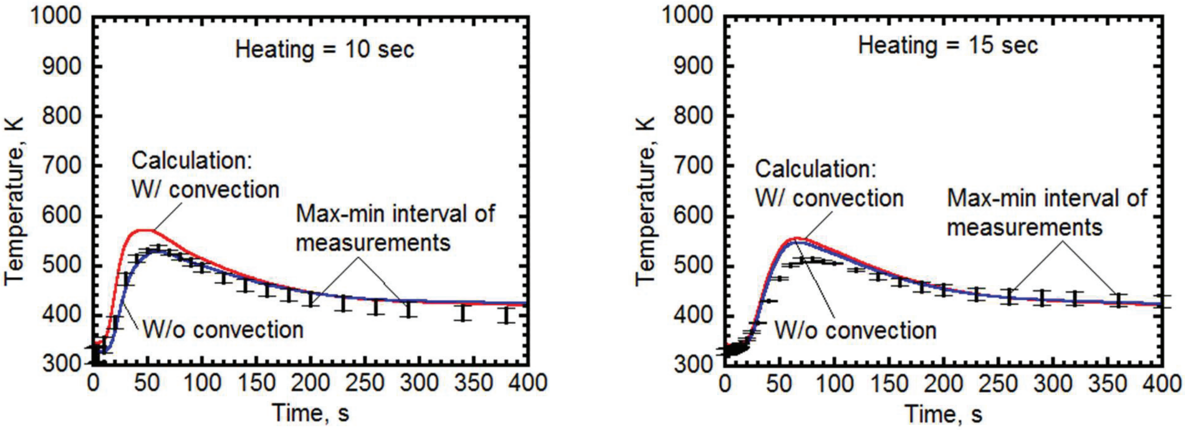

(a) 0.12 g/cm^3 (b) 0.15 g/cm^3

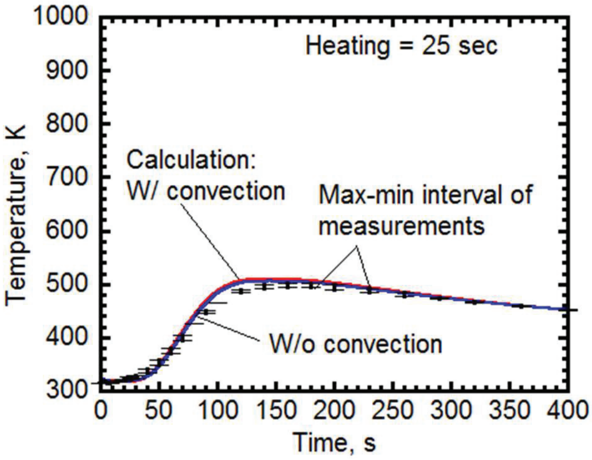

(c) 0.27 g/cm^3

Fig. 4.17 Influence of convective strength on temperature distribution at 23 mm depth

Chapter 5

Summary, Conclusions and Recommendations

5.1 Summary

An accurate and reliable analysis of the TPS performance prediction requires a rigorous study through the ground tests, and numerical modeling campaigns. Inability of the ground tests to investigate some intricate flow field details have singled out the numerical analysis approach as the first among equals in terms of preference. Numerical analysis methods have particularly gained popularity due to the development of high-performance computers which tremendously reduce both the computing and the financial resources by a great deal. However, allocating high fidelity in utilizing these methods calls for their mandatory validation using the ground tests data. The overall objective of this study was to develop a high-fidelity computer code that is capable of analyzing the thermal response of a highly porous heat shield material subjected to atmospheric re-entry heating conditions. Ground tests were also conducted to generate data for purposes of validation of the developed numerical methods in this study. The other objectives of the study included: validation of the ARCFLO3+ and the test chamber CFD flow codes, investigation of the influence of the convective transfer to the overall thermal response analysis and the preliminary study of the convective transport contribution to the overall thermal transfer within porous carbon-based materials.

In Chapter 1, an introduction to the study was laid out. Here, a brief background and history of the space exploration missions were highlighted. Previous researches on the TPS ablation, radiative transfer models, and flow analysis within the arc heated wind tunnels were also explained, carefully stating the existing challenges with the existing radiative transfer models and the wind tunnel simulation models. At the end of this chapter, the study problem was described and the objectives to be achieved stated.

In Chapter 2, operating principle of the ground test facility (the constrictor-type arc heated wind tunnel, in this case) were briefly described. Then preparation procedure for the test specimens was explained. Two different test material configurations were used: a 25 mm diameter blunt body specimen was used for the ARCFLO3+ code validation experiments and 50 mm diameter specimens were used for the thermal response analysis study. Three porous carbon-based materials of density 0.12, 0.15 and 0.27 g/cm^3 with respective porosity values of 0.93, 0.90 and 0.85 were used in the current study. The 0.27 g/cm^3 test specimen (char) was prepared through a furnace-controlled heat treatment of an ablative material developed in-house. The remaining two porous carbon-based materials were used in their original state from Osaka Gas Chemicals Co., Ltd manufacturer. Thereafter, the experimental test conditions were described. The 1 MW constrictor-type arc heated wind tunnel, managed and operated by JAXA at the ISAS, was utilized during the experiments in this study. In the arc heater section, the measured data included: freestream arcjet mass flow rate, the arc heater input power, the arc voltage, the arc electric current, the pressure at the wall of the arc heater chamber, the mass averaged enthalpy and the thermal efficiency of the arc heater. In the test chamber section, the stagnation point distribution of flow field variables, i.e. the Pitot pressure and the heat flux values, were measured at various positions of 50, 60, 70, and 80 mm from the physical nozzle exit along the axial direction. The measurements conducted for analyzing the test material's thermal response included the cold wall heat flux, the nominal Pitot pressure, and the temperature time histories for the heating surface, the 18, and 23 mm in-depth positions and the rear surface of the test material. Heating times of 10, 15, and 25s were maintained for the 0.12, 0.15 and 0.27 g/cm^3 test materials, respectively.

In Chapter 3, all the numerical methods applied in this study were described. First, the physical and numerical models for the arc heater flow field were described. Here, the governing equations for solving thermochemical equilibrium state within the arc heater were expressed and elaborated. Then the radiation model for calculating radiative heating within the arc heater using the ARCFLO3+ code was explained. Thereafter, validation of ARCFLO3+ code using the measured data was done. After this, the physical and numerical models for the nozzle and shock layer flow fields were described, explaining the following: the governing equations, transport coefficients, equation of state, chemical reaction model, energy exchange between various modes of energy, and the numerical approach. Finally, the physical and numerical models for the material thermal response analysis were described. Under this, the following were elaborated: the governing equations, physical modeling of radiative conductivity, thermophysical properties, computational meshes and boundary conditions, coupling method, and grid convergence study.

Finally, in Chapter 4, calculation and measurement results from this study were compared and discussed in order to validate the developed numerical analysis methods. The presented results were divided into two broad categories, i.e. arcjet flow results, and TPS thermal response analysis results. Under the arcjet flow modeling, results were compared for the arc heater operating conditions as well as for the distribution of the arcjet flow properties. Under the TPS thermal response analysis, results were compared for the heat flux and flow distribution, and for both the surface and in-depth temperature time histories. In the discussion, possible reasons for some of the observed behavioral patterns in the results' comparison were pointed out. It should be noted that an overall acceptable agreement between the calculated and the measured data was achieved across all the study cases.

5.2 Conclusions

The overall objective of developing a high-fidelity computer code that is capable of analyzing the thermal response of a highly porous heat shield material subjected to atmospheric re-entry heating conditions was successfully achieved. In the code, radiative conductivity was modeled using the extinction coefficient evaluated from the X-ray CT model. The radiative conductivity values obtained from the micro-scale specimen information using the X-ray CT data could be sufficient enough to predict the macroscopic energy transfer within the TPS materials. The deduced extinction coefficient values were 4692 ± 882, 6656 ± 666, and 13610 ± 1182 m^{-1} for the 0.12, 0.15, and 0.27 g/cm^3 test materials, respectively.

The coupling approach between the arcjet flow and the material response in the current study was able to sufficiently capture the radial non-uniformity in the flow field variables and therefore contributed greatly to the good results agreements that were registered. The developed coupling method was also able to effectively predict the final shape of the test specimen at the heated surface, precisely recording about 0.3 mm recession at the stagnation point against 0.3±0.16 mm value from measurements. This meant that the surface chemical reactions were properly incorporated in the calculations. Consequently, the compared surface and in-depth temperature time histories all agreed reasonably.

Validation of the ARCFLO3+ code for solving the arc heater operating conditions was successfully done. In this process, a maximum error margin between the measured and calculated arc heater operating conditions was within 2%. The CFD flow code was successfully verified against the experimental data. This was evidenced by the good agreement between the measured and calculated Pitot pressure values. Again, the heat flux calculation with both the non-catalytic and fully catalytic flows was able to achieve a range of results within which the measured value was found.

Through the uncoupled flow calculation, the contribution of the convective transport to the total heat transfer analysis was well demonstrated. Preliminary investigation of this contribution with varying mass flux values for the test specimens was also successfully achieved.

5.3 Recommendations

Although an overall success was achieved in this study, the prediction accuracy of the in-depth temperature distribution was not quite satisfactory even after the improvement of the surface temperature agreement using a finite catalytic flow at the heating surface. A peculiar phenomenon of delay in the onset of the temperature rise during heating was noted with the current material response model. Preliminary examination with the uncoupled calculations pointed out that omission of the convective transfer in the overall thermal analysis could be a potential contributor to the observed anomaly. Therefore, a further detailed analysis that is able to accurately account for the arcjet flow into the test material is recommended.

Furthermore, the current coupling model works with the material response code that solves purely the solid material energy conservation equation. It is recommended that the model be upgraded to accommodate the arcjet flow conservation equations alongside the solid material energy conservation equation. This way, it will be possible to simultaneously solve the radiative, convective, and conductive heat transfers in a coupling process between the CFD flow and material response codes with a much closer precision.

Achievements

Journal Publication:

1. Owiti, B. O., Sakai, T., and Ishida, Y., "Radiative Transfer in a Low Density Ablative Material Under Arcjet Flow Conditions," *Journal of Thermophysics and Heat Transfer*, Vol. 34, No. 1, 2020, pp. 181-192. (Published online in https://arc.aiaa.org/toc/jtht/34/1).
2. Bernard O. Owiti, Takeharu Sakai, Kazuhiko Yamada, Toshiyuki Suzuki and Kazuhisa Fujita, "Current Status of Modeling High Enthalpy Arcjet Flow," *Trans. JSASS Aerospace Tech. Japan*, (accepted for publication).

International Conferences:

1. Owiti, B. O., Sakai, T., Ishida, Y., and Tanno, H., "Thermal Response Simulation of Low Density Heat Shields Under An Arcjet Flow Condition," The 32nd International Symposium on Shock Waves (ISSW32), Singapore, 14th –19th July, 2019.
2. Owiti, B. O., Sakai, T., Kawabata, H., and Ishida, Y., "Thermal Response Analysis of Low Density Ablative Materials Subjected to High Temperature," American Institute of Aeronautics and Astronautics (AIAA) Paper 2019-1777, San Diego, California, America, 7th – 11th January 2019.
3. Owiti, B. O., Sakai, T., Kawabata, H., and Ishida, Y., "Coupled Radiation, Conduction and Convection Analysis of Low Density Heat Shield Material in High Temperature Environments," International Conference on Flow Dynamics (ICFD), Sendai, Japan, 7th –9th November, 2018.

Acknowledgments

I would like to sincerely thank, in a special way, my able supervisor, Professor Takeharu Sakai. His continued professional guidance was a major contributor to the success of my Ph.D. studies, especially having introduced me to CFD studies literally from basics. Professor Sakai's experience was quite invaluable for the improvement in my program coding, writing and even oral presentations capabilities.

I would like to thank Dr. Toshiyuki Suzuki and Dr. Yuichi Ishida of JAXA for their input throughout the study period. May I also extend my gratitude to fellow graduate students in the Thermal Energy Engineering Laboratory, Tottori University, as well as all my friends who contributed in one way or the other for the successful conclusion of this research study. Their input can never pass unappreciated.

JICA has been at the center stage throughout this time of studies, offering continuous financial and monitoring support. I am truly grateful to JICA in particular and the government of Japan in general for offering me this unique, rare and special opportunity to expand my knowledge boundaries and apply the same to improve other aspects of life especially in my developing part of the world. Special thanks to my JICA coordinator, Ms. Harumi Higashiyama, for her constant support and motivation throughout this period, not to mention her regular monitoring and discussion meetings.

I also want to convey sincere gratitude to the final defense committee members; Professor Hiromitsu Kawazoe, Professor Yutaka Hara, and Professor Tetsuya Oda for their important contributions both during the pre-defense and during the final defense presentations. I am truly grateful to the entire committee.

My children and my sister have been a constant source of inspiration throughout this research journey. Thank you very much for being there always to support my course, offer a perpetual moral comfort, and for walking the entire stretch of the journey.

I would also like to sincerely thank my Ph.D. defense committee for their positive critiques and guidance during the examination period. Their contribution went a long way to improve the quality and the final outcome of my study.

Finally, I wish to thank the Almighty God for granting me the strength, the good health and eventual success in my studies.